Earthquake and volcanic processes at mid-ocean ridges

Yen Joe Tan

Submitted in partial fulfillment of the
requirements for the degree of
Doctor of Philosophy
in the Graduate School of Arts and Sciences

COLUMBIA UNIVERSITY

2019

ABSTRACT

Earthquake and volcanic processes at mid-ocean ridges

Yen Joe Tan

In this thesis, I present results that broadly fall into two themes. The first involves understanding active tectonic and magmatic processes at mid-ocean ridges. The second involves using small stress changes due to the tides to probe earthquake processes at mid-ocean ridges. The four main results of my thesis are as follow: (1) The spatiotemporal evolution of an eruption at a fast-spreading mid-ocean ridge, the East Pacific Rise, is now characterized and understood to be mainly controlled by the buildup of tectonic stress to a critical level rather than magma overpressure. (2) Microearthquakes at the East Pacific Rise are found to be strongly modulated by tides in the years before an eruption but not immediately after the eruption, suggesting the potential utility of tidal triggering strength for eruption forecasting. (3) Earthquake size-frequency distribution, often quantified using the b value, is shown to vary systematically with tidal stresses which lends support to the use of earthquake b value as an in-situ stressmeter. (4) The 2015 Axial Seamount eruption is revealed to be preceded by variable rates of melt influx into the shallow reservoir, highlighting the short-timescale variability of magmatic systems as they are primed for an eruption.

Contents

Acknowledgements

I owe a great deal to many people for where I am today. Firstly, I have been very lucky to have had many great mentors in my career so far. I thank my thesis advisors Maya Tolstoy and Felix Waldhauser for their countless insightful advice and for being extremely supportive of my various pursuits. Jian Lin, for introducing me to the fascinating world of marine geophysics. Bill Menke, Göran Ekström, and Meredith Nettles for their willingness to teach and ability to explain concepts in the clearest manner. David Marsan for hosting my visit in France and always entertaining my random musings.

I would like to thank all the Lamont-Doherty people who enriched the past five years of my life. Bridgit Boulahanis for keeping me sane. Dan Sousa for being an amazing roommate. Joshua Russell for introducing me to birdwatching. Kira Olsen, Weston Anderson, Dan Rasmussen, Helen Janiszewski, Hannah Rabinowitz, Natalie Accardo, Celia Eddy, Rachel Marzen, Genevieve Coffey, Kelvin Tian, Spahr Webb, Roger Buck, Jim Gaherty, Donna Shillington, Chris Scholz, Terry Plank, Ben Holtzman, and Timothy Crone for the numerous interesting conversations and discussions.

Finally, I would like to thank my parents, brother, and wife for their unwavering

support throughout my life. And Rijan Maharjan, who always makes sure I do the right thing.

Dedicated to everyone who has helped me become a better person.

Introduction

Light does not penetrate beyond the first few hundred meters of the ocean and so most of the seafloor is shrouded in complete darkness. Yet, this is where over two-thirds of the Earth's volcanic activity occur, mostly along the ∼70,000 km of mid-ocean ridges. The difficulty in sustaining long-term continous monitoring in the marine environment means that these volcanic systems have remained relatively underexplored compared to their subaerial counterparts. It is this sense of exploration that is the primary driver behind the work in this thesis, as I was blessed with the opportunity to work with two unique datasets that represent two of only a few *in-situ* geophysical observations of mid-ocean ridge eruptions. Working on understanding these volcanic systems subsequently led to the realization that the sensitivity of mid-ocean ridge microearthquakes to tidal stress perturbation also provides a unique natural laboratory for us to further understand fundamental earthquake processes. Hence a thesis on both earthquake and volcanic processes at mid-ocean ridges. The two study areas of this thesis are the East Pacific Rise near 9°50'N and the Axial Seamount on the Juan de Fuca ridge (Fig. 1).

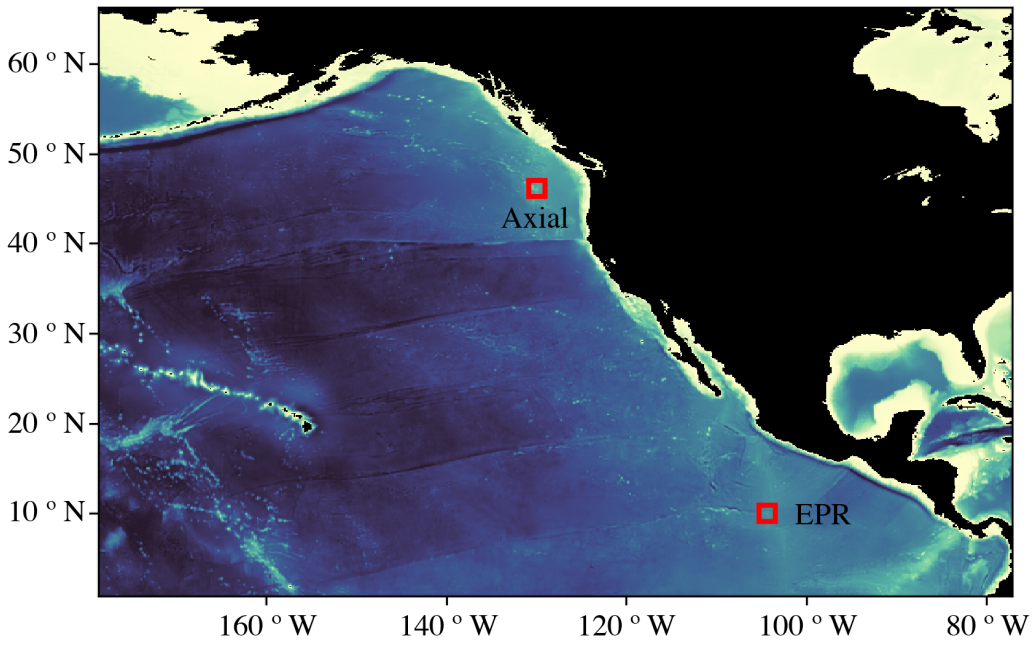

Figure 1: Regional map showing locations of Axial Seamount and 9°50'N East Pacific Rise.

Axial Seamount

In early 2015, a real-time cabled seafloor observatory was completed on the summit of Axial Seamount, a volcano formed at the intersection of the Juan de Fuca ridge and the Cobb hotspot off the coast of Oregon. This represents a state-of-the-art monitoring network on a submarine volcano. Coupled with prior high-resolution active-source imaging of the shallow magma reservoir [1, 2], the observatory provides a unique dataset to understand the structures and processes that control this magmatic system. As luck would have it, the volcano erupted in April 2015. This immediately became the best-characterized submarine eruption to-date. The diking-eruptive sequence involved both northward and southward dike propagation [3–5],

with lava being erupted only in the northern caldera floor and the north rift zone [6, 7] and being sourced from a steeply-dipping prolate-spheroid pressure source beneath the southeastern part of the caldera that extends from 1.75 km to 6 km depth [4]. Earthquakes located were found to delineate outward-dipping faults that were reactivated as the volcano inflates and deflates [3, 5, 8]. However, there had not been much focus on the buildup to this eruption. We thus decided to analyze the data during this time period in the hope of better understanding how the magmatic system built up to an eruption. Through the integration of measurements of seismic velocity variations and the spatiotemporal evolution of earthquakes as well as deformation rate, we show that a few weeks before the eruption, there was increased rate of melt influx into a region of the shallow reservoir from which the erupted lavas were subsequently sourced. The integration of multiple datasets is necessary to fully characterize the shallow magma reservoir where melt influx can vary over short time and small spatial scales, and is a step forward towards better eruption forecasting.

Earthquakes follow a power-law size–frequency distribution with the b value often used to quantify the relative frequency of small and large magnitude earthquakes. In rock fracture experiments, the b value of small fracture events was found to correlate with stress [9]. This prompted the idea that earthquake b values can be used as stressmeters to estimate spatiotemporal variations of the solid earth's stress state. However, the underlying assumption that earthquake b value is stress-dependent still has to be verified. Several attempts have been made looking at the correlation of earthquake b value with faulting style [10], depth [11], and subducting plate age [12]. However, these studies were restricted by small sample sizes and the need to combine

earthquakes over large spatial regions, as well as the inability to control for other variables that might also affect earthquake b values such as rock heterogeneity [13] and fault roughness [14]. In the three months before the April 2015 Axial Seamount eruption, ∼60,000 earthquakes which delineate a ring-fault system [3] were located in a 25 km^3 block of crust that experiences periodic tidal loading. The microearthquakes at Axial Seamount had been previously shown to be strongly modulated by tidal stress [3, 15]. The large number of earthquakes within a small region, combined with the earthquakes' sensitivity to tidal stress perturbations [3, 15] on the order of ±20 kPa in this region, gives us a unique natural laboratory to study the stress dependence of the earthquake b value. We find that above a threshold stress amplitude, b value is inversely correlated with tidal stress. This supports the potential use of b values to estimate small stress variations in the Earth's crust. It also supports the representation of the Earth's crust as an inhomogeneous elastic medium where fracture will occur if the local stress exceeds a critical value and that fractures stop growing when they propagate into a region of lower stress [9].

9°50'N East Pacific Rise

The 2006 9°50'N East Pacific Rise eruption is one of the best studied mid-ocean ridge eruptions to-date. The earthquake rate was shown to build up steadily in the two years leading up to the eruption before decreasing sharply post-eruption [16]. Lava was found to have been erupted along 18 km of the ridge [17], mostly sourced from a 5-km-long melt lens [18] and the sub-axial melt lens underneath it [19] but

also from multiple other isolated melt lenses [20]. However, the exact timing of the eruption remained unresolved due to disagreements between geochemical dating [21] and earthquake timings [16, 22].

During the 2015 Axial eruption, William Wilcock at the University of Washington identified thousands of impulsive seismic arrivals that do not look like earthquakes or whale calls from the real-time seismic data and postulated that they might be generated by fresh lava being erupted on the seafloor. This prompted us to reexamine the seismic records from EPR and sure enough, we identified similar seismic signals. Upon locating them, we find that their locations correlate very well with the lava flow boundary that was previously mapped [17], giving us confidence that these signals were generated by freshly erupted lavas. This also gave us the confidence to use the locations of these impulsive seismic sources to guide the expedition three months after the 2015 Axial eruption on where to look for freshly erupted lava. Freshly erupted lavas were found throughout the north rift zone [6], even though the two previous eruptions in 1998 and 2011 propagated down the south rift zone [7].

The impulsive seismic events at EPR allowed us to fully characterize the spatiotemporal evolution of the erupted lava and show that the eruption occurred as a single event over a two-week period instead of the previously-proposed multiple pulses over 7-10 months [21]. Combined with the characterization of earthquakes and long-period events over the eruption period, we further inferred that the eruption was primarily controlled by the buildup of tectonic stress to a critical level instead of magma overpressure. This suggests that mid-ocean ridges might fundamentally behave differently from typical volcanic systems.

The majority of the microearthquakes at 9°50'N East Pacific Rise was inferred to be a result of hydrothermal cracking [23] and are very sensitive to tidal stress perturbations [24, 25]. The tidal stress sensitivity had even been utilized to infer the permeability structure of the system [26, 27]. The sensitivity of subduction-zone earthquakes to small tidal stress perturbation has been suggested to increase leading up to megathrust earthquakes [28–30]. However, these studies were limited by the small sample size. We proceeded to test the idea that tidal triggering strength can be a good proxy for the stress state of the mid-ocean ridge system. We used the ∼100,000 earthquakes located over a 4-year period to show that the tidal triggering signal was strong but relatively constant in the years before the eruption, but disappeared/weakened after the eruption. Our findings suggest that tidal triggering variation may not be useful for forecasting mid-ocean ridge eruptions over a 2+ year timescale but might be useful over a longer timescale.

Chapter 1

Dynamics of a seafloor-spreading episode at the East Pacific Rise

This chapter has been published in the following paper:

Tan, Y. J., Tolstoy, M., Waldhauser, F. & Wilcock, W. S. D. Dynamics of a seafloor spreading episode at the East Pacific Rise. *Nature* **540**, 261-265 (2016).

1.1 Abstract

Seafloor spreading is largely unobserved because 98 per cent of the global mid-ocean-ridge system is below the ocean surface. Our understanding of the dynamic processes that control seafloor spreading is thus inferred largely from geophysical observations of spreading events on land at Afar in East Africa and Iceland [31]. However, these are slow-spreading centres [31] influenced by mantle plumes [32, 33]. The roles of magma pressure and tectonic stress in the development of seafloor spreading are still unclear. Here we use seismic observations to show that the most recent eruption at the fast-spreading East Pacific Rise just North of the Equator initiated at a 5-kilometres-long melt-rich segment [18]. The change in static stress then promoted almost-concurrent rupturing along at least 35 kilometres of the ridge axis, where

tectonic stress had built up to a critical level, triggering magma movement. The location of impulsive seismic events indicative of lava reaching the seafloor [3] suggests that lava subsequently erupted from multiple isolated [20, 34] magma lenses (reservoir chambers) with variable magma ascent rates, mostly within 48 hours. Therefore, even at magmatically-robust fast-spreading ridges, a substantial portion of the spreading may be due to tectonic stress building up to a critical level rather than magma overpressure in the underlying magma lenses.

1.2 Introduction

The global mid-ocean ridge (MOR) system is located mostly in the deep ocean. Therefore, remote detections of seismic signals at submarine ridges are interpreted by analogy to observations at subaerial ridges to infer dynamic spreading processes. Only ten seafloor spreading events have been seismically characterized to date [3, 36], with hydroacoustic detections of migrating earthquake swarms at intermediate-spreading ridges (about 4–9 cm yr^{-1} at the full spreading rate) interpreted as lateral dike propagations [37], similar to observations at slow-spreading centres ($<$ 4 cm yr^{-1}) in Afar and Iceland [38–41]. However, less is known about fast-spreading ridges ($>$ 9 cm yr^{-1}), where the relatively thin lithosphere produces earthquakes that are extremely difficult to locate with existing hydroacoustic monitoring networks [22].

The most recent eruption occurring near 9°50'N at the fast-spreading East Pacific Rise is the first observed repeat eruption at a mid-ocean ridge [16, 42]. The event was recorded by ocean-bottom seismometers (OBSs) deployed between 9°49'N and 9°51'N

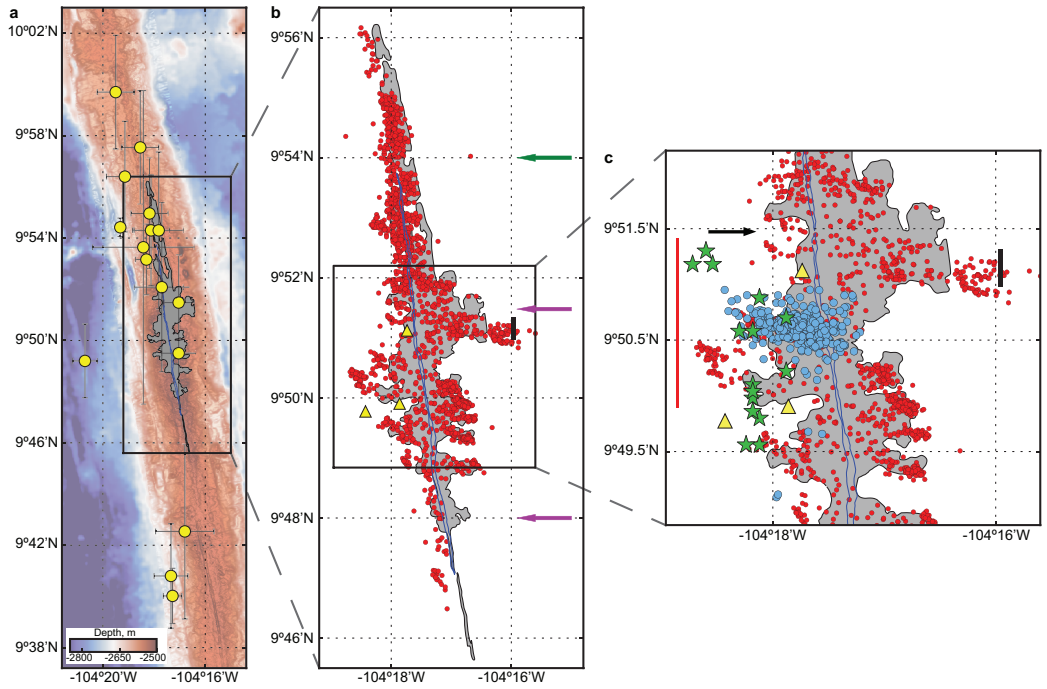

Figure 1: Location of various seismic events. a, Location of T-wave earthquakes [22] (yellow dots) and lava flow map [17] (shaded region). Error bars represent 68% confidence interval [22]. b, Location of seismometers (yellow triangles) and impulsive lava events (red dots), showing close spatial correlation with the lava flow map [17]. The AST [17] is shown as a thin blue line with green arrow marking its end. The bold black line marks the revised extent of the 2006 lava flow farther off-axis than originally identified [35]. AML disruptions (purple arrows) were inferred from seismic reflection studies post-eruption [20]. c, Location of impulsive lava events (red dots), local earthquakes (blue dots), and long-period events (green stars). The black arrow marks the break in AST and the northern extent of melt-depleted sub-AML [19] (red line) associated with the end of the northward migration of long-period events. The bold black line marks the revised extent of the 2006 lava flow farther off-axis than originally identified [35].

from May 2005 to April 2006, although only three seismometers survived the lava flow and unrelated instrument failure (Fig. 1c). A diking event on 22 January 2006 was inferred from an hour-long peak in seismic amplitude [16] and hydroacoustically detected (T-wave) earthquakes [22]. However, the eruption is widely referred to as the 2005–2006 eruption and cited as having happened in multiple pulses over a period of 7–10 months [17, 20, 34, 35] on the basis of radiometric dating results [21], similar to

the previous eruption at 9°50'N in 1991–1992 [21, 43]. This implies that the eruptions were modulated by pulses of magma injection into the underlying axial magma lenses (AMLs).

We analysed the OBS data collected from May 2005 to April 2006 and detected three types of seismic events—impulsive lava events, local earthquakes, and long-period events (Figs 1 and 2).

1.3 Methods

Impulsive lava event detection and location

We used a standard detection algorithm based on short-term average to long-term average of the seismic energy recorded by the seismometer, covering May 2005 to April 2006. We then manually went through the entire period to identify missed events and to pick the arrivals. No events were identified before 22 January 2006. During the first hour of the eruption, we could not locate all the events because many of them were occurring simultaneously at short distances from the stations, thus observed phases could not be uniquely assigned to individual events.

Events were located by assuming the signals were generated on the seafloor and had bounced off the sea surface once before reaching the seismometers (Fig. S2b inset). We used an iterative least-squares method assuming a constant sound velocity of 1.5 km s^{-1} with water depth from a high-resolution bathymetry map acquired in November 2005 [44]. The sound velocity profile with depth in this region varies from

1.48 km s^{-1} to 1.52 km s^{-1} [45]. We quantify our location uncertainties due to a simplified sound velocity model by locating the events with a sound velocity of 1.48 km s^{-1} and 1.52 km s^{-1}. This shifts our original catalogue locations by an average of 107 m. We quantify our location uncertainties due to pick error by adding normally distributed noise of standard deviation 0.1 s to the arrival times before locating the events. This is performed on the whole catalogue 100 times. On average, the event locations are shifted by < 1 m. This small uncertainty may be explained by the slow sound velocity, as the locations are well constrained by the station relative arrival times (on the order of seconds, which is much larger than the estimated pick error of 0.1 s). Event magnitudes were calculated as the logarithm of the displacement (in micrometres) multiplied by the signal travel distance (in kilometres). This assumes no attenuation other than from geometric spreading.

Earthquake detection and location

We manually went through a 6.5-h period starting from approximately 3 h before the first impulsive lava event was identified and handpicked the P- and S-wave arrivals. This was the period of highest seismic root-mean-square amplitude during the deployment [16]. These events were then used as templates for an array-based waveform correlation detection algorithm [46]. We then manually reviewed the detected events. Events with both P- and S-wave arrivals at all three stations were located using the NonLinLoc grid-search program [47]. A window of 0.5 s around each arrival was extracted for cross-correlation to get differential arrival times. Only differential

arrival times with cross-correlation coefficient above 0.7 were used in the relocation using the hypoDD program [48]. Depth-dependent P- and S-wave one-dimensional velocity models were used [49]. Local magnitudes (ML) were derived using the formulation described in [50]. Synthetic test suggests that the eastward dipping structure we observed is resolvable (Fig. S6). Least-squares errors for the relative locations were computed [48] using a subset of better-constrained events (template events and events located within the OBS array). The mean relative location errors are 120 m for longitude, 40 m for latitude, and 220 m for depth (Fig. S7).

Long-period event detection and location

We manually picked the first arrivals and located the events using a grid search method that minimizes the standard deviation of predicted source origin times based on arrival times at each station [51], assuming a fixed source depth and constant velocity of 2.5 km s^{-1}. A 100-m grid spacing was used. The epicentres of the events do not change very much between the assumed depths of 0 km to 1.5 km (Fig. S8a), which is the approximate depth of the AML [20]. Velocities between 0.5 km s^{-1} and 6.5 km s^{-1} were tested, with the velocity of 2.5 km s^{-1} giving the overall minimum standard deviation (Fig. S9). This velocity is consistent with a mean crustal S-wave velocity above 1.5 km depth [49]. However, the epicentres of the events do not change very much with change in velocity assumption (Fig. S8b), because the northward migration of the event locations is constrained by the station relative arrival time (Fig. S10).

Magma ascent rates calculation

For the northernmost segment, the AML depth varies from 1.5 km to 1.65 km [20]. The time gap between the first T-wave earthquake and the first lava event in this region is about 181 min. Therefore, the calculated magma ascent rate is between 0.14 m s^{-1} and 0.15 m s^{-1}. For the central segment, the AML depth varies from 1.45 km to 1.6 km [20]. The time gap between the first T-wave earthquake and the first cluster of lava events in this region is about 117 min (Fig. 2). Therefore, the calculated magma ascent rate is between 0.21 m s^{-1} and 0.23 m s^{-1}. However, there is a single lava event that happened about 97 min after the first T-wave earthquake in this region (Fig. 2). If this event time is used instead, the calculated magma ascent rate for the central segment is between 0.25 m s^{-1} and 0.28 m s^{-1}. This event time represents a conservative estimate for the earliest lava event in the central segment because, at the start of the eruption, many events were occurring simultaneously at short distances from the stations, so that observed phases could not be uniquely assigned to individual events. The time gap between the last long-period event and the first lava event is around 36 min. If this aseismic period is the time of magma ascent instead, it would give the fastest rate of between 0.67 m s^{-1} and 0.74 m s^{-1}.

1.4 Results

The lava events have impulsive waveforms with a dominant frequency around 22 Hz (Fig. S1), similar to those previously suggested [52] and recently confirmed to be associated with fresh lava reaching the seafloor [3]. This association is further

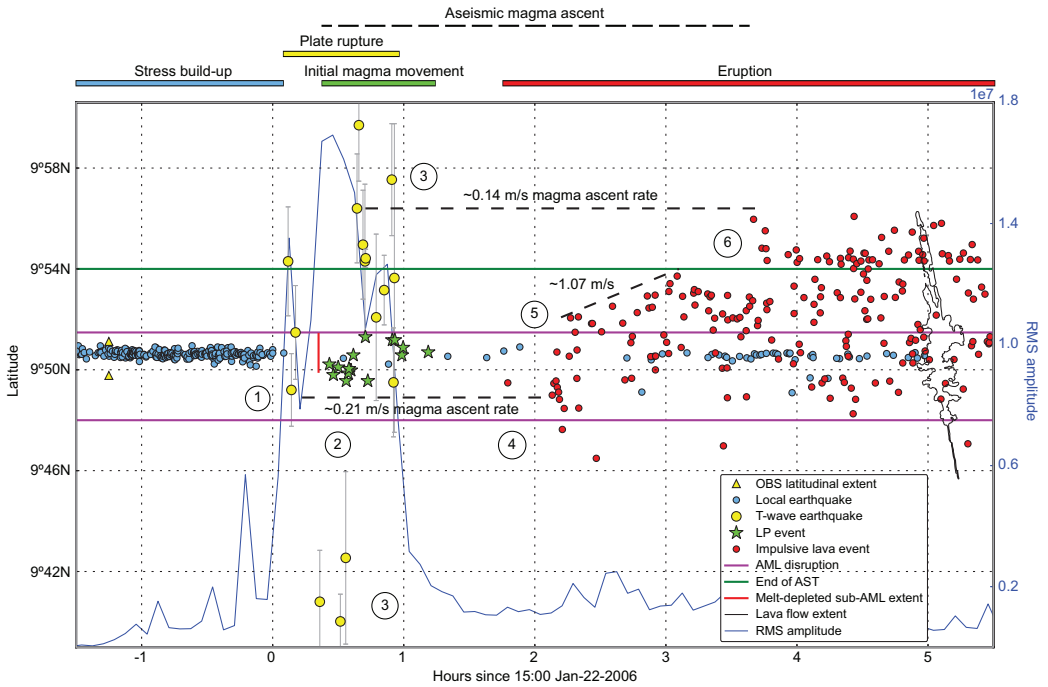

Figure 2: Temporal and along-axis progression of various seismic events. (1) Build-up of stress culminating in plate rupture. (2) This triggered magma movement from the underlying melt-rich AML. (3) The static stress change then promoted rupturing beyond the initiation region. (4) Lava first erupted in the central segment. (5) Lava then erupted from a different AML [20] at the adjacent segment. (6) Finally, the rupturing triggered magma from another isolated [34] AML to rise vertically at a slower speed and erupt with a smaller volume. T-wave earthquake error bars represent the 68% confidence interval [22]. Magma ascent rates were calculated assuming an AML depth of 1.5 km (see Methods). AML disruptions (purple horizontal lines) and extent of melt-depleted sub-AML (red vertical line) were inferred from seismic reflection studies post-eruption [19, 20]. New lava flow extent (solid black line), shown in map view for reference, was mapped post-eruption [17]. The root-mean-square amplitude of the seismic vertical channel was calculated in the 3–45 Hz band in 5-min windows (blue line). Note that flows from 9°48'N to 9°46'N did not overflow the AST and are associated with very few impulsive lava events. The southernmost T-wave earthquakes are consistent with the possible disruption of vent fluid temperatures at 9°42'N [17]. This suggests that spreading occurred along about 35 km of the ridge axis. However, spreading could have extended beyond the distal ends of the observed T-wave earthquakes.

supported by their locations (see Methods) which coincide extremely well with the fresh lava flow boundaries (Fig. 1b) mapped using digital seafloor imagery collected in 2006–2007 [17]. Their spatiotemporal evolution, where events at individual flow

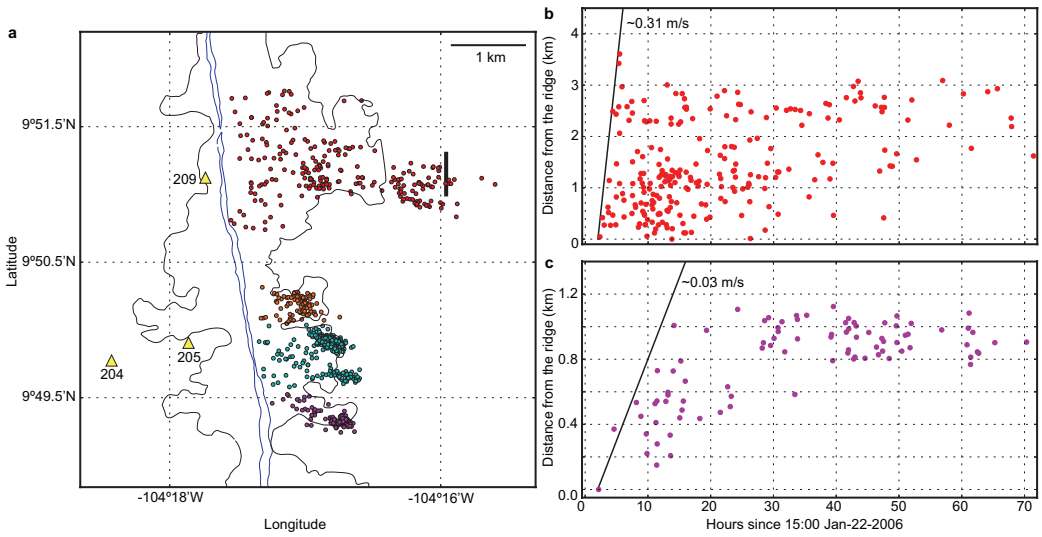

Figure 3: Lava flow velocities. a, Location of seismometers (yellow triangles labelled with station numbers) and impulsive lava events (coloured dots) in the four flow lobes [17] (thin black outline enclosing the lava flow). The AST [17] is shown as a thin blue line. b, c, Impulsive lava events in the northernmost flow lobe propagated farther off-axis at a faster rate than events in the southernmost flow lobe. At later times, events were concentrated at the toe (on the right) of the flows. Migration of other flow lobe events is shown in Fig. S5. No spatiotemporal trend was observed for the flow to the west of the ridge axis, possibly because we missed many events in the first hour of the eruption (see Methods). The first events we located in the western flow lobe are already more than a kilometre off-axis (Fig. S2a).

lobes show initial migration away from the ridge axis before concentrating at the toe of the flows (Fig. 3, Fig. S2a), is also consistent with lava freezing over as it reaches the seafloor and forming subsurface lava channels that allow subsequent flows to propagate off-axis [42]. These events could be generated by explosions from magma degassing [53] or the interaction of lava with seawater [54] as lava reaches the seafloor, and are consistent with evidence for explosive activity at 9° 50' N during the 1991–1992 eruption [42].

These lava events were detected starting 22 January 2006 and lasted for about a week, with about 85% of the located events occurring during the first two days

(Fig. S2b). This suggests that most of the lava erupted rapidly in the first 48 h and unequivocally dates the eruption to January 2006 rather than 2005–2006. With an estimated 22 × 106 m^3 of lava erupted [17], this gives an average eruption rate of around 100 m^3 s^{-1}. This is much lower than the eruption rate of 103 m^3 s^{-1} to 106 m^3 s^{-1} derived from numerical modelling [55] for the less voluminous 1991–1992 eruption [17], despite the melt from both eruptions being derived from the same mantle source [34]. Assuming that the lower eruption rate corresponds to a lower magma driving pressure, this suggests that tectonic stress may be important in initiating the 2006 eruption.

In the two years leading up to the eruption, earthquake activity rate gradually ramped up [16]. The limitations of the small surviving OBS array mean that our earthquake locations are largely restricted to within a small area between 9°49.8'N and 9°51.1'N and from the axial summit trough (AST) to approximately 2 km west of the axis (Fig. 1c). In the hours preceding the eruption, earthquakes in this area ruptured an eastward-dipping structure that goes down to approximately the depth of the AML near 9°50.5'N (Fig. S3). The structure might represent a zone of developing normal faults that were activated by the build-up of magma pressure [34] or tectonic stress [56] since the last eruption. The build-up of stress is also indicated by the increasing magnitude of these local earthquakes in the hour preceding the volcanic crisis (Fig. S4), which culminated in a cluster of T-wave earthquakes of body-wave magnitudes Mb 2–3.5 near 9°50.5'N (Fig. 1a) that was detected by a regional hydrophone array [22].

Fifteen minutes after the first T-wave earthquakes near 9°50.5'N, a series of long-

period events were detected around the same region (Fig. 2). These signals have a dominant frequency around 1.6 Hz. Long-period events are regularly observed preceding volcanic eruptions and have been suggested to originate from a resonating source in a fluid-filled conduit or crack [57]. These events are located (see Methods) west of the ridge axis within our seismic array (Fig. 1c). We did not find any long-period events that are not detected by all stations. This suggests that similar signals are unlikely to occur just outside the array. These long-period events are the largest-amplitude signals detected by the OBSs throughout their deployment. Seismic reflection studies after the eruption have shown melt bodies up to a kilometre off-axis in the region [58]. Therefore, these long-period events might reflect dike initiation from the western edge of the AML, consistent with models that suggest that diking might initiate at the edge of a magma lens [59]. The first T-wave earthquakes occurred before the long-period events, which suggests that the faults could have breached through to the AML and initiated magma movement [56].

The long-period events started near 9°49.5'N and migrated about 4 km northward over the next 30 min, terminating at 9°51.3'N near a break in the AST [17] and the AML [20] (Figs 1c and 2). These events may reflect flow instabilities as magma rises vertically from the magma lens while the AML ruptures northward (Fig. 4), or lateral dike propagation along the segment that terminated at a stress barrier [60]. The along-axis extent of long-period events matches that of the melt-depleted section of a deeper magma lens (sub-AML) underlying the top AML (Figs 1c and 2) imaged post-eruption [19]. This suggests that the rapid draining of this segment of the AML might have induced recharge from the underlying sub-AML [19] (Fig. 4). Lava first

reached the seafloor in this region around 2 h after the first T-wave earthquakes (Fig. 2). This implies that magma rose from the AML starting at a depth of around 1.5 km (ref. 6) at a rate of about 0.21 m s^{-1} (see Methods). The seismicity in this central segment peaked and stopped before the start of the long-period events swarm (Fig. 2). This suggests that the spreading episode started with faulting that triggered magma movement, and not the reverse. This is different from the 1978 Krafla event, where the main earthquake swarm started after a peak in continuous tremor [39], and from the 2005 Afar event, where earthquake swarms continued after a peak in sporadic tremors and ultralong-period events [40].

The T-wave earthquakes subsequently clustered to the south and north of 9°50.5'N (Fig. 2), encompassing the entire eruption area and beyond [22]. This is unlikely to represent lateral dike propagation because that would require an unrealistic propagation rate of approximately 14–32 m s^{-1} [22]. Therefore, we infer that the earthquake clustering reflects almost-concurrent faulting that was probably promoted by the static stress change from the diking event near 9°50.5'N. This suggests that the plate boundary was close to failure owing to the build-up of tectonic stress over the 14 years or so since its last spreading episode [56]. Our observation differs from those at spreading episodes at Afar and Iceland, where dikes propagated laterally for tens of kilometres over multiple weeks [38–41]. Although these T-wave earthquakes were the largest earthquakes in the region during this period, we were not able to identify them on the OBSs, probably owing to the high seismic noise amplitude during this period and their locations farther away and outside our OBS array (Fig. 2).

The rupturing of the ridge axis then triggered vertical magma movement from the

underlying, segmented AMLs [20, 34] (Fig. 4). Immediately after lava first reached the seafloor at the central segment between 9°49'N and 9°51'N, impulsive lava events at the adjacent segment to the north show a northward migration of about 5 km at a rate of 1.07 m s^{-1}, terminating at the end of the AST [17] (Fig. 2). This reflects either dike propagation triggered by rupturing of the ridge axis or lava flowing northward within the AST. About 45 min later, lava started erupting in the northernmost region (Fig. 2) from off-axis fissures approximately 600 m east of the AST [17], fed by a different AML [34]. The northernmost region has a slower inferred magma ascent rate of about 0.14 m s^{-1} (see Methods).

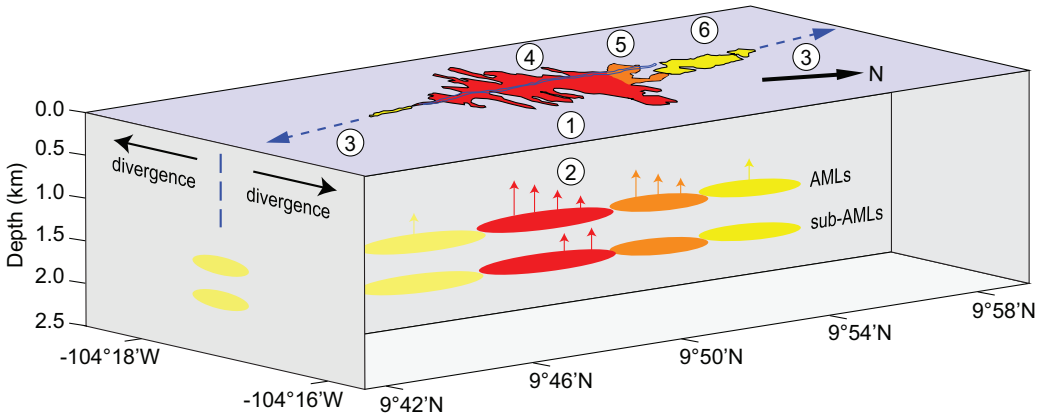

Figure 4: Schematic representation of the dynamics of seafloor spreading at the East Pacific Rise. Numbers 1–6 mark the inferred processes represented in Fig. 2. (1) Build-up of stress culminated in plate rupture (T-wave earthquakes). (2) This triggered magma movement (long-period events) from the underlying melt-rich AML (red ellipse) which then induced recharge from a deeper sub-AML [19]. (3) The static stress change then promoted rupturing (clustering of T-wave earthquakes) beyond the initiation region (blue dashed arrows) owing to the build-up of tectonic stress to a critical level at the plate boundary. (4) Lava first erupted (impulsive lava events) in the central segment. (5) Lava then erupted from a different AML [20] (orange ellipse) at the adjacent segment. (6) Finally, the rupturing triggered magma from another isolated [34] AML (yellow ellipse) to rise vertically at a slower speed and erupt with a smaller volume.

1.5 Discussions and Conclusions

The location of the first T-wave earthquakes and long-period events suggests that the eruption initiated near 9°50.5'N. This region has the highest density of active high temperature hydrothermal venting [61], is near the location of the largest flow lobe from this eruption [17], overlies a drained sub-AML imaged post-eruption [19], and has generally been considered the focus of magmatic activity and upwelling. The lavas from this region also have the highest MgO lava compositions of this eruption, suggesting relatively hot melt in the underlying AML [34]. The impulsive lava events from the flow lobe near this region propagated farthest off-axis at the fastest speed of about 0.31 m s^{-1} (Fig. 3b) compared to the events in the smaller lobes to the south that propagated at about 0.03 m s^{-1} (Fig. 3c, Fig. S5b and c). This shows that this region had the highest lava effusion rate during the eruption, consistent with the presence of high-flow-rate morphologies [35]. Post-eruption seismic imaging showed that the AML underneath this 5-km-long segment is the most melt-depleted [18], indicating that this is where most of the erupted lava was sourced from. Geochemical modelling suggests that the spreading episode was not triggered by renewed injection of magma into the underlying AML [34], unlike at Krafla in 1978 and at Dabbahu in 2005 [31]. However, the initiation at this segment may be due to long-term build-up of magma pressure [34] or tectonic stress [56] since the last eruption.

Static stress change associated with the diking then promoted almost-concurrent rupturing along at least 35 km of ridge axis, triggering eruption of melt sourced from multiple AMLs [20, 34]. The less voluminous flows north of 9°54' N and south of 9°48'

N (Fig. 1b), where lava did not even flow over the AST [17], might reflect a relatively lower magma driving pressure from the underlying, isolated AMLs. Disruption in vent temperatures as far south as 9°42' N [17] suggests that faulting may have happened even farther south without lava reaching the surface, consistent with the southernmost T-wave earthquakes on 22 January 2006.

The variable along-axis magma ascent rates and erupted lava volumes support that the multiple underlying AMLs are segmented [20] and thus unlikely to be concurrently critically stressed from build-up of magma pressure. Instead, the build-up of tectonic stress to a critical level probably allowed almost-concurrent faulting along at least 35 km of the ridge segment, which then triggered magma movement. This is consistent with a model in which the AMLs are surrounded by hot asthenosphere and hence too weak to maintain large magma overpressure or support large elastic stress differences from the low strain rate of plate pull. The high strain rate of faulting is thus needed to breach through to the AMLs to trigger magma movement [56]. Therefore, we can conclude that spreading along at least 30 km of the 35-km-long ridge segment ($>$ 85%) happened owing to build-up of tectonic stress. If plate pull dominates at this magmatically robust fast-spreading ridge, it could also dominate at intermediate- and slow-spreading ridges, which generally have relatively lower magma supplies. Therefore, while MORs are often described as volcanoes that erupt owing to build-up of magma pressure [21, 34], our study demonstrates that eruptions at MORs are a fundamentally different process largely controlled by tectonic stress due to plate pull. MORs could be viewed less as volcanoes and more as tears in the crust where magma reaches the surface when plates are pulled apart.

1.6 Acknowledgements

Y.J.T. thanks W. R. Buck for discussions and reading of the manuscript. Y.J.T. thanks A. H. Barclay and R. S. Matoza for discussions. We thank R. P. Dziak and D. R. Bohnenstiehl for providing the T-wave earthquake catalogue. We thank the captains, crews and science parties of the RV Knorr and RV Atlantis. This work was supported by NSF grant OCE-0961594. We thank J. Karson and V. Schlindwein for their contribution to the peer review of this work.

1.7 Supplementary Figures

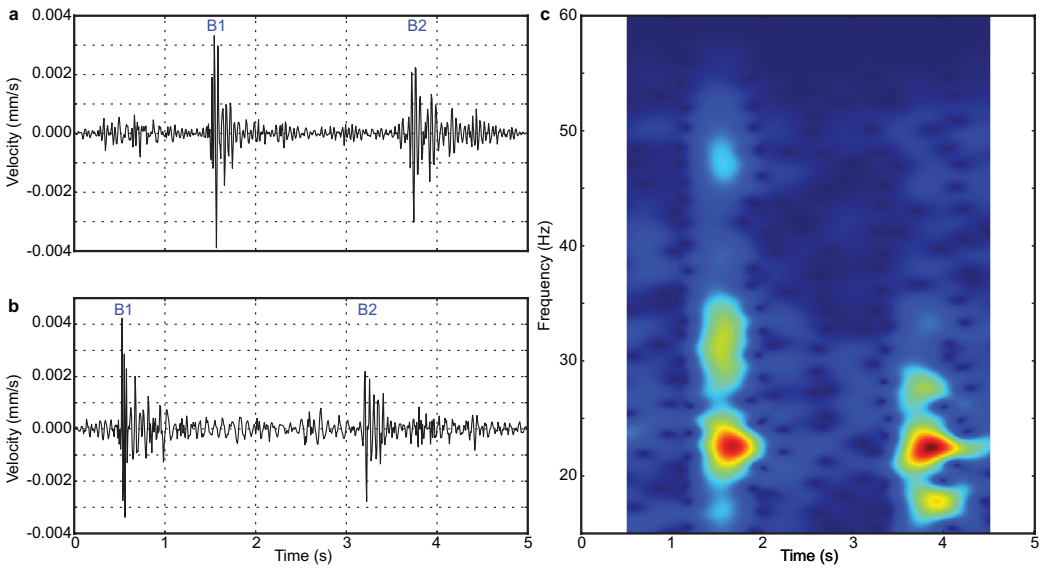

Figure S1: Impulsive lava event signals. a, b, Velocity seismograms of the same event recorded at two different stations. The difference in station relative arrival time of >1 s for the first arrival suggests a waterborne arrival (that is, the seismic wave travelled through the water column rather than through the crust), since these stations are around 2 km apart, with water velocity being 1.5 km s^{-1} and P-wave crustal velocity being around 4–5 km s^{-1} [49]. The event also has multiple arrivals: the first arrival represents a signal that has bounced off the sea surface once (B1) and the second arrival represents a signal that has bounced off the sea surface twice (B2) (Fig. S2b). c, The signal shows a dominant frequency of about 22Hz.

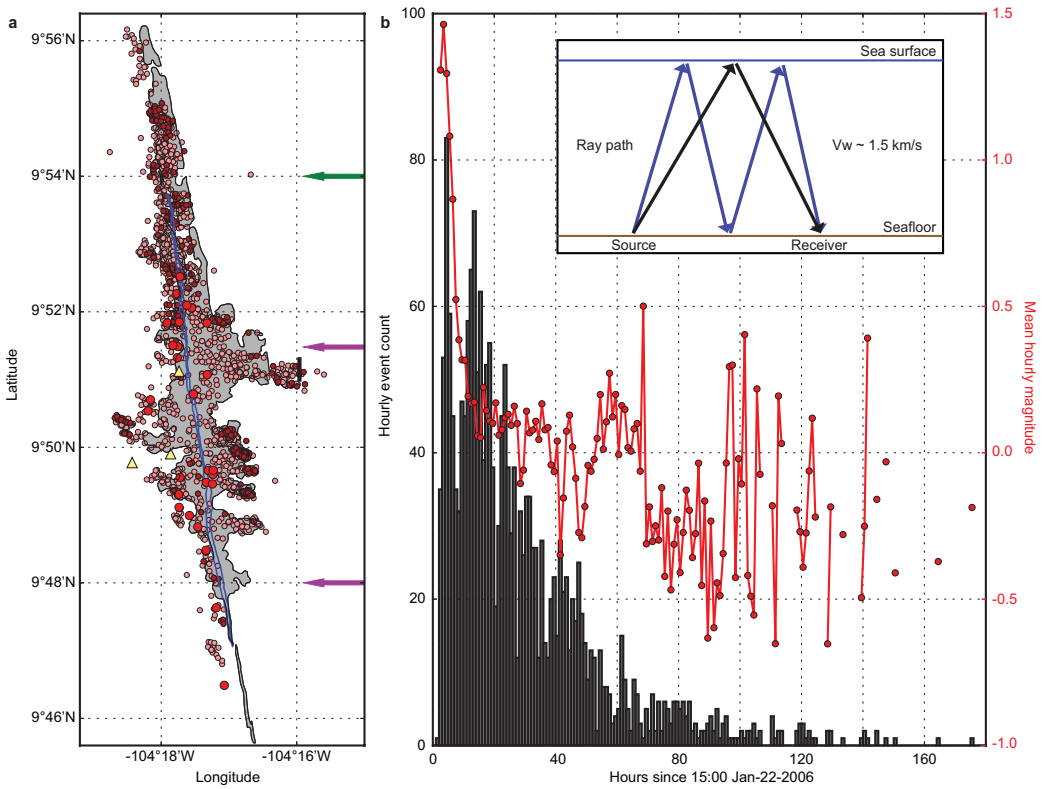

Figure S2: Impulsive lava events. a, Location of seismometers (yellow triangles) and impulsive lava events in the first hour (red), first two days (pale red), and last five days (dark red). The AST [17] is shown as a thin blue line with green arrow marking its end. The bold black line marks revised 2006 lava flow farther off-axis than originally identified [35]. AML disruptions (purple arrows) were inferred from seismic reflection studies post-eruption [20]. b, Histogram of hourly impulsive lava event rate. The red line shows hourly average impulsive lava event magnitude. Mid-ocean-ridge basalt on the East Pacific Rise has been found to have low volatile content [62]. Therefore, the larger-magnitude impulsive lava events during the first 5 h might be driven by excess degassing of volatiles from a larger reservoir of unerupted magma [63], consistent with the estimate that <15% of the available magma in the AML was erupted [17]. The lava has also been suggested to have degassed from supersaturated conditions owing to a rapid magma ascent rate from depth [64]. The breaks in the red line are due to hours when there are no events located, and hence no average magnitude data point. Event magnitudes were calculated as the logarithm of the displacement (in micrometres) multiplied by the signal travel distance (in kilometres), which is different from earthquake magnitude. The inset shows the model of the signal travel path used in locating the impulsive lava events (V_w is the velocity of the seismic wave travelling through the water column). A direct waterborne arrival is not recorded, probably because of the upward refraction of energy due to increasing velocity with water depth. The lack of crustal arrival indicates a small absolute magnitude.

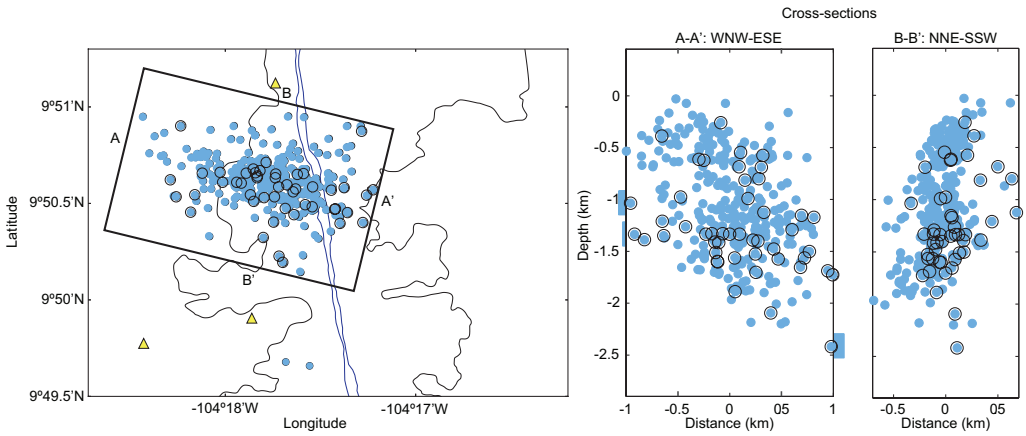

Figure S3: Earthquake locations. The A–A' depth slice shows a 1-km-thick east-southeast (ESE)-dipping structure towards the ridge axis. The B–B' depth slice shows that the structure is subvertical in this direction (that is, north-northeast to south-southwest, NNE–SSW) with a width of around 500 m. Earthquakes occurred between 13:30 and 20:00 on 22 January 2006, mostly in the first two hours. The 50 largest-magnitude earthquakes are highlighted with black circles.

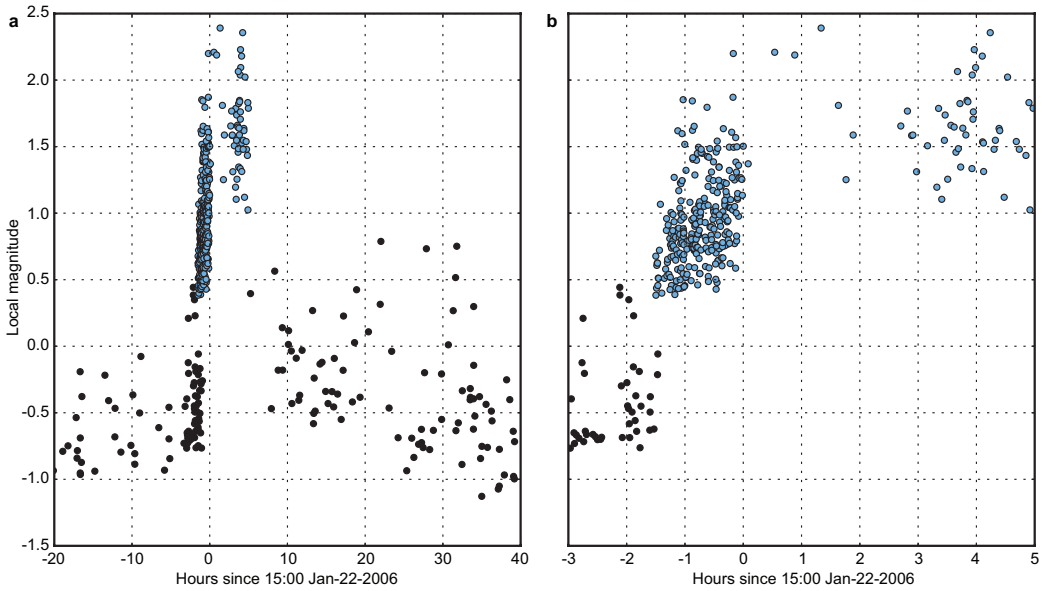

Figure S4: Local magnitude of earthquakes. a, Earthquakes show increasing local magnitude M_L with time in a two-hour period leading up to the eruption. Blue dots represent earthquakes during the eruption period analysed in this study in detail while black dots represent earthquakes over a longer period. b, An 8-h zoom-in on panel a, demonstrating a clear trend of increasing magnitude immediately before plate rupture.

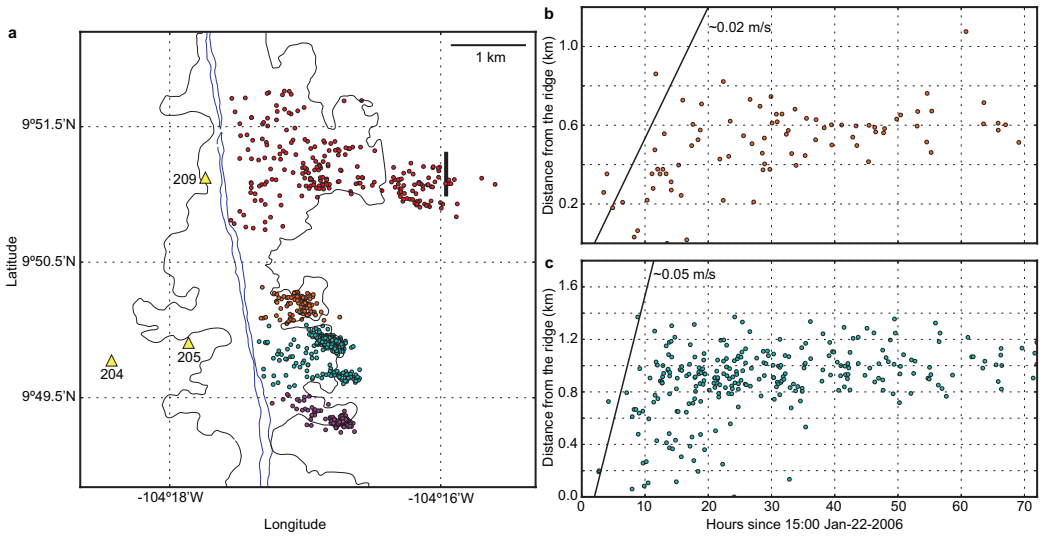

Figure S5: Lava flow velocities. a, Location of seismometers (yellow triangles labelled with station numbers) and impulsive lava events (coloured dots) in the four flow lobes [17] (thin black outline enclosing the lava flow). The bold black line marks the revised extent of the 2006 lava flow farther off-axis than originally identified [35] (see legend to Fig. 1). b, c, Propagation of impulsive lava events off-axis in two flow lobes.

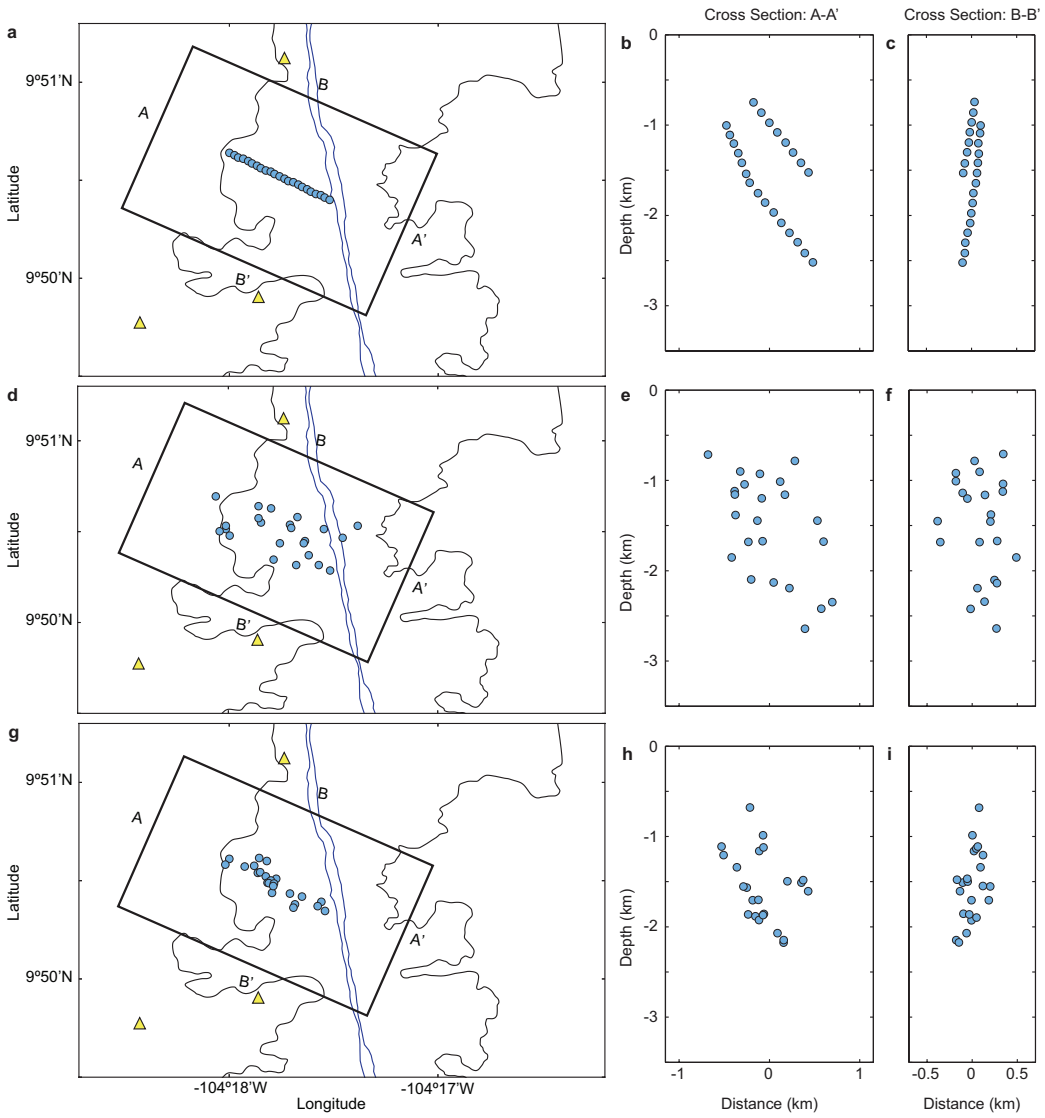

Figure S6: Synthetic test of earthquake locations. a–c, Actual locations of synthetic sources. d–f, Locations of synthetic sources with normally distributed noise of standard deviation 200 m added. These are used as the initial locations for double difference relocation. g–i, Relocated locations of synthetic sources. Events were relocated using synthetic arrival time with normally distributed noise of standard deviation 0.01 s added.

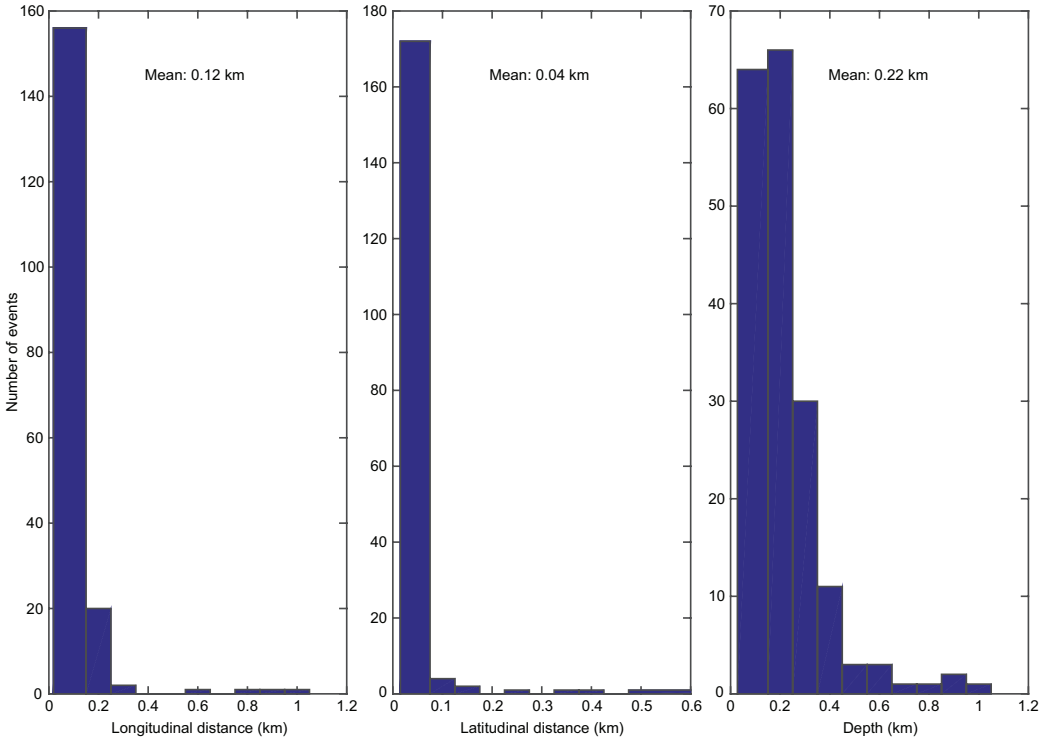

Figure S7: Earthquake relative location errors. Distribution of least-squares errors for the relative locations in longitudinal distance, latitudinal distance and depth.

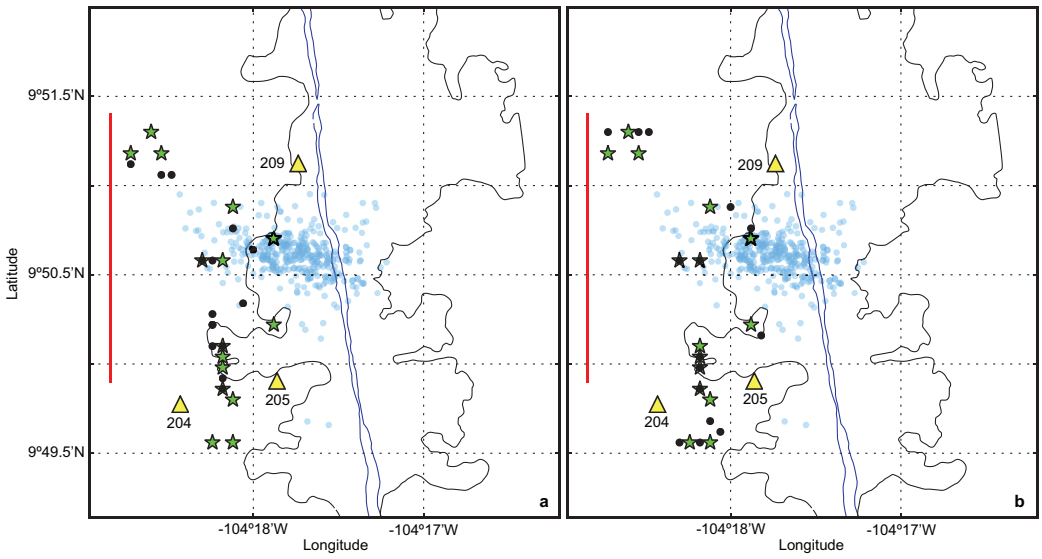

Figure S8: Long-period event locations. a, Long-period event locations assuming 0 km depth (black dots) and 1.5 km depth (green stars), assuming a constant crustal velocity of 2.5 km s^{-1}. The red line marks the extent of melt-depleted sub-AML [19]. Although location depth cannot be definitively determined, the 1.5-h time gap between the initiation of long-period events and melt reaching the surface strongly supports a deeper source. b, Long-period event locations assuming a constant crustal velocity of 2.5 km s^{-1} (green stars) and 2.9 km s^{-1} (black dots) assuming 1.5 km depth. Regardless of the depth and velocity used, events generally cluster near the western edge of the melt lens and bound the area of sub-AML depletion. Faint blue dots represent local earthquake locations (Fig. 1c) for reference.

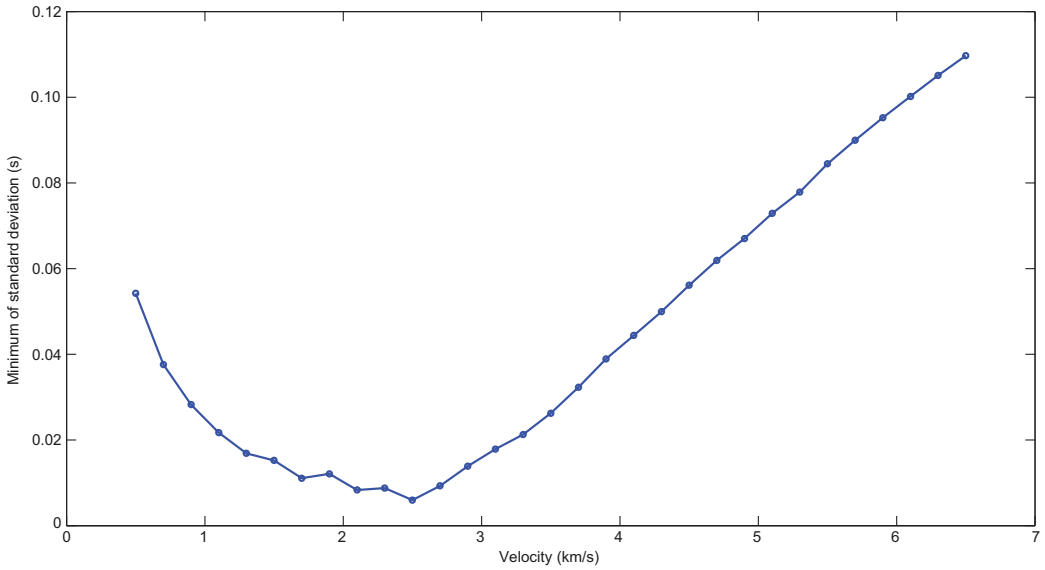

Figure S9: Long-period event velocity assumption. Minimum of standard deviation for different guess (modelled) velocities, assuming a depth of 1.5 km. The overall minimum of the standard deviation occurs at a velocity of 2.5 km s^{-1}.

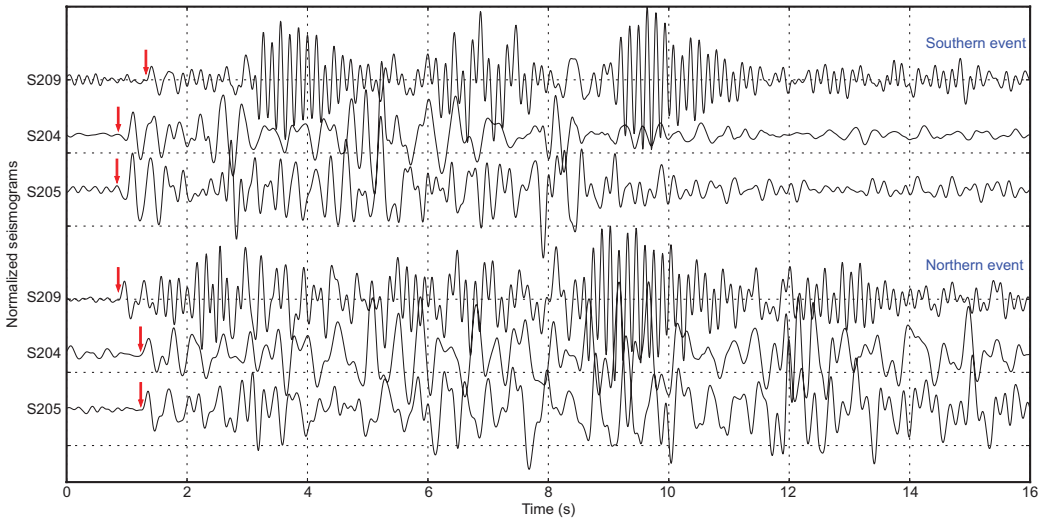

Figure S10: Waveforms of long-period events. Waveforms of two separate events at all three stations low-pass filtered at 5Hz. Red arrows mark the first arrivals. Both event signals arrived at stations S204 and S205 at the same time. This constrains the location of these events to the west of the ridge axis, between these two stations. The event to the south arrived first at S204 and S205 before S209. The event to the north arrived first at S209 followed by S204 and S205. This constrains the northward migration of the long-period events.

Chapter 2

Tidal triggering of microearthquakes over an eruption cycle at 9°50'N East Pacific Rise

This chapter has been published in the following paper:

Tan, Y. J., Tolstoy, M., Waldhauser, F. & Bohnenstiehl, D. R. Tidal triggering of microearthquakes over an eruption cycle at 9°50'N East Pacific Rise. *Geophysical Research Letters* **45** (2018).

2.1 Abstract

Studies have found that earthquake timing often correlates with tides at mid-ocean ridges and some terrestrial settings. Studies have also suggested that tidal triggering may preferentially happen when a region is critically stressed, making it a potential tool to forecast earthquakes and volcanic eruptions. We examine tidal triggering of ∼100,000 microearthquakes near 9°50'N East Pacific Rise recorded between October 2003 and January 2007, which encompasses an eruption in January 2006. This allows us to look at how tidal triggering signal varies over an eruption cycle to examine its utility as a forecasting tool. We find that tidal triggering signal is strong but does not vary systematically in the 2+ years leading up to the eruption. However, tidal

triggering signal disappears immediately post-eruption. Our findings suggest that tidal triggering variation may not be useful for forecasting mid-ocean ridge eruptions over a 2+ years timescale but might be useful over a longer timescale.

2.2 Introduction

Studies on whether the periodic stress change of ∼1 kPa produced by tidal forcing modulates global earthquake timing have produced conflicting results [e.g., 65]. Nevertheless, studies have found that earthquake timing correlates with tides for certain environments such as mid-ocean ridges [3, 15, 24, 25, 66, 67], shallow thrust faults [67–69], and volcanic regions [70, 71]. In subduction zones, studies have also suggested that tidal triggering of earthquakes appears in the years preceding some large earthquakes and disappears after[28–30, 72]. Therefore, tidal triggering may happen preferentially when a region is critically stressed [3, 24, 28–30, 72], making it a potential tool to forecast earthquakes and volcanic eruptions.

The East Pacific Rise (EPR) is a fast-spreading mid-ocean ridge (> 9 cm yr^{-1} at the full spreading rate). Near 9°50'N EPR, a seafloor spreading event in January 2006 ruptured at least 35 km of the ridge axis [22, 73]. The eruption was preceded by 2+ years of increasing seismicity rate [16] and was inferred to be largely controlled by the buildup of tectonic stress to a critical level instead of magma overpressure in the underlying magma reservoirs [73]. Looking at microearthquakes recorded between October 2003 and April 2004, ∼2 years before the eruption, [24] showed that microearthquake timing at this site correlates with semidiurnal tides, occurring

preferentially near times of peak volumetric extensional stress. Subsequent detailed analyses showed systematic spatial variations in earthquake tidal triggering (phase lag relative to times of peak volumetric extensional stress) that is consistent with pore-pressure perturbations generated by ocean tidal loading propagating through a hydrothermal system with heterogeneous permeability structure [26, 27].

Looking at microearthquakes recorded between October 2003 and January 2007, [25] subsequently showed that microearthquake timing also correlates with fortnightly tides. While true fortnightly tides have amplitudes of only about 10% that of semidiurnal tides [74], fortnightly modulations of diurnal and semidiurnal tides have amplitude ranges comparable to semidiurnal tides. [25] found that the microearthquakes occurred preferentially during times of increasing volumetric extensional stress before the eruption, and during times of decreasing volumetric extensional stress after the eruption.

In this study, using ∼100,000 microearthquakes recorded from 2+ years before to ∼1 year after the eruption, we look at how the microearthquakes' response to semidiurnal tides changes over an eruption cycle at 9°50'N EPR to examine its utility as a forecasting tool.

2.3 Methods

Microearthquakes

From October 2003 to January 2007, up to 12 ocean bottom seismometers (OBSs) were deployed and recovered approximately annually in a 4×4 km region near 9°50'N EPR [16] (Fig. 1). The four deployments were from October 2003 to April 2004, April 2004 to May 2005, May 2005 to April 2006, and April 2006 to January 2007. For deployment 3, because of multiple instrument losses and technical failures, there were four stations operating from May to July 2005, two stations from July to October 2005, and three stations from October 2005 until the end of the deployment (Fig. 1). When only two stations were operating, no earthquakes were located.

$\sim$100,000 microearthquakes were located for all four deployments using a cross-correlation-based double-difference method [48, 49]. Local magnitudes (M_L) were derived from peak displacement amplitude with attenuation and station correction terms applied. The magnitude of completeness is M_L -0.7 for deployment 1 and M_L -1.0 for deployment 2-4. $\sim$33,000 events are above the magnitude of completeness (M_c), with the largest event of M_L 2.2.

The microearthquakes are inferred to be a result of hydrothermal cracking as well as fracturing from magmatic and tectonic stresses [23]. Although previous studies in this region have found a range of focal mechanism solutions (normal, thrust, strike-slip) [49, 75], we believe the extension-dominated environment means that the earthquakes likely consist of predominantly crack-opening and/or normal faulting events. The seismicity delineates an along-axis oriented hydrothermal circulation cell and

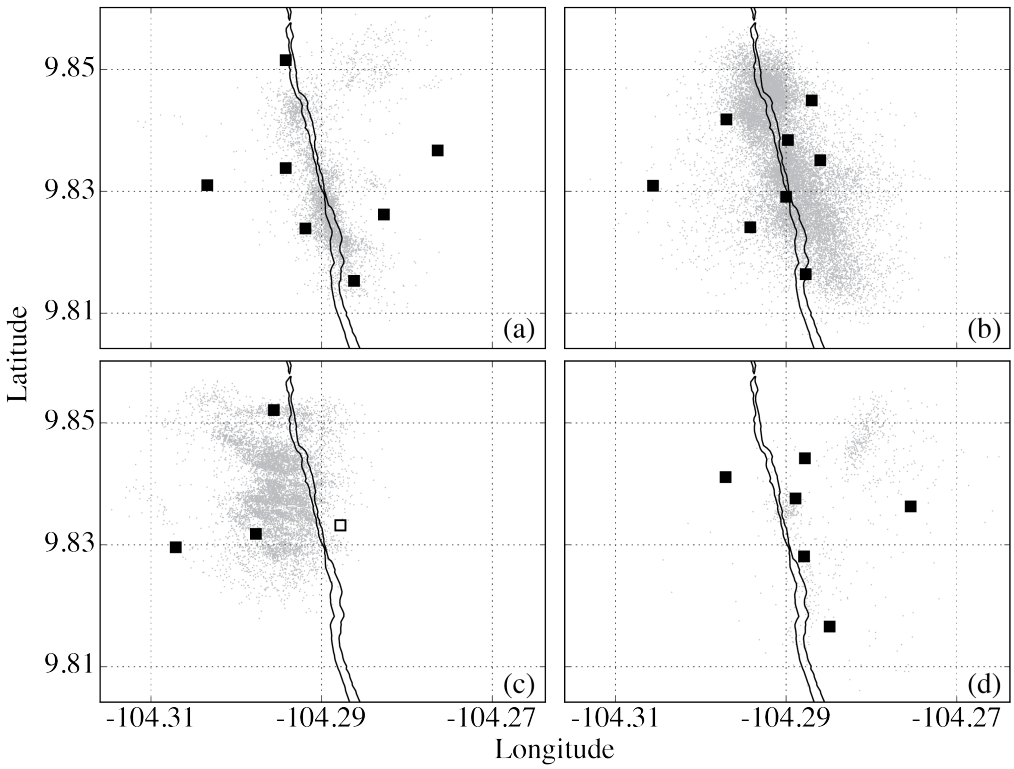

Figure 1: a–d, Locations of microearthquakes above Mc for deployments 1–4. Station locations are shown as filled black squares. Open black square shows station that only operated from May to July 2005 in deployment 3. Axial summit trough is shown as a thin black line [17].

mostly concentrates above the axial magma chamber at 1.5 km depth [23, 49]. The seismicity rate increased in the 2+ years leading up to an eruption in January 2006 and decreased substantially post-eruption [16, 73]. Deployment 3 has significantly fewer instruments because many were lost to the lava flow and unrelated instrument failure. Therefore, earthquakes located in deployment 3 are concentrated west of the ridge axis, reflecting an OBS array that primarily covered the northwest flank of the study area (Fig. 1).

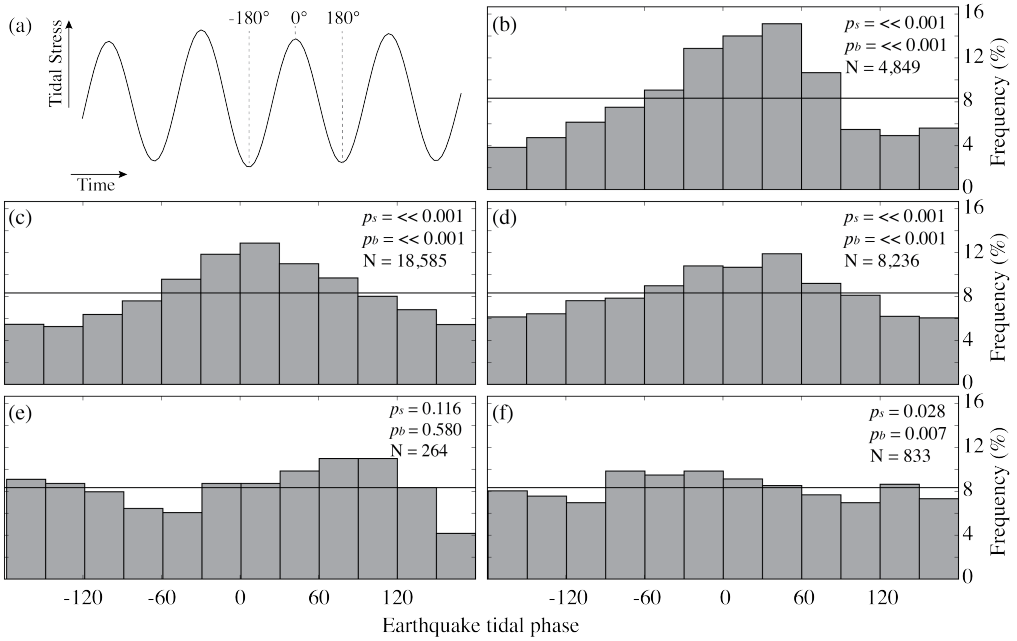

Figure 2: a, Definition of tidal phase. The phase is 0° at peak tidal stress and ranges from −180° at the preceding minimum to 180° at the subsequent minimum. b–f, Frequency distributions of earthquake tidal phases for deployment 1, deployment 2, deployment 3 before the eruption, deployment 3 after the eruption, and deployment 4. Only earthquakes above Mc are included. Horizontal black lines mark the expected frequency distribution if the earthquake times are randomly distributed.

Tidal Stress and Earthquake Tidal Phase

For solid Earth tide, we estimate the horizontal strains using the SPOTL software [76]. We then calculate the vertical strain from the horizontal strains using a plane stress condition assuming a Poisson's ratio of 0.25. For ocean tide, we use the EOT11a ocean tidal model to obtain predicted tidal height for the eight major short-period tidal constituents (K1, K2, M2, N2, O1, P1, Q1, and S2) [77]. We calculate the vertical stress variations from ocean-tidal loading directly from the tidal height, assuming a constant water density of 1025 kg/m^3. We then estimate the horizontal strains from ocean-tidal loading using the SPOTL software, which uses a mass-loading Green's function for strain based on the Gutenberg-Bullen Earth model [76]. Finally, we

convert strain to stress using P- and S-wave velocities as well as density of the top layer of the Gutenberg-Bullen Earth model [78]. Since the tidal wavelengths are very long compared to the microearthquake depths of mostly < 1.5 km, we assume the stresses modeled at the seafloor are not significantly different from those in the earthquake source region.

The mode of failure of shallow microearthquakes (< 1.5 km) in this region is predicted to be tensile or mixed-mode [59]. Therefore, we focus on variations in volumetric stress, which have estimated amplitudes of ± 2.5 kPa, with positive being extensional (Fig. S1). Since our study area is close to an ocean tidal node, tidal stress variation is dominated by the solid Earth tide (Fig. S1 of the supporting information). We then assign a tidal phase to each earthquake based on its origin time relative to the semidiurnal tides. The phase is 0° at peak tidal stress and ranges from -180° at the preceding minimum to 180° at the subsequent minimum (Fig. 2a).

2.4 Results

For deployment 1-3 before the eruption, frequency distribution of earthquake tidal phases clearly shows that microearthquake timing is modulated by semidiurnal tides (Fig. 2). Microearthquakes occur preferentially around times of peak tidal extensional stress (0° phase). We perform the Schuster test to test the null hypothesis that the earthquake times are randomly distributed [79]. We obtain p_s of $<< 0.001$ for deployment 1-3 before the eruption. We also perform the binomial test to estimate the probability p_b of observing different number of earthquakes during times of

encouraging stress, $-90 < \theta < 90$, compared to during times of discouraging stress, $\theta > 90$ and $\theta < -90$, if the earthquake times are randomly distributed. We obtain p_b of $<< 0.001$ for deployment 1-3 before the eruption. Therefore, both the Schuster and binomial tests support our inference that microearthquake timing is modulated by semidiurnal tides before the eruption. This is further supported by examining the frequency of earthquakes as a function of tidal stress amplitude, which shows that for deployment 1-3 before the eruption, earthquake frequency increases systematically with increasing tidal stress (Fig. S2).

For deployment 3 after the eruption, we obtain p_s of 0.116 and p_b of 0.580 (Fig. 2e). Therefore, we cannot reject the null hypothesis that the earthquake times are randomly distributed. However, this change in p-value might be a result of change in sample size since we have significantly fewer number of earthquakes after the eruption. We randomly draw 264 events (with replacement) from deployment 3 before the eruption and calculate p_s and p_b. This is repeated 1,000 times. We obtain p_s and p_b that are smaller than those obtained for deployment 3 after the eruption 96% and 99% of the time. Therefore, this is consistent with the tidal triggering signal disappearing immediately after the eruption. This is further supported by the earthquake frequency not increasing systematically with increasing tidal stress (Fig. S2d).

For deployment 4, we obtain p_s of 0.028 and p_b of 0.007 (Fig. 2f). Frequency distribution of earthquake tidal phases also shows that microearthquakes occur preferentially around times of peak tidal extensional stress (Fig. 2f). The earthquake frequency also increases weakly with increasing tidal stress (Fig. S2e). These are consistent with tidal triggering signal reappearing within a year after the eruption.

Deployment	N_{enc}	N_{dis}	N_T	p-value
1	262	81	343	$<< 0.001$
2	509	178	687	$<< 0.001$
3 before eruption	213	107	320	$<< 0.001$
3 after eruption	57	47	104	0.378
4	178	142	320	0.050

Table 1: Tidal cycle statistics for all deployments. N_{enc} is the number of tidal cycles with more earthquakes during times of encouraging stress, $-90 < \theta < 90$. N_{dis} is the number of tidal cycles with more earthquakes during times of discouraging stress, $\theta > 90$ and $\theta < -90$. N_T is the sum of N_{enc} and N_{dis}. Only earthquakes above M_c were included.

However, when we randomly draw 264 events (with replacement) from deployment 4, calculate p_s and p_b, and repeat this 1,000 times, we obtain p_s and p_b that are smaller than those obtained for deployment 3 after the eruption only 38% and 85% of the time. Therefore, the reappearance of tidal triggering signal in deployment 4 is not a robust feature.

Earthquakes at mid-ocean ridges are dominated by swarm activities. Therefore, our dataset is not amenable to conventional mainshock-aftershock declustering methods. To address the potential effect of swarms on the overall statistics, we look at each semidiurnal tidal cycle and compare the number of earthquakes occurring during times of encouraging stress and discouraging stress. For the null hypothesis that the earthquake times are randomly distributed relative to the semidiurnal tides, this reduces each tidal cycle to the equivalent of one coin flip regardless of the number of earthquakes during the tidal cycle.

For each deployment, we calculate N_{enc}, the number of tidal cycles with more earthquakes during times of encouraging stress, and N_{dis}, the number of tidal cycles with more earthquakes during times of discouraging stress. We exclude tidal cycles

where there are equal number of earthquakes during times of encouraging stress and discouraging stress (∼9% of cycles). We then perform the binomial test to estimate the probability of observing the given N_{enc}/N_T where $N_T = N_{enc} + N_{dis}$, if the earthquake times are randomly distributed. We obtain p-values of $<< 0.001$ for deployment 1-3 before the eruption. This is again consistent with our inference that microearthquake timing is modulated by semidiurnal tides before the eruption.

For deployment 3 after the eruption, we obtain a p-value of 0.378 (Table 1). Since the change in p-value might be a result of change in sample size, we perform a two-sample z-test to evaluate the probability that $N_{enc}/N_T = 213/320$ (deployment 3 before the eruption) and $N_{enc}/N_T = 57/104$ (deployment 3 after the eruption) come from the same population. This yields a z-score of 2.2 with a one-tailed probability of 0.015. Therefore, this is consistent with tidal triggering signal disappearing immediately after the eruption. For deployment 4, we obtain a p-value of 0.050 (Table 1). Therefore, we cannot reject the null hypothesis that the earthquake times are randomly distributed.

Finally, we examine how the microearthquakes' response to semidiurnal tides varies with time. For each semidiurnal tidal cycle, we calculate the percentage of excess events (P_{ex}) [69]:

$$P_{ex} = \frac{n_{ex} - \frac{n_T}{2}}{n_T} \times 100, \tag{2.1}$$

where n_{ex} is the number of earthquakes during times of encouraging stress, $-90 < \theta < 90$, and n_T is the total number of earthquakes. We then compute the median

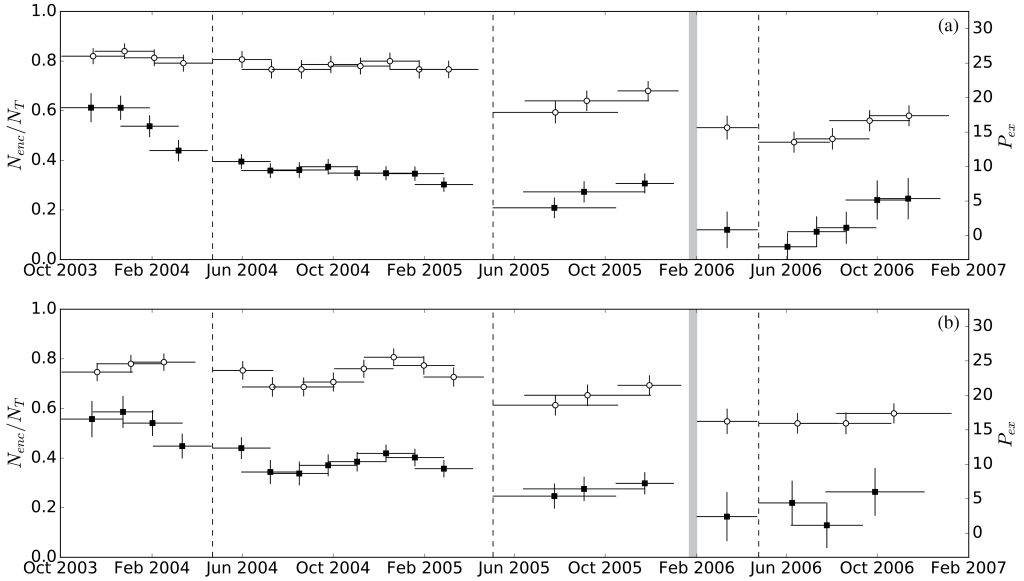

Figure 3: Temporal variation of N_{enc}/N_T (open circles) and P_{ex} (filled squares). Moving windows of 150 semidiurnal tidal cycles, represented by horizontal bars, shifted by 75 tidal cycles. Vertical bars represent 1σ limits estimated based on 1,000 bootstrap samples of the population. Vertical dashed lines mark deployment changes. Gray bar marks the eruption period [73]. a, Full catalog. b, Only earthquakes above M_c

P_{ex} as well as N_{enc}/N_T for moving windows of 150 semidiurnal tidal cycles with 50% overlap (Fig. 3). N_{enc}/N_T should be ∼0.5 if the earthquake times are randomly distributed. We use time windows of 150 semidiurnal tidal cycles to minimize the effect of microearthquake timing being modulated by fortnightly tides [25]. However, we get similar results when using a smaller time window of 100 semidiurnal tidal cycles, but with larger fluctuations (Fig. S3). We examine both the full catalog and the catalog of only earthquakes above M_c to evaluate the temporal variation of P_{ex} and N_{enc}/N_T.

When using the full catalog, N_{enc}/N_T is ∼0.8 for both deployment 1 and 2 (Fig. 3a and S3a). While N_{enc}/N_T falls to ∼0.7 for deployment 3 before the eruption, we think this is likely an effect of changes in earthquake spatial distribution between

deployments due to changes in station coverage (Fig. 1). Compared to deployment 1 and 2, earthquakes located in deployment 3 are concentrated further west of the ridge axis (Fig. 1). However, in deployment 3, N_{enc}/N_T falls to ∼0.6 after the eruption (Fig. 3a and S3a). N_{enc}/N_T remains low initially at ∼0.6 in deployment 4 but increases toward the end of the deployment. N_{enc}/N_T towards the end of deployment 4 is comparable to that of deployment 3 before the eruption, but smaller than that of deployment 1 and 2 (Fig. 3a and S3a). The temporal variation of N_{enc}/N_T is relatively similar when we only examine earthquakes above M_c, but with larger short-term fluctuations (Fig. 3b and S3b).

When using the full catalog, P_{ex} decreases with time in both deployment 1 and 2 (Fig. 3a and S3a). This could reflect weakening of tidal triggering leading up to the eruption due to changes in the dominant forces driving the microearthquakes (magmatic vs. tectonic) [25]. However, this is not a robust feature because we do not observe the same trend when we only examine earthquakes above M_c (Fig. 3b and S3b). Instead, P_{ex} shows short-term fluctuations which could be due to smaller sample size or temporal changes in earthquake spatial distribution. Regardless, in deployment 3, P_{ex} decreases immediately after the eruption (Fig. 3 and S3). P_{ex} remains low initially in deployment 4 but increases towards the end of the deployment. P_{ex} towards the end of deployment 4 is comparable to that of deployment 3 before the eruption, but smaller than that of deployment 1 and 2. The error bars are also larger due to the lower seismicity rate (Fig. 3 and S3). The N_{enc}/N_T plot is generally flatter than the P_{ex} plot because while N_{enc}/N_T is expected to correlate with P_{ex}, this relationship levels off at high P_{ex} (Fig. S4).

2.5 Discussion and Conclusions

When examining temporal variation in tidal triggering signal, it is important to consider changes in earthquake spatial distribution. This is because, at least in our study area, susceptibility to tidal triggering as quantified by P_{ex} varies spatially (Fig. S5). P_{ex} is larger around 9.82°N, an inferred hydrothermal down-flow zone, and smaller around 9.84°N, an inferred hydrothermal up-flow zone [23]. Therefore, especially for deployment 1 and 2 where the differences in array configuration result in an earthquake distribution across areas with very different susceptibility to tidal triggering (Fig. S5), temporal variation in P_{ex} may be due to changes in earthquake spatial distribution.

Our analysis suggests that before the eruption near 9°50'N EPR in January 2006 [16, 73], the microearthquake timing is strongly correlated with the semidiurnal tides. This is consistent with previous studies that found tidal triggering of earthquakes at mid-ocean ridges [3, 15, 24, 25, 66, 67]. The susceptibility of microearthquakes at mid-ocean ridges to tidal triggering may be explained in a few ways. Firstly, the stressing rate due to hydrothermal, magmatic, and tectonic processes may be relatively high, which would lead to a shorter earthquake nucleation time [80]. A short nucleation time relative to the period of tidal stress variation would result in a system that is more susceptible to tidal triggering [81]. However, the occurence of peak seismicity rate during peak semidiurnal tidal stress suggests that the earthquake nucleation times exceed the semidiurnal tidal period and a nucleation-dominated response instead of a simple threshold failure is expected. In the nucleation-dominated response

mode, the response of faults to high-frequency stress change is damped [81]. Alternatively, structural heterogeneities at mid-ocean ridges may result in amplification of tidal stresses, such as adjacent to melt lenses, that are significantly greater than the tidal stresses in a homogeneous elastic medium [82]. Finally, the microearthquakes might be occuring on very weak faults due to the presence of hydrothermal precipitates.

We also observe that the tidal triggering signal disappears immediately post-eruption. This is consistent with observations at Axial Seamount where the strong tidal triggering signal in the four months leading up to its 2015 eruption weakened after the eruption [3]. The disappearence of the tidal triggering signal immediately post-eruption may be explained in a few ways. Firstly, the eruption would have relieved a portion of the accumulated magmatic and tectonic stresses. Therefore, the fault population on average would be further away from their failure threshold. Alternatively, the relative compression adjacent to the dike might have closed cracks in the surrounding regions, preventing water from flowing as quickly through the hydrothermal circulation cell. This would reduce the stressing rate, which would lead to a longer earthquake nucleation time and weaker susceptibility to tidal triggering [81]. However, in the nucleation-dominated response mode, it is unclear from laboratory experiments if the susceptibility to tidal triggering is sensitive to the relative period of earthquake nucleation time and stress oscillation [81].

Finally, we do not observe systematic variation of the tidal triggering signal in the 2+ years leading up to the eruption. This suggests that temporal changes in tidal triggering signal may not be a useful short-term tool to forecast mid-ocean ridge

eruptions. This is supported by [15] observing strong tidal triggering of earthquakes at Axial Seamount in the summer of 1994, four years before it erupted in 1998 [83]. We also observe that the tidal triggering signal might have reappeared within a year after the eruption. However, due to changes in station coverage between deployments, low seismicity rate after the eruption, and the end of our experiment within a year after the eruption, the duration of recovery to full strength tidal triggering after the eruption is not well constrained by our data. Therefore, it is possible that this recovery takes some years and may thus provide some indication of how far along the eruption cycle the site is. This should hopefully be answered in the near future with data from the Axial Seamount cabled observatory where there is long-term seismic monitoring of an active volcano on a mid-ocean ridge.

2.6 Acknowledgements

Y.J.T. thanks Heather Savage and Timothy Crone for fruitful discussions. We thank the captains, crews and science parties of the RV Knorr and RV Atlantis. This work was supported by NSF grants OCE-0961594 and OCE-1536320. Catalogs used here are available from the authors upon request.

2.7 Supplementary Figures

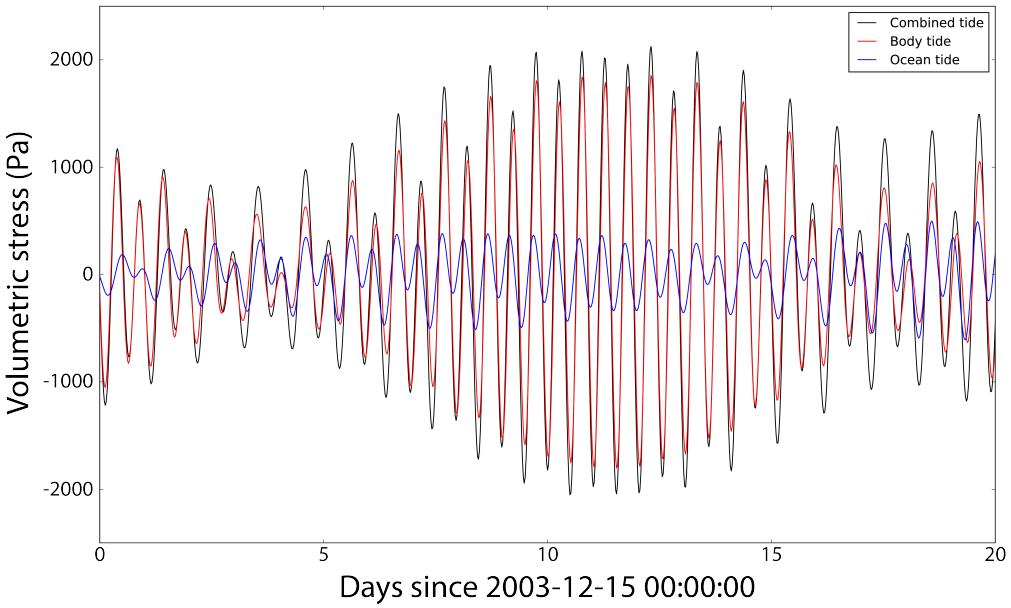

Figure S1: Volumetric stress from solid Earth tide (red), ocean tidal loading (blue), and the combined effect of solid Earth and ocean tide (black)

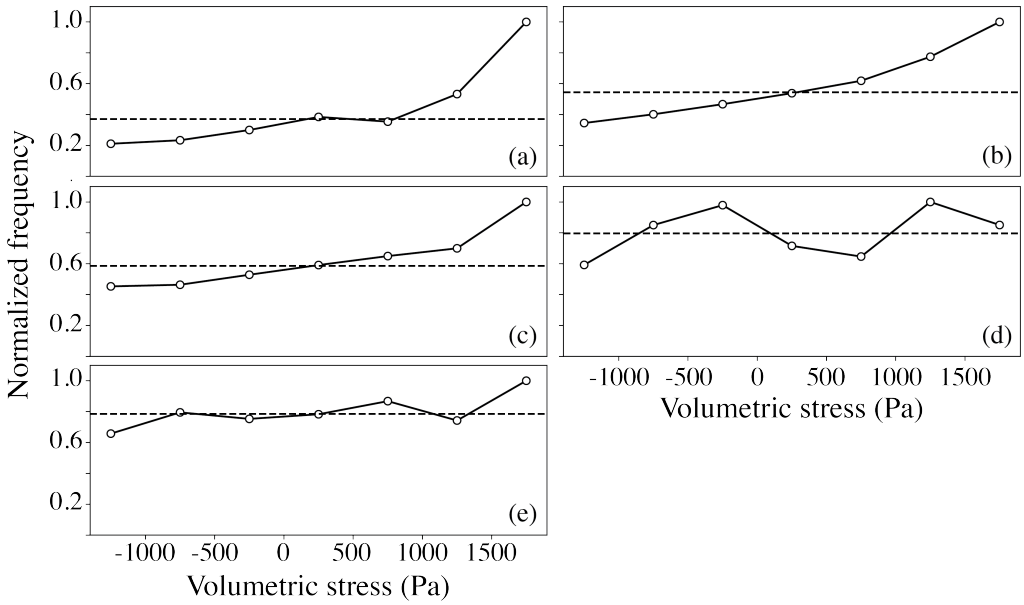

Figure S2: a-e, The normalized frequency of earthquakes (number per hour divided by the maximum number per hour) as a function of tidal volumetric stress in 0.5 kPa bins for deployment 1, deployment 2, deployment 3 before the eruption, deployment 3 after the eruption, and deployment 4 respectively. Dashed lines show the mean normalized frequency of earthquakes. Only earthquakes above M_c are included.

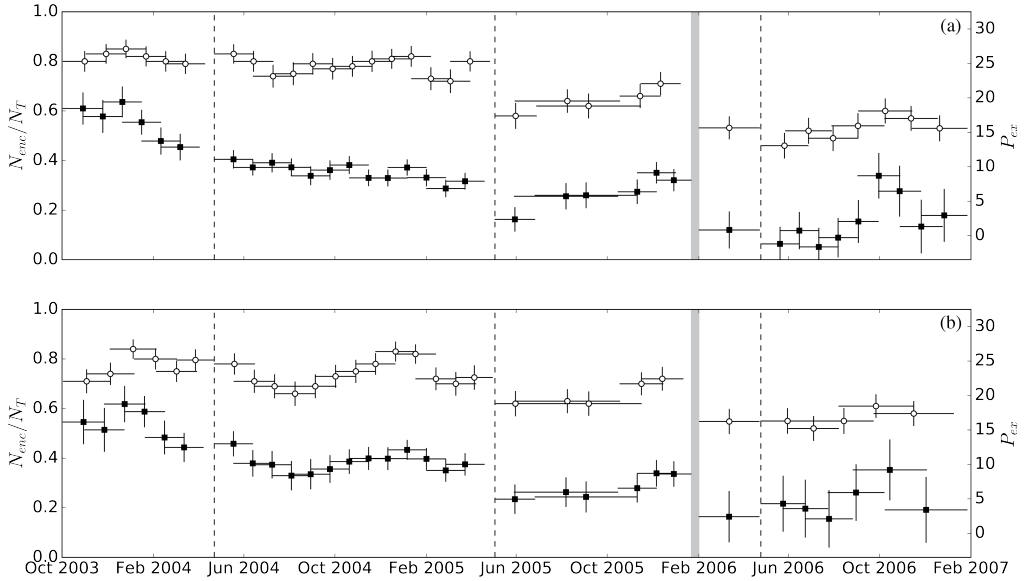

Figure S3: Temporal variation of N_{enc}/N_T (open circles) and P_{ex} (filled squares). Moving windows of 100 semidiurnal tidal cycles, represented by horizontal bars, shifted by 50 tidal cycles. Vertical bars represent 1 limits estimated based on 1,000 bootstrap samples of the population. Vertical dashed lines mark deployment changes. Gray bar marks the eruption period [73]. a, Full catalog. b, Only earthquakes above M_c.

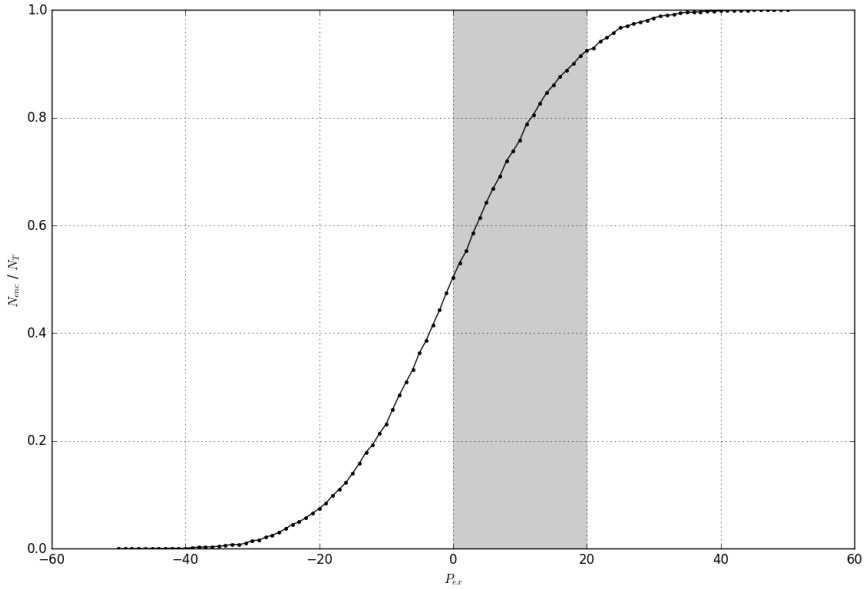

Figure S4: Relationship between N_{enc}/N_T and P_{ex} when events are independent and randomly distributed in time. For each synthetic run, we generate a catalog of 1,000 events randomly distributed over 100 tidal cycles, with a prescribed Pex over the whole time period. We then calculate the N_{enc}/N_T . We do this for a range of prescribed Pex. The plots shows that N_{enc}/N_T and P_{ex} are generally correlated, but Nenc/NT levels off at high P_{ex}. Grey bar marks the range of Pex observed in our study (Fig. 3 and S3).

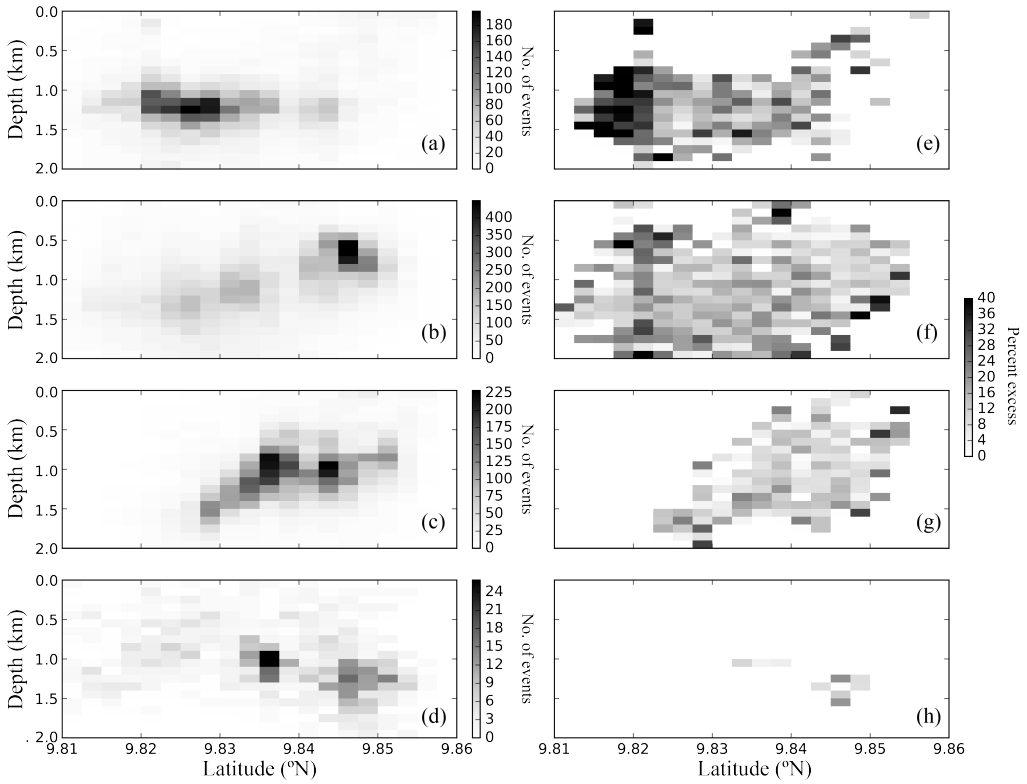

Figure S5: Along-axis 2D spatial variation of a-d, earthquake distribution for deployment 1 to 4 and e-h, P_{ex} for deployment 1 to 4. Only earthquakes above M_c were included. For P_{ex}, only grids with at least 10 events are included

Chapter 3

Axial Seamount: Periodic tidal loading reveals stress dependence of the earthquake size distribution (b value)

This chapter has been published in the following paper:

Tan, Y. J., Waldhauser, F., Tolstoy, M. & Wilcock, W. S. D. Axial Seamount: Periodic tidal loading reveals stress dependence of the earthquake size distribution (b value). *Earth andd Planetary Science Letters* **512**, 39–45 (2019).

3.1 Abstract

Earthquake size-frequency distributions commonly follow a power law, with the b value often used to quantify the relative proportion of small and large events. Laboratory experiments have found that the b value of microfractures decreases with increasing stress. Studies have inferred that this relationship also holds for earthquakes based on observations of earthquake b values varying systematically with faulting style, depth, and for subduction zone earthquakes, plate age. However, these studies are limited by small sample sizes despite aggregating events over large regions, which precludes the ability to control for other variables that might also affect earthquake b values such as rock heterogeneity and fault roughness. Our natural experiment in a

unique seafloor laboratory on Axial Seamount involves analyzing the size-frequency distribution of ∼60,000 microearthquakes which delineate a ring-fault system in a 25 km^3 block of crust that experiences periodic tidal loading of ±18 kPa. We find that above a threshold stress amplitude, b value is inversely correlated with tidal stress. The earthquake b value varies by ∼0.09 per kPa change in Coulomb stress. Our results support the potential use of b values to estimate small stress variations in the Earth's crust.

3.2 Introduction

Earthquake occurrence is primarily controlled by the stress state on fault interfaces. Because *in situ* stress measurements are difficult to obtain, a proxy for estimating the stress state of fault zones through their seismic cycles is valuable for understanding earthquake occurrence and forecasting earthquakes. Earthquakes follow a power-law size-frequency distribution given as $\log_{10}(N) = a - bM$, where N is the number of earthquakes greater than or equal to magnitude M, and a and b are constants [84]. The value a describes the total number of earthquakes while the b value describes the relative frequency of small and large magnitude earthquakes. In rock fracture experiments, acoustic emissions from small cracking events follow the same power-law size distribution [9]. Furthermore, their b values have been found to decrease (larger proportion of large events) with increasing differential stress [9, 85, 86].

The same stress dependence of b value has been inferred to apply to earthquakes. The b value of earthquakes has been found to vary systematically with faulting style

[10], depth [11], and for subduction zone earthquakes, plate age [12]. These observations are consistent with the earthquake b value decreasing with increasing differential stress [87]. However, these studies were restricted to using minimum bins of as few as 50 to 200 earthquakes to calculate the b values, which is barely a large enough sample size to even establish the existence of a power-law distribution [88]. In addition, these studies had to aggregate events over large regions and thus were unable to control for other variables that might also affect earthquake b values such as rock heterogeneity [13] and fault roughness [14]. Establishing whether earthquake b value varies systematically with stress is critical for demonstrating its potential use as a stress meter in the Earth's crust which could help improve forecasting of large earthquakes [89–91] and volcanic eruptions [92].

Tidal forcing on the Earth produces periodic stress changes on the order of several kPa. Studies to establish a correlation between global earthquake rate and tidal stress changes have produced equivocal results [e.g. 65, and references therein] with mainly negative results in continental regions [93, 94]. However, [69] found statistically-significant tidal triggering for shallow, subduction-zone thrust earthquakes where stress changes due to ocean tidal loading can be an order of magnitude larger than the solid earth tides. Even stronger tidal triggering of earthquakes [15, 24, 66] that weakens post-eruption [3, 95] has been documented at mid-ocean ridges. For instance, at Axial Seamount which is located at the intersection of the Juan de Fuca Ridge and the Cobb-Eickelberg hotspot, earthquakes occur preferentially during low ocean height [3, 15]. [96] recently demonstrated that the exponential increase in seismicity rate with tidal stress at Axial Seamount agrees with predictions of both rate-state

and stress corrosion theories [96, Fig. 5], and the long-documented high sensitivity can be explained by the shallow depths of the earthquakes.

As part of the Ocean Observatory Initiative (OOI), a cabled seismic network was installed on the summit of Axial Seamount (Fig. 1a) with time-corrected seismic data streaming from late January 2015 [3]. In the three months before the volcano erupted in April 2015, ∼60,000 earthquakes were located using the double-difference method [48]. The earthquakes delineate an outward-dipping ring-fault system that extends to ∼2-km depth [3] (Fig. 1). The large number of events located within a small region, combined with the earthquakes' sensitivity to tidal stress perturbations [3, 96], make this an excellent natural laboratory to study how the earthquake b value relates to stress changes.

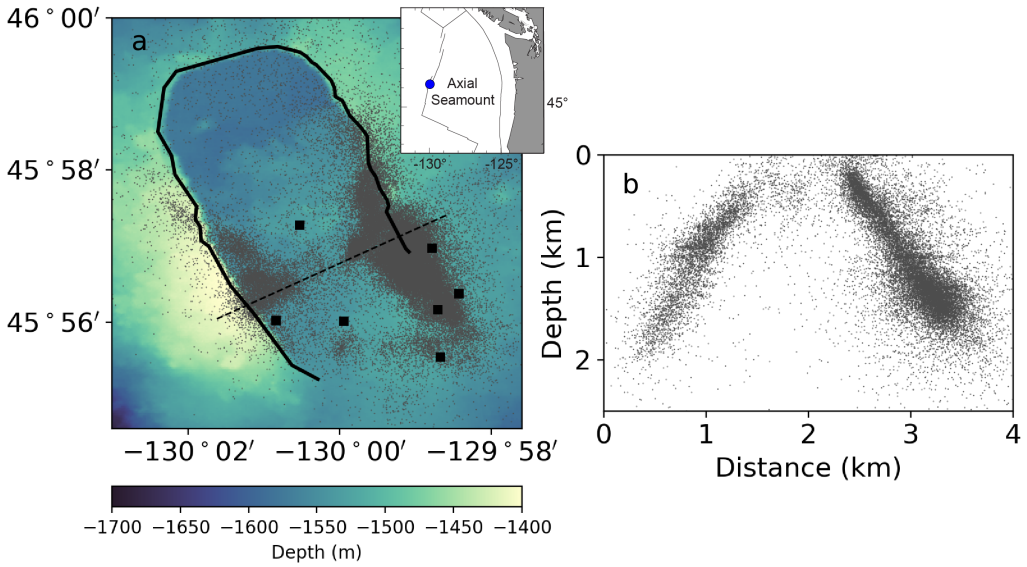

Figure 1: Locations of ∼35,000 earthquakes above $M_c = 0.1$ between January 22nd and April 23rd 2015. a, Bathymetric map with earthquake epicenters (grey dots), seismometers (black filled squares), caldera rim (black line), and the cross section shown in (b) (black dashed line). Inset shows regional location of Axial Seamount. b, Depth cross-section across the caldera showing the projected earthquake locations within 0.5 km of the profile.

3.3 Methods

Earthquake Catalog

In the first year of operation, ∼70,000 earthquakes were located by the OOI Axial seismic network [3]. In the three months before the volcano erupted, the majority of the composite focal mechanisms determined showed normal or oblique-normal sense of motion. During the one-month-long eruption period, the slip direction was reversed as the volcano deflated [8]. After the eruption, the seismicity rate decreased substantially [3, 5] with the focal mechanisms suggesting heterogeneous fault slip directions [8]. Therefore, in this paper, we only examine the ∼60,000 earthquakes that occurred in the three months before the volcano erupted. The earthquake catalog, including the moment magnitudes (M_W) estimated following [97], has been previously published [3].

b Value

We estimate the b values using the maximum likelihood method [98], accounting for the use of binned magnitudes [99]:

$$b = \frac{log_{10}e}{\bar{M} - \left(M_c - \frac{\Delta M}{2}\right)}, \tag{3.1}$$

where M_c is the magnitude of completeness of the data set, $\bar{M}$ is the mean magnitude of earthquakes with magnitude $\geq M_c$, and ΔM is the binning interval of the magnitude, which is 0.1 in this study. We estimate the standard deviation of the b

value estimate following [100]:

$$\delta b = 2.3b^2 \sqrt{\frac{\sum_i^n (M_i - \bar{M})^2}{n(n-1)}}, \tag{3.2}$$

where n is the sample size. We quantify the significance of the b value difference between two groups of earthquakes using Utsu's test [101]:

$$p \approx \exp\left(\frac{-\Delta AIC}{2} - 2\right), \tag{3.3}$$

$$\Delta AIC = -2(N_1 + N_2)\ln(N_1 + N_2) + 2N_1 \ln\left(N_1 + \frac{N_2 b_1}{b_2}\right) + 2N_2 \ln\left(N_2 + \frac{N_1 b_2}{b_1}\right) - 2, \tag{3.4}$$

where p is the probability that the two groups of earthquakes are drawn from the same population, AIC is the Akaike's information criterion, N_1 and N_2 are the number of earthquakes, and b_1 and b_2 are the estimated b values of the two groups of earthquakes. We also compare the b value difference between two groups with their standard deviations [102]:

$$z = \frac{b_1 - b_2}{\sqrt{\sigma_1^2 + \sigma_2^2}}, \tag{3.5}$$

The null hypothesis that two b values come from the same population can be rejected at the 95% confidence level if z exceeds 1.96 and at the 99% confidence level if z exceeds 2.58.

Magnitude of Completeness

We first estimate the magnitude of completeness (M_c) of the catalog using the point of maximum curvature of the frequency-magnitude distribution (FMD) [103], which is equivalent to finding the magnitude bin with the highest number of earthquakes in the non-cumulative FMD [104]. We find $M_c = 0.0$ (Fig. S1). We then estimate M_c using the goodness-of-fit (GFT) method by comparing observed and synthetic cumulative FMDs [105]. We calculate synthetic cumulative FMDs using estimated a and b values of the observed earthquake catalog assuming a range of increasing cutoff magnitudes M_{co}. The goodness-of-fit is quantified using the parameter R:

$$R_{M_{co}} = 100 - \left(100 \frac{\sum_{M_{co}}^{M_{max}} |O_i - S_i|}{\sum_{M_{co}}^{M_{max}} O_i}\right), \tag{3.6}$$

where O_i and S_i are the observed and predicted number of earthquakes in each magnitude bin. M_c is then the first M_{co} where R exceeds a fixed threshold, typically defined at 90% level of fit [105] because real catalogs rarely achieve 95% level of fit [106]. We obtain $M_c = -0.1$ when using a 90% fit threshold and $M_c = 0.1$ when using a 95% fit threshold (Fig. S1). Finally, we estimate M_c base on the b value stability as a function of assumed cutoff magnitude M_{co} [107]. M_c is the first M_{co} at which $|b_{ave} - b| \leq \delta b$ [106], with b_{ave} being the mean of the b values estimated for three successive M_{co} (magnitude range of 0.3 since the bin interval is 0.1) and δb being the standard deviation of the b value estimate [100]. We obtain $M_c = 0.3$ (Fig. S1).

The maximum curvature (MAXC) and the GFT-90% methods can underestimate M_c [106] while the method based on b value stability (MBS) may overestimate M_c

[104]. Therefore, in this study, we adopt $M_c = 0.1$ from the GFT-95% method which leaves us with ∼35,000 earthquakes above M_c and an estimated b value of 1.31 ± 0.01. We also consider the more conservative estimate of $M_c = 0.3$ from the MBS method, which leaves us with ∼20,000 earthquakes above M_c and an estimated b value of 1.39 ± 0.01. The estimated b values are consistent with previous observations of $b > 1$ for normal fault events [10] and in marine volcanic environments [50].

Tidal Stress

We estimate the horizontal strains due to body tides using the SPOTL software which assumes an elastic and spherical Earth (degree-two Love numbers $h = 0.6114$, $k = 0.3040$, and $l = 0.0832$) and computes the tidal strains directly from the positions of the Moon and the Sun [76]. We then calculate the vertical strain from the horizontal strains assuming a plane stress condition:

$$\Delta\epsilon_{zz} = \frac{-\nu}{1-\nu}(\Delta\epsilon_{xx} + \Delta\epsilon_{yy}), \tag{3.7}$$

using Poisson's ratio ν of 0.23 which is consistent with $V_P = 5.4$ km/s, $V_S = 3.2$ km/s, and a density of 2800 kg/m^3. The Poisson's ratio quantifies the effect where a material tends to contract along the axes perpendicular to the axis of tensile strain. For the effects of ocean tidal loading, we first obtain the predicted tidal height for the eight major short-period tidal constituents (K1, K2, M2, N2, O1, P1, Q1, and S2) using the EOT11a global ocean tidal model [77] combined with the Oregon State University regional ocean tidal model for the west coast of the United States [108] as

provided with the SPOTL software. We then calculate the ocean tidal loading effect in two parts. First, we estimate the horizontal strains due to variable regional ocean tidal loading using the SPOTL software, which uses a mass-loading Green's function for strain based on the Gutenberg-Bullen Earth model [76]. We then calculate the vertical strain from the horizontal strains assuming a plane stress condition before converting strains to stresses using elastic constants consistent with a Poisson's ratio of 0.23. Secondly, we estimate the vertical stress perturbation due to direct ocean tidal loading as

$$\Delta\sigma_{zz} = -\rho g h, \tag{3.8}$$

where ρ is the density of seawater (1030 kg/m^3), g is the gravitational acceleration (9.8 m/s^2), and h is the tidal height relative to its mean value. We then estimate the horizontal stresses from the vertical stress assuming uniaxial strain:

$$\Delta\sigma_{xx} = \Delta\sigma_{yy} = \frac{\nu}{1-\nu}\Delta\sigma_{zz}, \tag{3.9}$$

Finally, we combine the various tidal stress components to form the stress tensor. We find that at Axial Seamount, ocean tides are much larger than body tides and hence the vertical tidal stress dominates (Fig. S2). We calculate the tidal-stress time series in 5-minute intervals. We assume the stresses estimated at the seafloor applies to the earthquake source region because the tidal wavelengths are very long compared to the earthquake depths of mostly less than 2 km (Fig. 1b). We do not account for the effect of bathymetry in our tidal stress calculations. The bathymetry only varies by

less than 200 m around our earthquake epicenter region (Fig. 1a) and while it might affect the absolute value of our tidal stress estimates, the relative difference in tidal stress at different times is expected to still be valid.

We assume the earthquakes are predominantly normal faulting events since the ring-fault system appears to have accommodated pre-eruptive inflation [3], 79% (31 of 39) of the composite focal mechanisms determined before the eruption based on first-motion polarity showed normal or oblique-normal sense of motion [8], and this is a region of tectonic extension. This initially seems to contradict the well-documented preferential occurrence of earthquakes during low ocean height at Axial Seamount [3, 15] because a decrease in ocean height (increase in tensile vertical stress) should produce a Coulomb stress change that inhibits slip on normal faults. However, [96] resolved this apparent paradox by accounting for the effect of the underlying magma chamber on the stress distribution. The higher compressibility of the magma chamber means that it will inflate or deflate relative to the surrounding crust in response to tidal stresses and produce Coulomb stress changes on the fault that is opposite in sign as those produced directly by the tidal stresses [96, Fig. 3]. When the magma chamber bulk modulus is below a critical value, the magma chamber effect will exceed that of the direct tidal stress effect and the phase of the tidal triggering gets inverted [96, Fig. 4], as observed at Axial Seamount. Since the vertical tidal stress dominates at Axial Seamount (Fig. S2) and the average Coulomb stress change on the fault can be approximated as $\Delta CFS = \chi \sigma_{zz}$ with χ dependent on the magma chamber bulk modulus [96], we will focus on variations in vertical stress due to the combined effects of ocean tidal loading and body tide. We adopt tension as positive and an increase

in vertical stress represents an increase in encouraging stress (Coulomb stress change that favors slip on normal fault). The vertical tidal stress has estimated amplitudes of ±18 kPa (Fig. S2).

3.4 Results

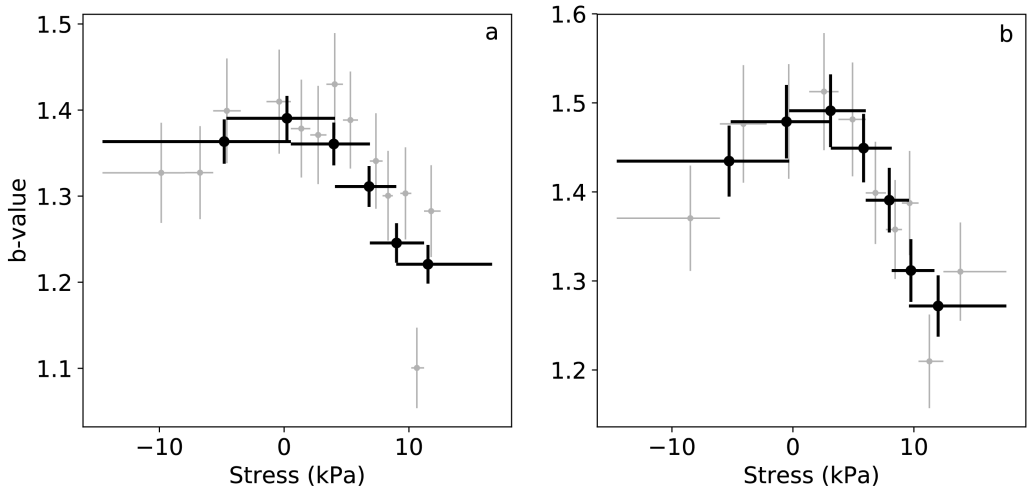

Figure 2: The earthquake b value as a function of tidal stress. The vertical error bars represent two standard deviations of the estimated b values [100]. The horizontal bars represent the range of earthquake tidal stress values included in each bin, with the markers centered at the mean earthquake tidal stress for each bin. a, Using M_c = 0.1. Non-overlapping bins of 2,000 events (gray) as well as moving bins of 10,000 events shifted by 5,000 events (black). b, Using M_c = 0.3. Non-overlapping bins of 2,000 events (gray) as well as moving bins of 5,000 events shifted by 2,500 events (black).

We assign each earthquake a tidal stress value based on its origin time. After sorting the earthquakes based on their associated tidal stress values, we calculate the b values for non-overlapping bins of 2,000 events. When using M_c = 0.1, we also calculate the b values for moving bins of 10,000 events, shifted by 5,000 events. When using M_c = 0.3, we calculate the b values for moving bins of 5,000 events, shifted by

2,500 events. For each bin, we re-estimate M_c using the GFT-95% method and only keep the data point if the re-estimated M_c equals the M_c of the bulk data. Only 4 out of 40 data points did not fulfill the criteria. We find that the earthquake b value only decreases systematically with increasing tidal stress when stress amplitudes exceed a certain threshold (Fig. 2).

We further investigate the relationship between b value and tidal stress by looking at how the b value varies between fixed stress bins. We calculate the b values for non-overlapping bins of 2 kPa for stress values between -8 and 14 kPa. We pick this range because it incorporates ∼91% of the earthquakes (Fig. S3) and allows us to use a reasonably large number of events per stress bin. The number of events vary between stress bins (Fig. S3) so we adopt the following strategy to maintain consistency: For each stress bin, we estimate 1,000 b values using events randomly drawn with replacement from the earthquake population. When using $M_c = 0.1$, we draw 1,600 events for each b value calculation because the stress bin with the smallest number of events contain ∼1,600 earthquakes (Fig. S3). When using $M_c = 0.3$, we draw 900 events for each b value calculation. The reported b value is then the average b value from the bootstrapping. We find that at low stress values, the b values are high but remain relatively constant. However, at stress amplitudes greater than 5 kPa, the earthquake b value decreases linearly with increasing tidal stress at ∼0.03 per kPa (Fig. 3).

We test the statistical significance of the b value variations as follow: Using $M_c = 0.3$, we sort the earthquakes based on their associated tidal stress values before splitting them into two equal-size groups. The lower tidal stress group has a mean

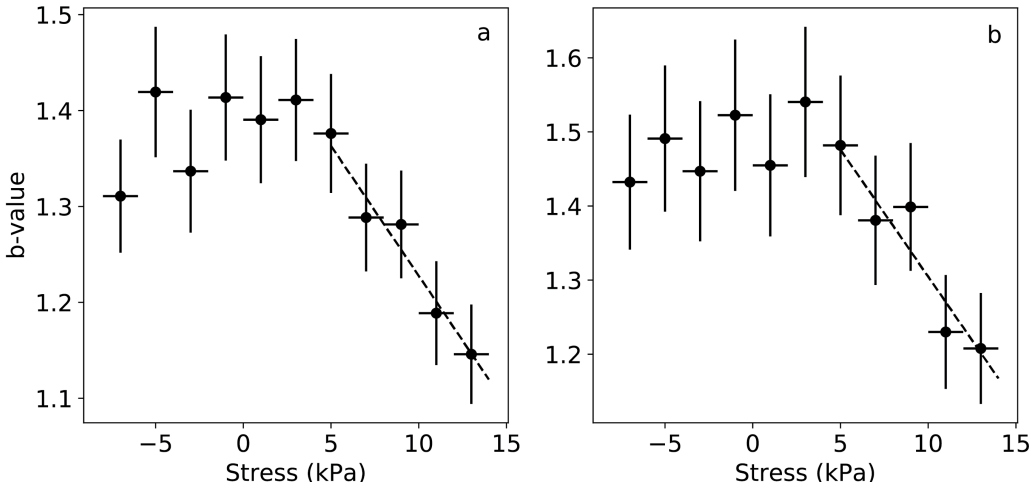

Figure 3: The earthquake b values for non-overlapping stress bins of 2 kPa. The vertical error bars represent two standard deviations of the estimated b values from bootstrapping. The horizontal bars represent the tidal stress range for each bin. Dashed lines represent linear least-squares fits, both giving b value varying by ~ 0.03 per kPa. a, Using $M_c = 0.1$. b, Using $M_c = 0.3$.

stress of -1 kPa while the higher tidal stress group has a mean stress of 10 kPa. We further verified that the lower and higher tidal stress groups both have $M_c = 0.3$. We then plot the cumulative and non-cumulative FMDs. The cumulative FMD curves show increasing separation at larger magnitudes. The non-cumulative FMD curves intersect at around $M_w = 0.5$ (Fig. 4). These results show that the slopes of the FMD curves for the lower tidal stress group is steeper (larger b value) than that of the higher tidal stress group. The lower tidal stress group has a b value of 1.46 ± 0.01 while the higher tidal stress group has a b value of 1.33 ± 0.01. We obtain similar b values and standard deviations from bootstrapping. The b value difference between the two groups are statistically significant at a $<1\%$ level based on both the Utsu's test [101] and the z-test (see Methods).

The FMD curves deviate from linearity at large magnitudes. This could reflect a

real departure from the power law distribution at large magnitudes or simply statistical fluctuations due to under-sampling. To quantify how this affects our results, we repeat the b value calculations after excluding earthquakes of M_w greater than 1.5 where the FMD curves become nonlinear [102] (Fig. 4). The lower tidal stress group now has an estimated b value of 1.53 $\pm$ 0.01 while the higher tidal stress group has an estimated b value of 1.40 $\pm$ 0.01. The b value difference between the two groups remains statistically significant at a <1% level based on both the Utsu's test [101] and the z-test. We also repeat the analysis shown in Fig. 3 and while the absolute b values become larger, we obtain similar trends with the earthquake b value decreasing linearly with increasing tidal stress at $\sim$0.03 per kPa when stress amplitude exceeds 5 kPa (Fig. S4). This is unsurprising because the maximum-likelihood estimate of the b value uses the average earthquake magnitude (Eq. 1) and is therefore only slightly affected by the small number of large magnitude events.

We further verified that the minimum bin sizes often used to document b value variations [10–12] are insufficient to robustly constrain our observed effect. We determine the minimum bin size needed to resolve the b value variations we observe as follow: Using $M_c = 0.3$, we sort the earthquakes based on their associated tidal stress values and split them into two equal-size groups (see Fig. 4). For a range of bin sizes, we then calculate 1,000 b values using events randomly drawn without replacement from the original population. The reported b value is then the average b value from the bootstrapping with the associated uncertainties (Fig. 5). For the b value difference between the lower and higher tidal stress groups to be statistically significant at a <5% and <1% level based on the Utsu's test [101], we need minimum

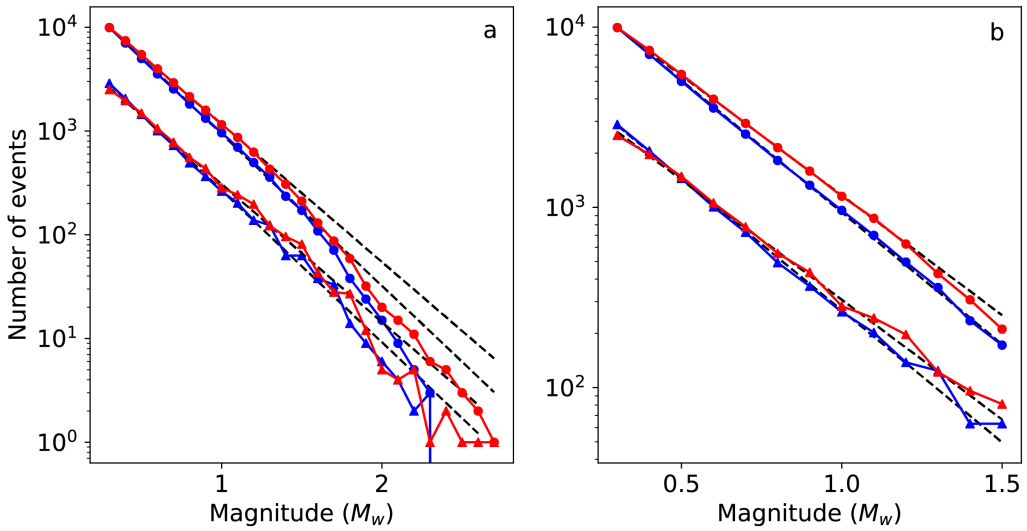

Figure 4: Cumulative (circle) and non-cumulative (triangle) FMDs of two groups of earthquakes. Dashed lines indicate maximum-likelihood fits to the data. a, Using $M_c = 0.3$, the ∼20,000 earthquakes are split into two equal-size groups after being sorted based on their tidal stress values. The lower tidal stress group (blue) has a mean stress of −1 kPa while the higher tidal stress group (red) has a mean stress of 11 kPa. b, Zoom-in of a.

bin sizes of 900 and 1,600 respectively. For the b value difference between the two groups to be statistically significant at a <5% and <1% level based on the z-test, we need minimum bin sizes of 800 and 1,300 respectively.

In multiple continental regions, earthquake b values have been found to decrease with increasing depth which has been interpreted as the result of increasing crustal strength [11] and material homogeneity [13] with depth. We similarly find that at Axial Seamount, the earthquake b value decreases with increasing depth (Fig. S5). Therefore, our observation of b value decreasing with increasing tidal stress could simply reflect the average earthquake depth increasing with tidal stress. While the Chi-squared test suggests the earthquake depth distributions of the lower and higher tidal stress groups come from two different populations, the depth difference is such

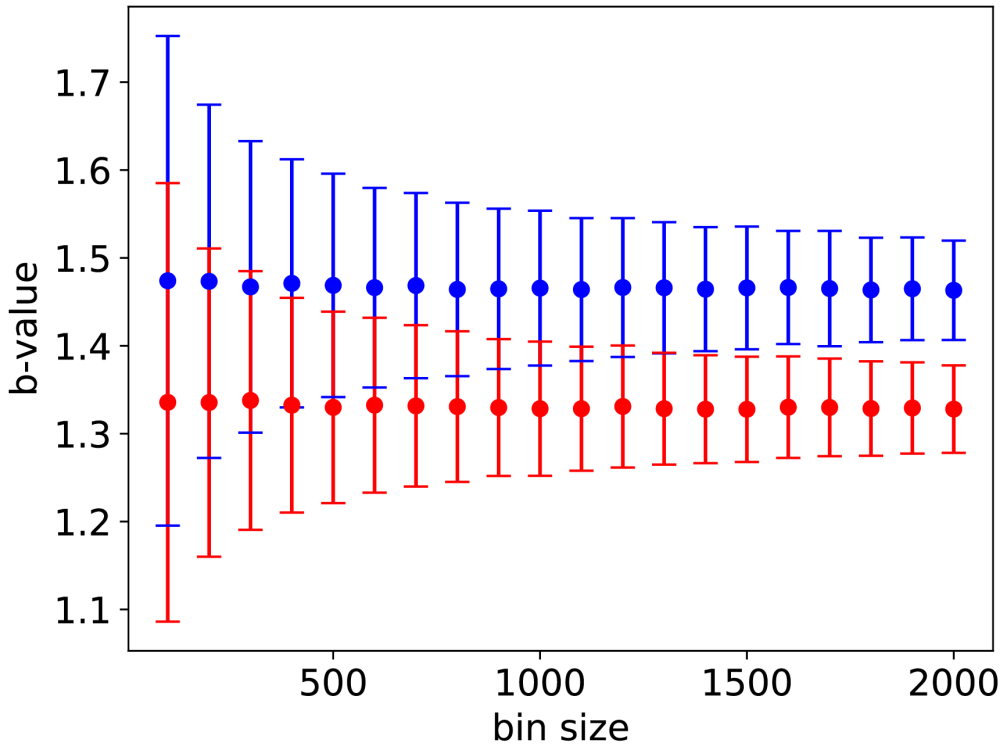

Figure 5: The estimated earthquake b values for the lower (blue) and higher (red) tidal stress groups as a function of bin sizes. For each bin size, we calculate 1,000 b values using events randomly drawn without replacement from the original population. The reported b value is then the average b value from the bootstrapping. The vertical error bars represent two standard deviations.

that the mean and median depths of the higher tidal stress group is shallower by ∼18 m and ∼16 m respectively. We also find that the mean and median earthquake depth decrease with increasing tidal stress (Fig. S6). Since b value decreases with increasing depth, this change in depth distribution would have resulted in b value increasing with tidal stress. Therefore, our observation of earthquake b value decreasing with increasing tidal stress is unlikely to be a secondary effect of change in earthquake depth distribution with tides.

The earthquake spatial distribution of the lower and higher tidal stress groups also differs slightly, with relatively more events on the western and northeastern walls of

the caldera for the lower tidal stress group (Fig. S7). We verify that the b value variation with tidal stress that we observe is still valid at smaller spatial scale as follow: We first bin the earthquakes into 1 km^2 spatial grids and find that there are five bins with more than 1,000 events (Fig. S7c) . For each of these five bins, we sort the earthquakes base on their tidal stress values and split the events into two equal-size groups. We find that for three out of the five bins, the b value of the lower tidal stress group is larger than the higher tidal stress group. However, the statistical significance of the b value differences is not guaranteed by the Utsu's [101] and z-test due to the small number of events in each bin.

3.5 Discussions

[87] calibrated the stress dependence of earthquake b values assuming a simple frictional strength model combined with measurements of b value variation with depth at different tectonic environments [11] and found that b value varies by $\sim$0.001 MPa^{-1}. Our analysis suggests that earthquake b value at Axial Seamount varies by $\sim$0.03 kPa^{-1} (Fig. 3). In a recent tidal triggering study at Axial Seamount, [96] modeled the average Coulomb stress change on the 67° outward-dipping normal faults [8] (Fig. 1) due to vertical tidal stress changes as $\Delta CFS = \chi\sigma_{zz}$, with $\chi = 0.32$ for a realistic magma chamber bulk modulus of 1 GPa. Adopting $\chi = 0.32$ would give us a b value change of $\sim$0.09 kPa^{-1} of Coulomb stress change. Our observation of b value variation that is sensitive to small stress perturbations ($\sim 10^5$ more sensitive compared to [87]) is consistent with the long-documented observations of strong tidal triggering

of earthquakes at Axial Seamount [3, 15] and other mid-ocean ridges [24, 66]. [96] demonstrated that the seismicity rate change with tidal stress at Axial Seamount agrees with predictions of both rate-state and stress corrosion theories, and that the higher sensitivity can be explained by the shallow depths of the earthquakes (and hence the corresponding lower normal stress and stress drop values). The same explanation could apply to our observations since laboratory experiments previously showed that b value variations depend on stress normalized to the maximum failure strength [9]. Our observed greater sensitivity is also consistent with observation of the b value of acoustic emissions in the laboratory varying with tidal stress [109].

While our calibrated b value change with stress cannot be directly applied to other tectonic environments as most catalogued earthquakes occur at deeper depths, a sensitivity that is greater than 0.001 MPa^{-1} [87] could explain observations of b value decreasing preceding large earthquakes [90] and volcanic eruption [92]. Otherwise, these observations would represent stress changes on the order of 100 MPa in the decades before the Tohoku and Sumatra earthquakes [90] and weeks before the Mount Ontake eruption [92]. Alternatively, these documented b value decreases might not have resulted from stress increases. Based on epidemic-type aftershock sequence (ETAS) modeling, [110] suggested that such b value decreases can emerge simply from conditioning of the seismicity having to culminate in a mainshock, which results in there being a growing contribution of a deviatoric power law distribution with a smaller b value to the background unconditional distribution. At Axial Seamount, [111] did not observe a systematic decrease in b value leading up to the April 2015 eruption. [3] similarly did not observe the tidal triggering signal or the seismicity rate

increasing leading up to the eruption. Therefore, the presumed stress accumulation in the three months before the volcano erupted might be too small to be detected with the current dataset.

Our observed stress dependence of earthquake b values can be understood within the same statistical model first proposed to explain why the b values of microfractures in laboratory experiments vary with stress [9]. If we treat the Earth's crust as an inhomogeneous elastic medium experiencing a uniform applied stress, the presence of inhomogeneities means that the stress at each point within the crust is a random variable that follows a probability distribution function that depends on the uniform applied stress. If we further assume that at each point, fracture will occur if the local stress exceeds a critical value and that fractures stop growing when they propagate into a region of lower stress, it follows that a fracture has a higher probability of growing larger when the applied stress is greater [9]. This translates to a decrease in b value with increasing stress. However, the threshold effect that we observe is not well-explained by this model. Nevertheless, a similar threshold effect is often discussed for earthquake triggering from stress changes [112, 113] with the stress threshold being dependent on the fault stiffness [112].

A recent study using global data hinted at a b value-tidal stress correlation, as earthquake b values were found to decrease with increasing tidal shear stress ranking, where an earthquake's ranking is based on the maximum tidal shear stress during the day before the earthquake relative to the daily maxima in the 15 days before the earthquake [114]. However, the relationship was not clear for earthquakes smaller than M_w 6.5 when looking at the Global Centroid Moment Tensor catalogue, poten-

tially due to aggregating events of various faulting styles in diverse tectonic regimes [114]. Due to the lack of a strong correlation between global seismicity rate and tidal stress changes [e.g. 65, and references therein], the authors instead invoke enhanced slow slip during increased tidal stresses that subsequently triggers earthquakes and increases the probability of rupture growth [114]. However, at Axial Seamount, the sensitivity of the earthquakes to small tidal stress changes [3, 15] can be simply explained by the shallow depths of the earthquakes [96] without invoking the existence of slow slip.

3.6 Conclusions

Our natural experiment in a unique seafloor laboratory, looking at the size distribution of earthquakes in a 25 km^3 block of crust that experiences periodic tidal loading, provides a robust validation of the stress dependence of the earthquake b value. We find that above a certain threshold stress amplitude, the earthquake b value decreases linearly with increasing tidal stress. The b value varies by $\sim$0.09 per kPa change in Coulomb stress. This suggests that b value changes can be used to estimate stress variations in the Earth's crust.

3.7 Acknowledgements

Y.J.T. thanks Göran Ekstrom, David Marsan, Meredith Nettles, Christopher Scholz, and Spahr Webb for fruitful discussions. This work was supported by NSF under

grant OCE-1536320. The earthquake catalog used in this study is from [3] and is archived in the Interdisciplinary Earth Data Alliance Marine Geoscience Data System (DOI: 10.1594/IEDA/323843). The authors thank Suguru Yabe and two anonymous reviewers for their construtive comments that improved the manuscript.

3.8 Supplementary Figures

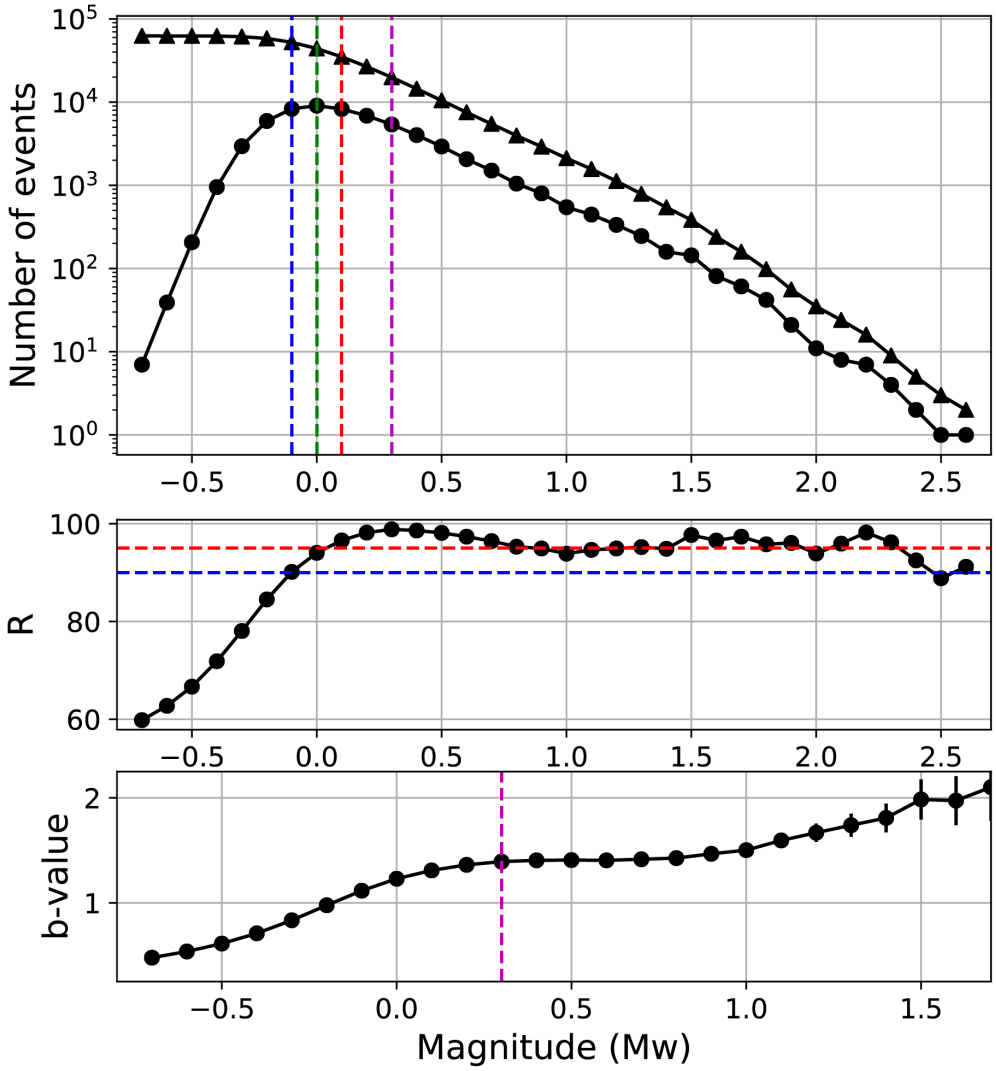

Figure S1: Selection of the minimum magnitude of completeness (M_c). top, Cumulative (triangle) and non-cumulative (circle) frequency-magnitude distributions (FMDs). Dashed lines depict the M_c estimates based on the MAXC (green), GFT-90% (blue), GFT-95% (red), and MBS (magenta) methods. middle, Variation of parameter R used to quantify the goodness-of-fit between observed and synthetic cumulative FMDs for a range of cutoff magnitudes. Dashed lines depict the 90% (blue) and 95% (red) thresholds. bottom, Variation of the b value for a range of cutoff magnitudes. Dashed line depicts where the b value first stabilizes (see Methods).

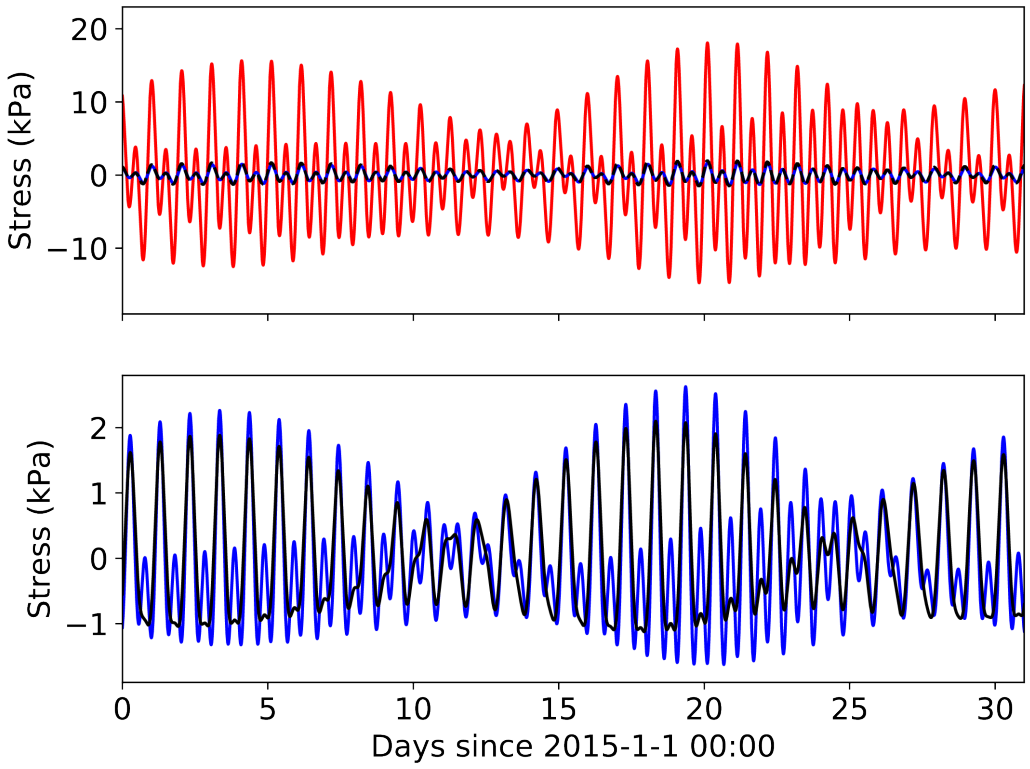

Figure S2: Time series of predicted tides at the surface at 45.95°N, 130.00°W. top, Estimate of σ_{xx} (black), σ_{yy} (blue), and σ_{zz} (red) from ocean tidal loading, with tension being positive (i.e. σ_{zz} is positive upwards). bottom, Body tides. The stress amplitude is about an order of magnitude smaller than that of ocean tides.

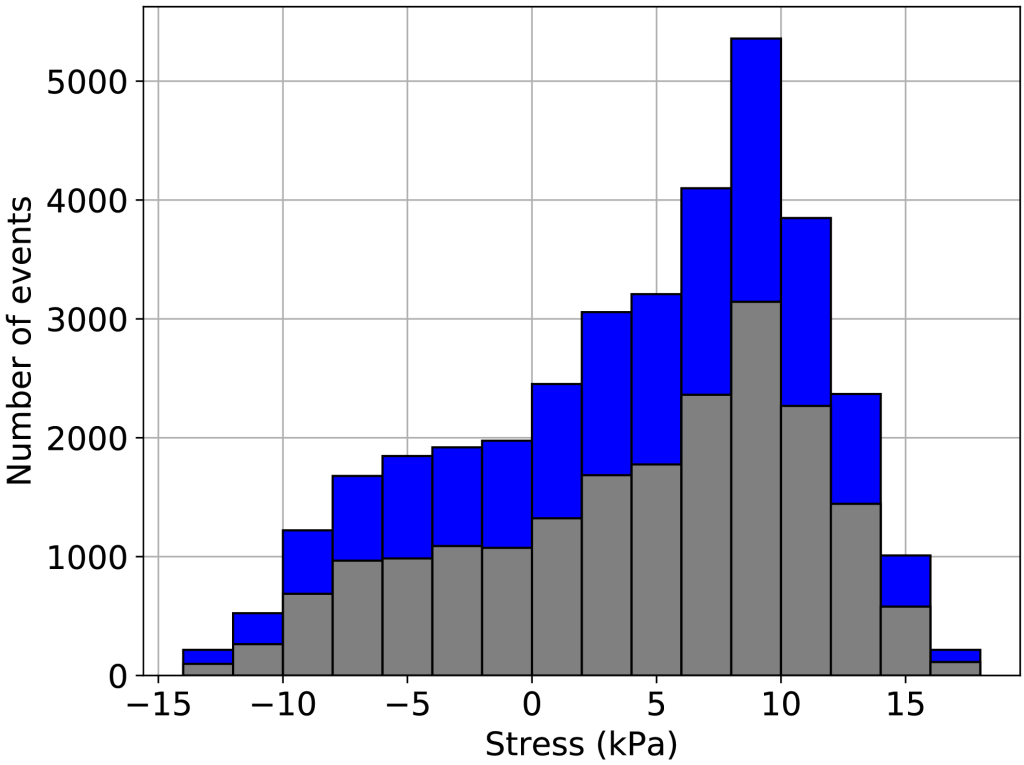

Figure S3: The earthquake tidal stress distribution in bins of 2 kPa for $M_c = 0.1$ (blue) and $M_c = 0.3$ (grey). The distribution reflects the combined effect of seismicity rate increasing with tidal stress [96] and the uneven distribution of tidal stress amplitudes.

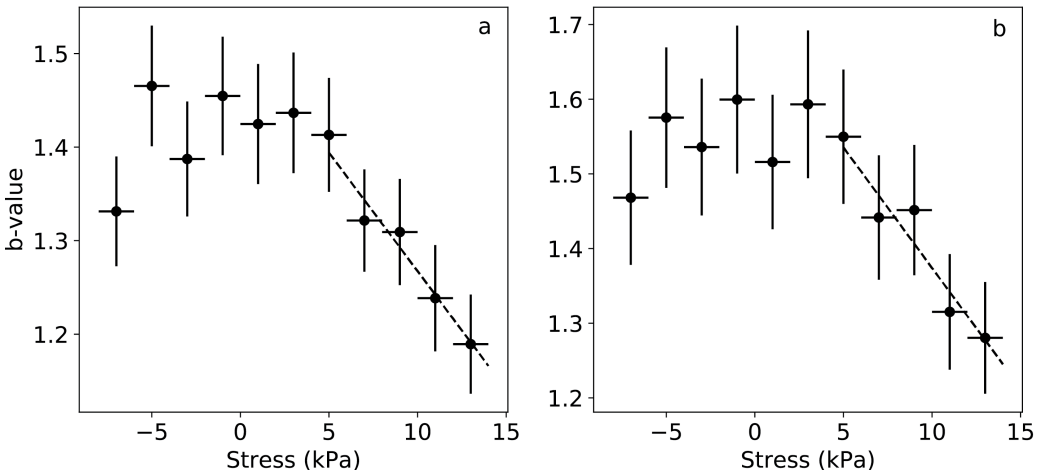

Figure S4: The earthquake b values for non-overlapping stress bins of 2 kPa. Earthquakes of M_w greater than 1.5 are excluded. The vertical error bars represent two standard deviations of the estimated b values from bootstrapping. The horizontal bars represent the tidal stress range for each bin. Dashed lines represent linear least-squares fits, both giving b value varying by $\sim$0.03 per kPa. a, Using $M_c = 0.1$. b, Using $M_c = 0.3$.

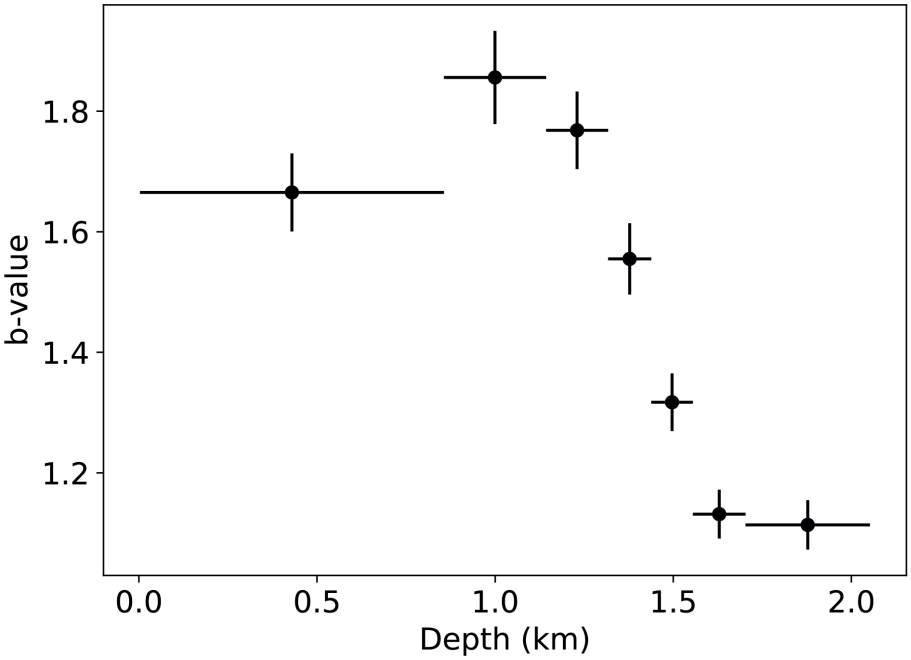

Figure S5: The earthquake b value as a function of depth in non-overlapping bins of 2,500 earthquakes. The vertical error bars represent two standard deviations [100] of the estimated b values. The horizontal bars represent the range of earthquake depth values included in each bin. Since M_c is expected to vary with depth, we estimate M_c for different depth ranges using the GFT-95% method before choosing a fixed M_c = 0.3 to estimate the b values.

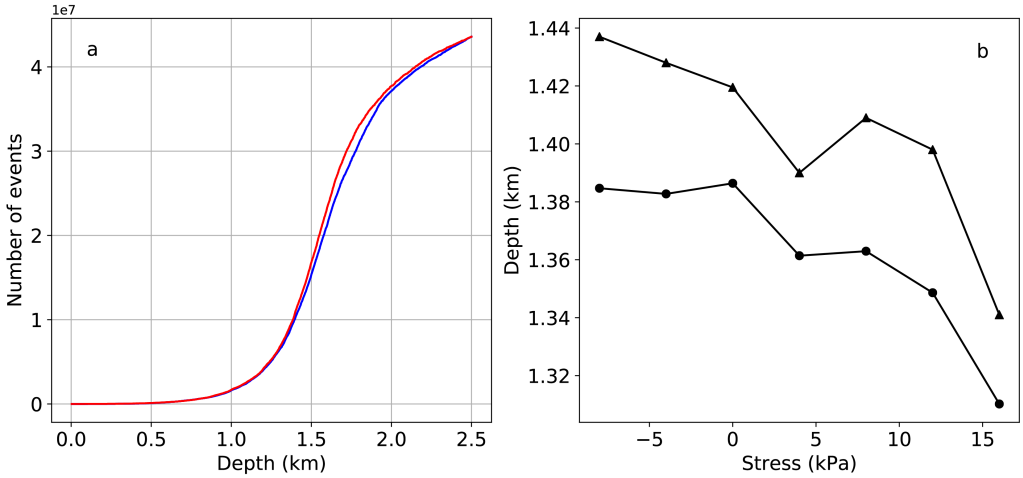

Figure S6: a, Cumulative number of events with depth for the lower tidal stress group (blue) and higher tidal stress group (red) (see Fig. 4). b, Mean (circle) and median (triangle) earthquake depth for non-overlapping stress bins of 4 kPa.

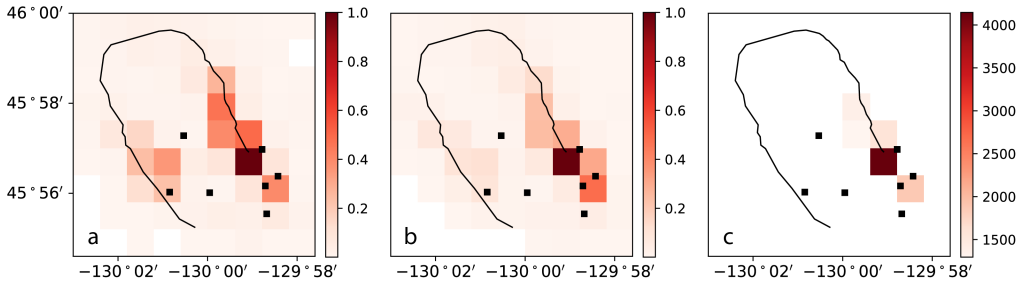

Figure S7: The normalized earthquake spatial distribution in 1 km^2 grids for a, lower tidal stress group and b, higher tidal stress group (see Fig. 4). c, The earthquake spatial distribution in 1 km^2 grids for all events above $M_c = 0.3$. Only grids containing more than 1,000 events are shown.

Chapter 4

Variable rate of melt influx into the shallow reservoir in the months before Axial Seamount's 2015 eruption

4.1 Abstract

How mid-ocean ridge volcanic systems evolve leading up to an eruption remains an open question due to the lack of long-term, continuous monitoring in these environments. A real-time seafloor cabled observatory was established atop Axial Seamount a few months before its most recent eruption in April 2015, providing a unique opportunity to address this question. Here we integrate measurements of seismic velocity variations and the spatiotemporal evolution of earthquakes as well as deformation rate to show that a few weeks before the eruption, there was increased rate of melt influx into a region of the shallow reservoir from which the erupted lavas were subsequently sourced. Our observations also support the interpretation of seismic imaging results of the potential existence of more than one melt pocket in the primarily-mush reservoir. Our results highlight the complexity of the shallow magma reservoir and how melt influx can vary over short time and small spatial scales. Our observation of geophysical precursors weeks before the eruption also suggests that analysis of real-time geophysical data might aid eruption forecasting and facilitate installation

of additional *in situ* instrumentation before future eruptions. This may lead to a better understanding of mid-ocean ridge volcanism.

4.2 Introduction

Earth's volcanism is dominated by eruptions along the ∼70,000-km-long mid-ocean ridge system that is mostly below the sea surface. However, the difficulty in sustaining long-term geodetic and seismic monitoring of submarine ridges means that our limited understanding of the active processes at ridges has mostly been inferred from geophysical observations of the few rifting episodes at slow-spreading ridges on land in Afar (Asal-Ghoubbet 1978; Dabbahu, 2005-2010) and Iceland (Krafla, 1975-1984). However even for these episodes, continuous near-field monitoring of their precursory activity was limited and the geometries of the shallow crustal reservoirs are not well-imaged [31]. Therefore, how the magmatic systems evolved leading up to an eruption remains an open question.

Axial Seamount rises ∼1 km above the surrounding seafloor at the intersection of the intermediate-spreading Juan de Fuca ridge and the Cobb-Eickelberg seamount chain. Its 8.5 km by 3 km summit caldera is underlain by a well-imaged, shallow (∼1.5 km), 14 km by 3 km wide magma reservoir that is up to 1 km thick with variable melt content [1, 2] (Fig. 1a). A new seafloor cabled observatory, which include seismometers and geodetic instruments that span the southern half of the caldera (Fig. 1a), came online a few months before the volcano's most recent eruption in April 2015. The 2015 diking-eruptive sequence involved both northward and southward

dike propagation[3–5]. However, lava only erupted in the northern caldera floor and the north rift zone [6, 7] (Fig. 1a). Earthquakes located delineate outward-dipping faults that are reactivated as the volcano inflates and deflates [3, 5, 8]. Modeling of vertical displacements suggests the presence of a steeply-dipping prolate-spheroid pressure source beneath the southeastern part of the caldera that extends from 1.75 to 6 km depth [4] (Fig. 1b). While the 2015 eruption sequence is well-studied [3–8, 115], it remains unclear whether there were geophysical precursors leading up to the eruption [3].

In this study, we use seismic noise interferometry to measure seismic velocity changes in the caldera edifice with time. We then integrate these results with the spatiotemporal evolution of the seismicity as well as the deformation rate as measured by tiltmeters and bottom pressure recorders (BPRs) to infer how the magmatic system evolved in the months before the eruption.

4.3 Methods

Seismic Interferometry

The cross-correlation function (CCF) of ambient seismic noise recorded at two stations converges to the Green's function which can be used to image the seismic velocity structure of the Earth's subsurface [116]. Since ambient seismic noise is continuously being recorded, studies have further extended the method to detect temporal variation of seismic velocity [117, 118]. The seismic network on Axial Seamount, which

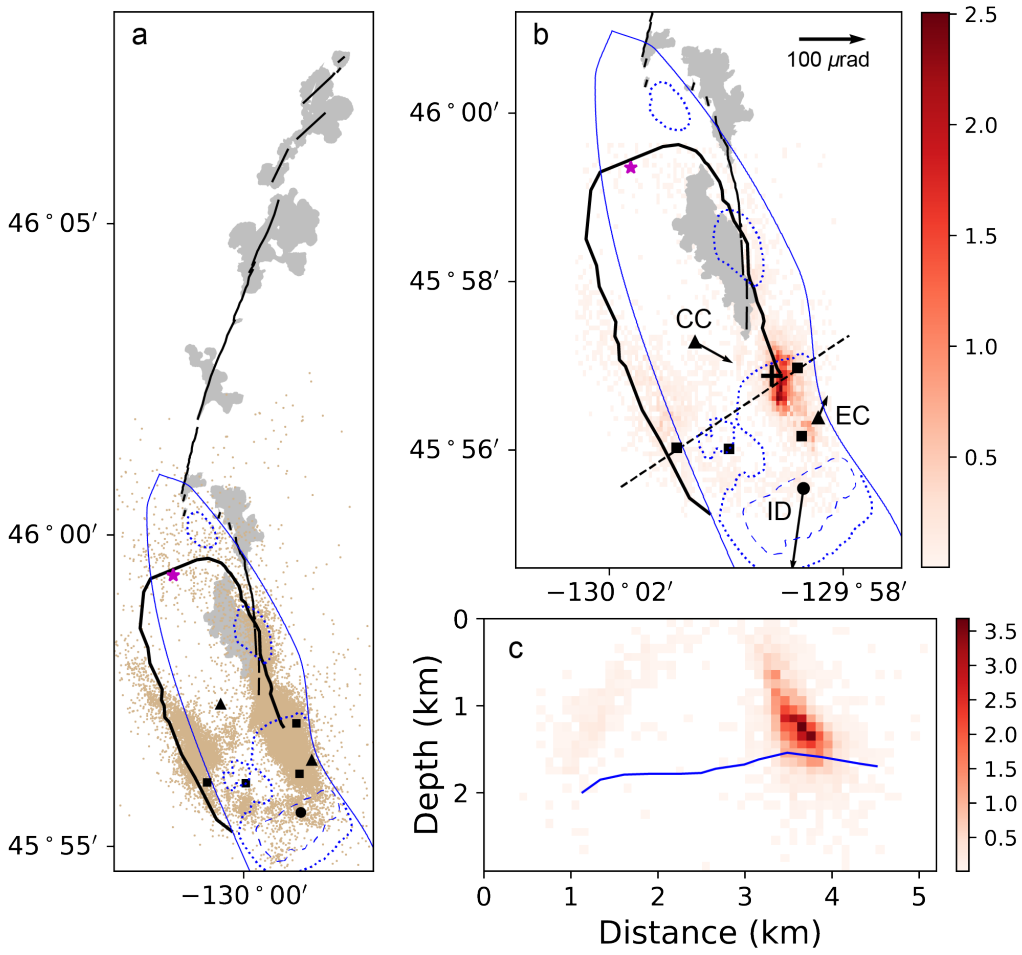

Figure 1: Map of Axial Seamount. a, Short-period (black squares and circle) and broadband (black triangles) seismometers, co-located bottom pressure recorder and tiltmeter stations (black triangles and circle), lava flows for the 2015 eruption [6, 7] (gray-shaded regions), earthquake epicenters [3] (brown dots), caldera rim (thick black line), eruptive fissures [6, 7] (thin black lines/dashes), CASM vent field (magenta star), magma chamber footprint [1] (blue line), and depth contours for the magma chamber at 1.25 km (dotted blue line) and 1.5 km (dashed blue line) depths [1]. b, Zoom in of (a). Tilt magnitudes and directions (black arrows), centroid of the modelled prolate-spheroid deformation source [4] (black cross), and the cross-section shown in (c) (black dashed line). Colorscale shows the difference in daily earthquake rate between the time period before March 9th 2015 and the time period after March 9th 2015 but before April 24th 2015 (see Fig. S1). CC, EC, and ID represent the Central Caldera, Eastern Caldera, and International District stations with co-located tiltmeters, BPRs, and seismometers referred to throughout the text. c, Depth cross-section across the caldera showing the projected earthquake rate change within 0.5 km of the profile. Blue line shows the roof of the shallow magma reservoir [1].

includes two broadband and five short-period seismometers, started streaming time-corrected data in January 2015. We use continuous seismic data recorded by the five short-period seismometers (Fig. 1b) to compute daily CCFs corresponding to all possible station pairs over a two-year period starting in January 2015. We excluded the two broadband seismometers from our analysis to avoid having to correct for instrument response due to uncertainties regarding the appropriate instrument responses.

We use the open-source MSNoise software to measure the relative velocity variation [119]. Using the 8 Hz vertical-component continuous waveforms, we perform one-bit normalization and spectral whitening in 30-minute windows before calculating CCFs for every station pair for time lags of $\pm$120 s. The CCFs were stacked for each day and then the daily CCFs were stacked over 15-day moving windows. A 15-day stack for February 1st contains 15 days of CCFs up to and including February 1st. The reference CCF involves stacking the daily CCFs between 1 June 2015 and 1 January 2017. We measure the delay time ($\mathrm{d}t$) at different lag times (t) between the CCFs and reference CCFs using the moving-window cross-spectrum (MWCS) method[120]. We only keep measurements with an error of less than 0.1s, a coherence of more than 0.65 and a delay time of less than 0.5s. A weighted linear regression was calculated in a 20-s window in the CCF to calculate $\mathrm{d}t/t$ [121]. The minimum lag time of this window was chosen by dividing the interstation distance by a velocity of 1.0 km/s. This allows measurement of the coda waves and excludes the direct arrivals in the CCFs. Finally, we calculate the relative velocity change using $\mathrm{d}v/v = -\mathrm{d}t/t$ assuming a homogeneous relative velocity change [120]. The presented $\mathrm{d}v/v$

represents an average of all the stations pairs. Measurement errors for the relative velocity variation were estimated from the linear regression of dt against t [121]. We use the frequency band between 0.1 and 0.9 Hz, which means the CCFs consist primarily of Rayleigh waves that are sensitive to structures down to ∼2 km below the seafloor [117].

Earthquakes.

∼60,000 earthquakes were located in the three months before the eruption [3]. The earthquakes delineate outward-dipping ring faults (Fig. 1c) that were reactivated during the pre-eruption uplift and syn-eruptive subsidence of the caldera [3, 8]. The epicenters depict a figure eight (Fig. 1a), with the northern ring less well-defined presumably due to the limited footprint of the seismic network [3].

Tilt and Bottom Pressure Records.

We download the tilt and bottom pressure data for stations MJ03D, MJ03E, and MJ03F from the Ocean Observatory Initiative data portal, which correspond to the International District (ID), Eastern Caldera (EC), and Central Caldera (CC) stations respectively (Fig. 1). We use data from the high resolution LILY tiltmeters. We calculate the tilt magnitude and direction from the raw X-tilt and Y-tilt data using the orientations of the tilt axes provided by the internal compasses starting from September 18th 2014. The tilt direction represents the direction of downward tilt.

The bottom pressure recorders (BPRs) record pressure changes exerted by the

overlying water column on the seafloor. If the seafloor rises, this will be recorded as a pressure decrease and vice versa. We then convert pressure to seafloor height using a water density of 1025 kg m^{-3}. Since seafloor pressure changes from oceanographic signals are quite large but can be relatively coherent across the spatial scale of the network [122], we also analyzed the pressure difference between BPR pairs. This then reflects the relative seafloor height between the two sites. The pressure difference analysis only managed to decrease the noise level for the EC and CC station pair.

For the three-segment piecewise linear fits to the time-series data (Figs S2-4), we obtain the slopes and break-points by minimizing the sum of squared residuals. We verified that a three-segment piecewise linear fit is justifiably better than one-segment and two-segment piecewise linear fits based on both the Akaike and Bayesian information criterion.

4.4 Results

The measured relative velocity change (dv/v) from 2015 to 2017 shows an annual signal, with peaks and troughs in the summer and winter, respectively (Fig. S5). Similar observations have been reported on land and are attributed to seasonal changes in ground-water aquifer or atmospheric temperature [123, 124]. Alternatively, such annual signal could be an artifact due to seasonal variation in the ambient seismic noise source [125]. In this paper, we instead focus on the short-term relative velocity changes before the eruption.

We observe an initial increase in dv/v three months before the eruption (Fig. 2a).

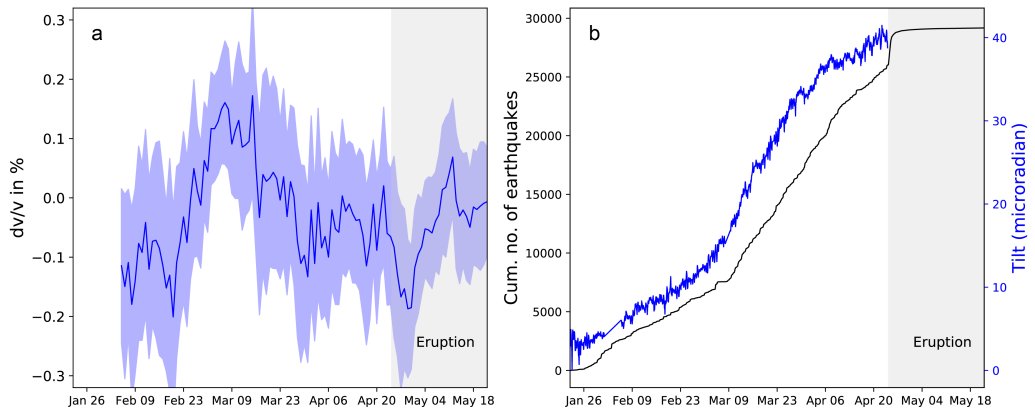

Figure 2: Variation in seismic velocity, seismicity rate, and inflationary tilt rate. a, Relative velocity variations $\mathrm{d}v/v$ before the eruption and the associated measurement errors. Grey bar marks the eruption period [3]. b, Cumulative number of earthquakes with time (black line) and tilt magnitude (blue line) recorded by the Eastern Caldera tiltmeter (see Fig. 1).

However, it is uncertain when this trend started because time-corrected seismic data only began streaming from late January 2015. $\mathrm{d}v/v$ then began to decrease starting early March 2015 (Fig. 2a). Precursory seismic velocity decreases have been observed before eruptions at Piton de la Fournaise volcano [117]. Since no concurrent surface uplifts were observed, the velocity decreases were attributed to crack opening from increases in magma pressurization at a depth that precluded measurable surface deformation [117]. However, at Kilauea volcano, velocity increases were found to correlate with inflation episodes as measured by a tiltmeter and were attributed to crack closing from compression [126]. These observations can be reconciled by considering the volumetric strain due to inflation of a point source: an area directly above the pressure source experiences extension, whereas the surrounding area experiences compression; a deeper pressure source results in a larger area of extension [126]. Therefore, whether a velocity increase or decrease is observed from inflation

of a point source depends on the region of the edifice that is being sampled by the seismic waves relative to the location of the pressure source.

Looking at the cumulative number of earthquakes with time, we find that there was a sharp increase in the earthquake rate from ∼180 day^{-1} to ∼440 day^{-1} in early March 2015 (Figs 2b and S2). The increase in earthquake rate implies an increase in stressing rate on the faults based on the rate/state model [80]. The earthquake rate increase was mostly concentrated in the southeastern part of the caldera between 1 to 1.75 km below the seafloor (Fig. 1b-c). This is above a region of the shallow magma reservoir previously inferred to have the highest melt content based on multichannel seismic surveys [1, 2] as well as the best-fitting pressure source based on modelling net vertical displacements between September 2013 and August 2015, which includes some pre-eruption inflation, the syn-eruptive deflation, and some post-eruption reinflation [4] (Fig. 1b). The earthquake rate then decreased to ∼250 day^{-1} in early April 2015 (Figs 2b and S2), about two weeks before the eruption.

Three of the seismic stations are co-located with tiltmeters (Fig. 1b). The EC station, the station closest to the region where the earthquake rate increase is concentrated, showed changes in inflationary tilt rate that most closely track the variations in seismicity rate (Fig. 2b). Nevertheless, all three tiltmeters recorded an increase in inflationary tilt rate around early March that subsequently decreased approximately three weeks before the eruption (Fig. S3). The inflationary tilt rate of the CC station increased from 0.8 microradians day^{-1} to 1.6 microradians day^{-1} around March 8th before decreasing back to 0.9 microradians day^{-1} around March 25th. The inflationary tilt rate of the EC station increased from 0.3 microradians day^{-1} to 0.8

microradians day^{-1} around March 2nd before decreasing back to 0.3 microradians day^{-1} around March 29th. The inflationary tilt rate of the ID station increased from 1.3 microradians day^{-1} to 1.7 microradians day^{-1} around February 28th before decreasing back to 1.1 microradians day^{-1} around April 4th. While the inflationary tilt rate of all three tiltmeters seems to vary coherently in the three months before the eruption, their tilt directions did not simply point outward radially from a single point source. The tilt directions of the EC and ID stations suggest the tiltmeters are responding to a pressure source located in the southeastern part of the caldera (Fig. 1b). However, the tilt direction of the CC tiltmeter seems to suggest the presence of a pressure source located in the northwestern part of the caldera (Fig. 1b). The tilt directions for both the CC and ID stations were relatively constant in the three months before the eruption (Fig. S3). The tilt direction for the EC station however reflected an $\sim$25°change during the period of increased inflationary tilt rate between early March and April 2015 (Fig. S3c).

All the BPR data seem to reflect relatively constant vertical uplift rates in the months before the eruption (Fig. S6). When we look at the relative seafloor height between the CC and EC stations, we find that it increased with time (Fig. S4), consistent with the vertical uplift rate in the Central Caldera being larger than that in the Eastern Caldera [4, 8] (Fig. S6). However, the rate of increase of the relative seafloor height increased from 35 cm year^{-1} to 59 cm year^{-1} around early March before subsequently decreasing to 35 cm year^{-1} approximately two weeks before the eruption (Fig. S4). This could represent an increase in the vertical uplift rate in the Central Caldera or a decrease in the vertical uplift rate in the Eastern Caldera

between early March and April 2015. However, since the tilt data of both the CC and EC stations suggest an increase in inflationary tilt rate between early March and April 2015, we instead infer that the vertical uplift rates of both the CC and EC stations increased during that time period but with the absolute magnitude of rate increase being larger at the CC station.

Even though the earthquake catalog and the $\mathrm{d}v/v$ measurements only go back to late January 2015, the tilt and BPR data go back to mid-September 2014. We find that in the seven months before the eruption, the inflationary tilt rate at the EC station is the largest between early March and April 2015 (Fig. S7). This also applies to the relative vertical uplift rate between BPR stations CC and EC (Fig. S7). The relatively vertical uplift rate between stations CC and EC closely tracks the inflationary tilt rate at the EC station (Fig. S7). We infer this to reflect that when there is an increase/decrease in vertical uplift rate at the EC station, station CC also experiences the same change but one of larger absolute magnitude.

4.5 Discussions and Conclusions

Our observations suggest that between early March and April 2015, there was a pulse of increased melt influx into a region of the shallow reservoir below the southeastern part of the caldera. The increased inflation rate resulted in a higher stressing rate on the outward-dipping fault above this segment of the reservoir and hence the increased earthquake rate (Figs 1b, 2, and 3). The region above the inflation source undergoes extension and the increased crack opening is manifested as a concurrent decrease

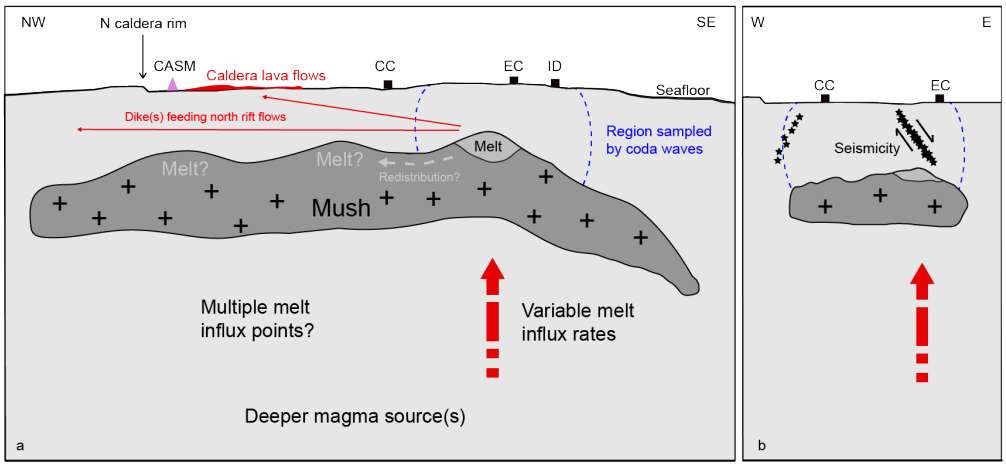

Figure 3: Cartoon illustrating the inferred volcanic processes leading up to the eruption. a, Northwest-Southeast cross-section. Increased rate of melt influx into the southern segment of the shallow reservoir weeks before the eruption resulted in the southern part of the edifice being dominated by extension and hence the decreasing seismic velocity in the edifice. There are possibly multiple melt pockets within the shallow reservoir, either due to the presence of multiple locations of melt influx from depth, or locations where melt ponds after being redistributed from the initial injection point in the southeastern part of the caldera. North rift lava flows might have incorporated magma from these other melt pockets. b, East-West cross-section. Variable rate of melt influx into the eastern region of the shallow reservoir affects the stressing rate on the fault and hence the seismicity rate.

in seismic velocity during this time period (Fig. 2a). The increased rate of melt influx into the southeastern part of the shallow reservoir weeks before the eruption could explain why the 2015 caldera lava flows were the hottest to erupt (highest MgO content) in the last 350 years [115]. It is also consistent with where the dikes initiated during the 2015 eruption sequence [3–5]. This increased rate of melt influx into the shallow reservoir weeks before the eruption is in line with previous suggestions that rifting episodes in Afar and Iceland were triggered by renewed magma influx into the shallow reservoir [31, 40, 127, 128]. However, this is counter to the East Pacific Rise, a non-hotspot-influenced mid-ocean ridge, where the eruption is inferred to be

primarily controlled by the buildup of tectonic stress instead of magma overpressure [73]. Thus Axial Seamount, which sits atop the Cobb hotspot, appears to behave more like a volcano than a typical mid-ocean ridge system [129].

The initial seismic velocity increase three months before the eruption is harder to explain. One potential explanation is that the southern part of the edifice was initially dominated by compression due to an inflating pressure source below the northern part of the caldera (Fig. 3). The presence of a pressure source below the northern part of the caldera is supported by the tilt direction of the CC tiltmeter (Fig. 1b). This is also consistent with the presence of the Canadian American Seamount (CASM) vent field on the northern caldera floor, as high-temperature hydrothermal systems have been suggested to require the presence of an underlying crustal reservoir with ongoing magma recharge to maintain the high heat fluxes [130]. The mapped eruptive fissures north of the caldera also align with the location of the CASM vent field and the northern part of the shallow reservoir and have different strikes compared to the eruptive fissures along the eastern wall of the caldera (Fig. 1a). However, the tilt magnitude and vertical uplift rate of CC and EC seem to co-vary throughout the seven months before the eruption (Fig. S7). It is therefore difficult to understand why the CC tilt direction would primarily reflect the inflation of another pressure source instead of the inflating pressure source below the southeastern part of the caldera. The CC tilt direction also remained relatively constant in the three months before the eruption. If station CC was responding to two pressure sources, one would expect its tilt direction to change if the deformation field changed from being initially dominated by an inflating pressure source below the northern part of the

caldera before early March to being dominated by the inflating pressure source below the southeastern part of the caldera after early March 2015. The lack of seismic and geodetic instrumentation in the northern part of the caldera means that we remain relatively blind to possible active processes beneath this part of the caldera.

Another potential explanation for the initial seismic velocity increase and the CC tilt direction is the complexity of the shallow magma reservoir topography. Active seismic reflection imaging shows that the top of the shallow magma reservoir varies significantly with four different shallow points (Fig. 1) [1, 2]. Therefore, while there is strong evidence for a pressure source in the southeastern part of the caldera, the melt is unlikely to accumulate in a simple point source. Instead, the different shallow points of the magma reservoir might reflect different locations of melt influx from depth, or locations where melt ponds after being redistributed from the initial injection point in the southeastern part of the caldera (Fig. 3). The presence of different melt pockets is consistent with the caldera lava flows having a more primitive composition (higher MgO) than the north rift flows [6, 115] which suggests an eruption that was fed by different regions of a zoned shallow magma reservoir. Such complexities would explain our difficulty in reconciling all the observations with simplified pressure source geometries that are stationary in time. Finally, we cannot rule out the anomalous CC tilt direction being a topographic effect, as the existence of sharp bathymetry such as the caldera rim can cause tilt to rotate up to 180°relative to what would be expected without bathymetry [131].

Our results suggest that the shallow magma reservoir can be relatively complex with variable melt influx rate in time. Such complexities can only be resolved with

the integration of multiple datasets. Future improvements include measurements that cover the entire footprint of the magma reservoir, in particular the northern caldera region, coupled with modeling that goes beyond simple reservoir geometries and takes into account the effect of bathymetry on surface deformation. Finally, our observation of increased magma influx rate into the shallow reservoir weeks before the eruption suggests that analysis of real-time geophysical data might aid eruption forecasting and facilitate installation of additional *in situ* instrumentation before future eruptisons, an important step in furthering our understanding of this fundamental process of crustal formation.

4.6 Acknowledgements

This work was supported by NSF under grant OCE-1536320. The earthquake catalog used in this study is from [3] and is archived in the Interdisciplinary Earth Data Alliance Marine Geoscience Data System (DOI: 10.1594/IEDA/323843). The seismic data used in this study were downloaded from the Incorporated Research Institutions for Seismology Data Management System (IRIS DMC).

4.7 Supplementary Figures

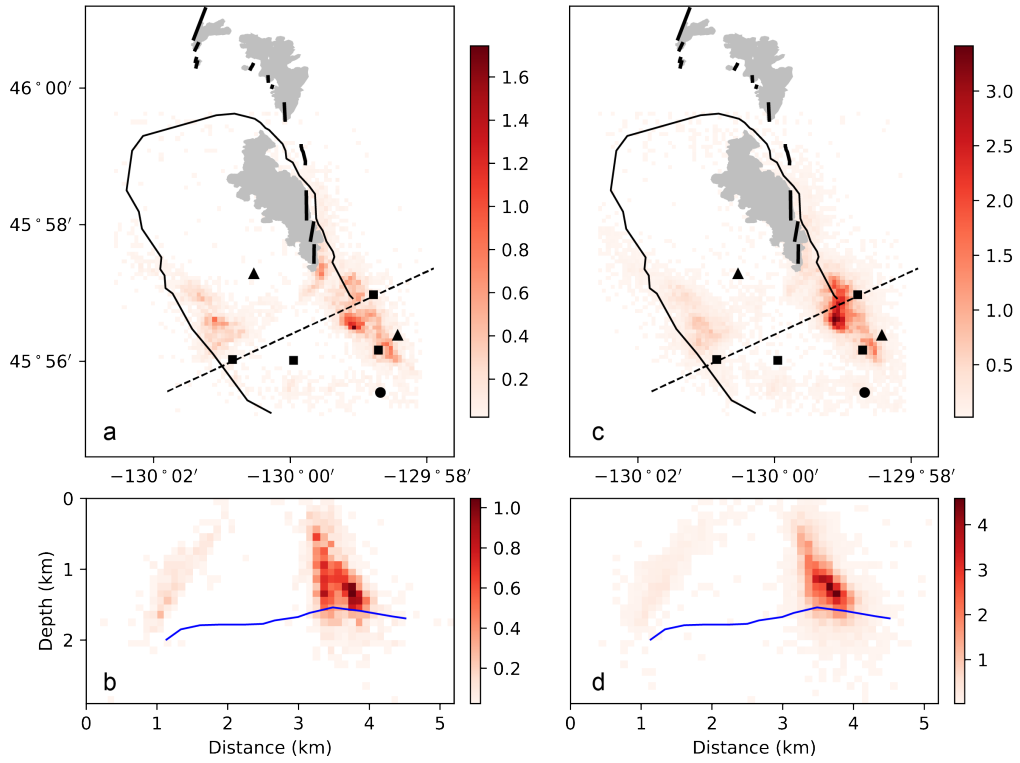

Figure S1: Daily earthquake rate. a-b, Between Jan 22nd and March 9th 2015. c-d, Between March 9th 2015 and April 23rd 2015. a,c, Map view with black dashed line depicting cross-sections shown in (b) and (d). Gray-shaded regions are the lava flows for the 2015 eruption [6, 7], black line delineates the caldera rim, thick black ticks delineate the eruption fissures [6, 7]. b,d, Depth cross-section across the caldera showing the projected daily earthquake rate within 0.5 km of the profile. Blue line depicts the roof of the shallow magma reservoir [1].

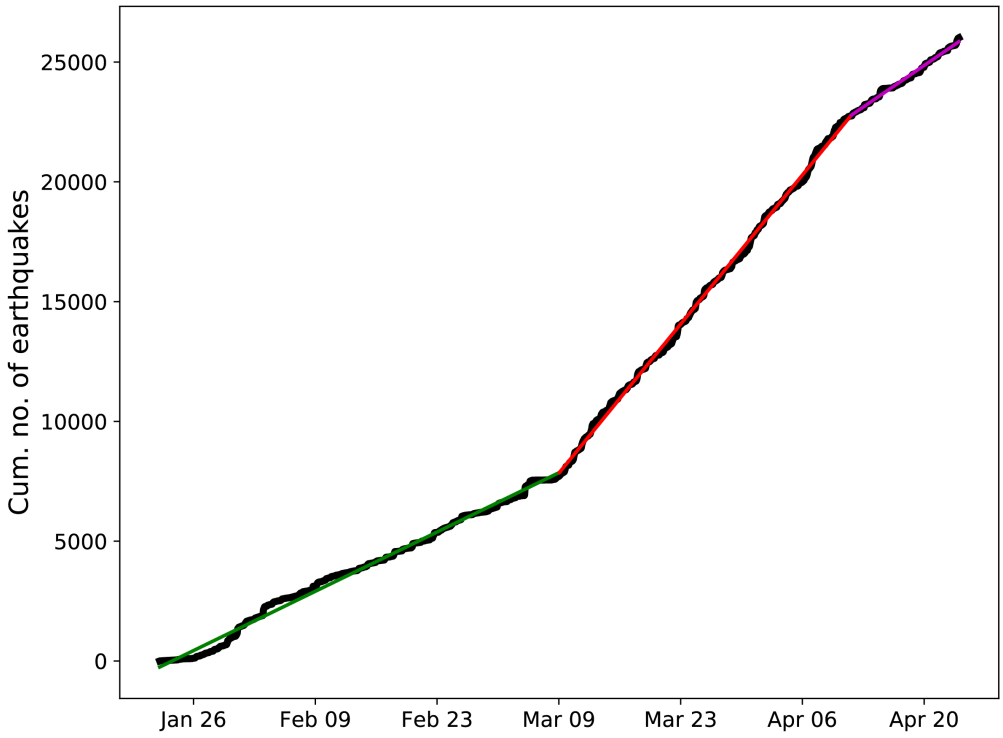

Figure S2: Cumulative number of earthquakes with time (black line). Green, red, and magenta lines show linear fits to the three time periods with different seismicity rates. The start times and seismicity rates of the three segments are Jan 22nd, March 9th, April 11th and $\sim$180 day^{-1}, $\sim$440 day^{-1}, and $\sim$250 day^{-1}.

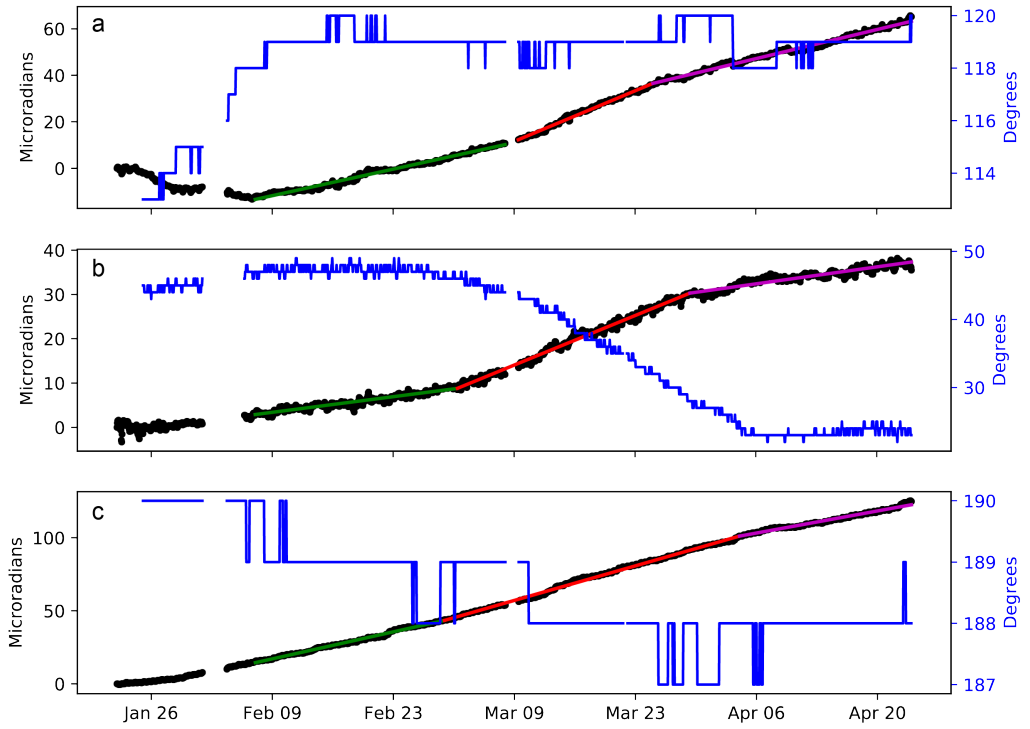

Figure S3: Tilt magnitude (black) and direction (blue) from Jan 22nd to April 23rd 2015. Green, red, and magenta lines show linear fits to the three time periods with different tilt increase rates. a, Central caldera. The start times and tilt increase rates of the three segments are Feb 7th, March 8th, March 25th and 0.8 microradians/day, 1.6 microradians/day, 0.9 microradians/day. b, Eastern caldera. The start times and tilt increase rates of the three segments are Feb 7th, March 2nd, March 29th and 0.3 microradians/day, 0.8 microradians/day, 0.3 microradians/day. c, International district. The start times and tilt increase rates of the three segments are Feb 7th, Feb 28th, April 4th and 1.3 microradians/day, 1.7 microradians/day, 1.1 microradians/day. See station locations in Fig. 1.

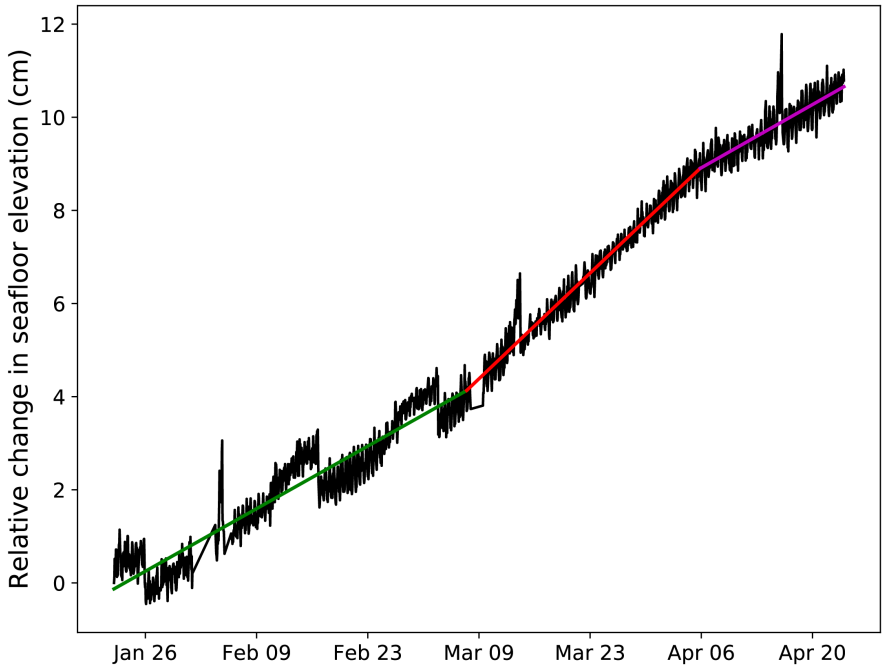

Figure S4: Relative change in seafloor elevation with time recorded between the Central Caldera and Eastern Caldera bottom pressure recorders from Jan 22nd 2015 to April 23rd 2015. The upward trend shows that CC is uplifting at a higher rate than EC. Green, red, and magenta lines show linear fits to the three time periods with different relative uplift rates. The start times and relative uplift rates of the three segments are Jan 22nd, March 7th, April 5th and 35 cm/yr, 59 cm/yr, 35 cm/yr.

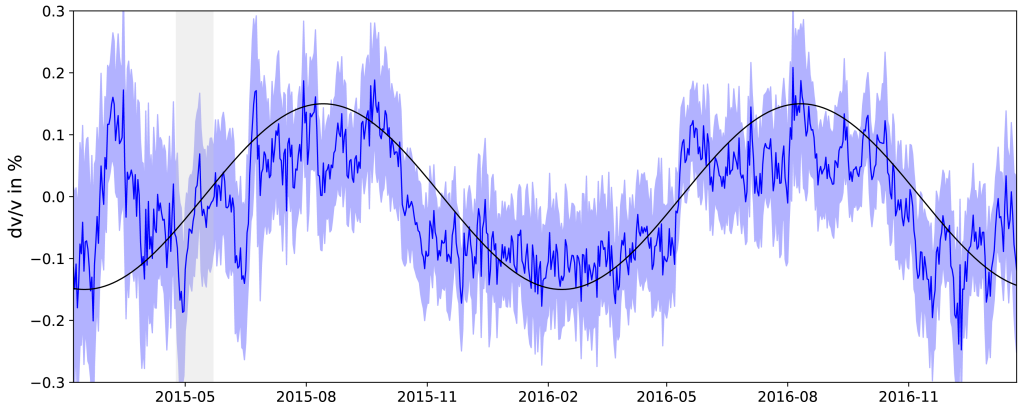

Figure S5: Relative velocity variations $\mathrm{d}v/v$ (blue line) from 2015 to 2017 and the associated measurement errors (blue shading). Grey bar marks the eruption period [3]. Black line shows a sinusoid with a one-year period.

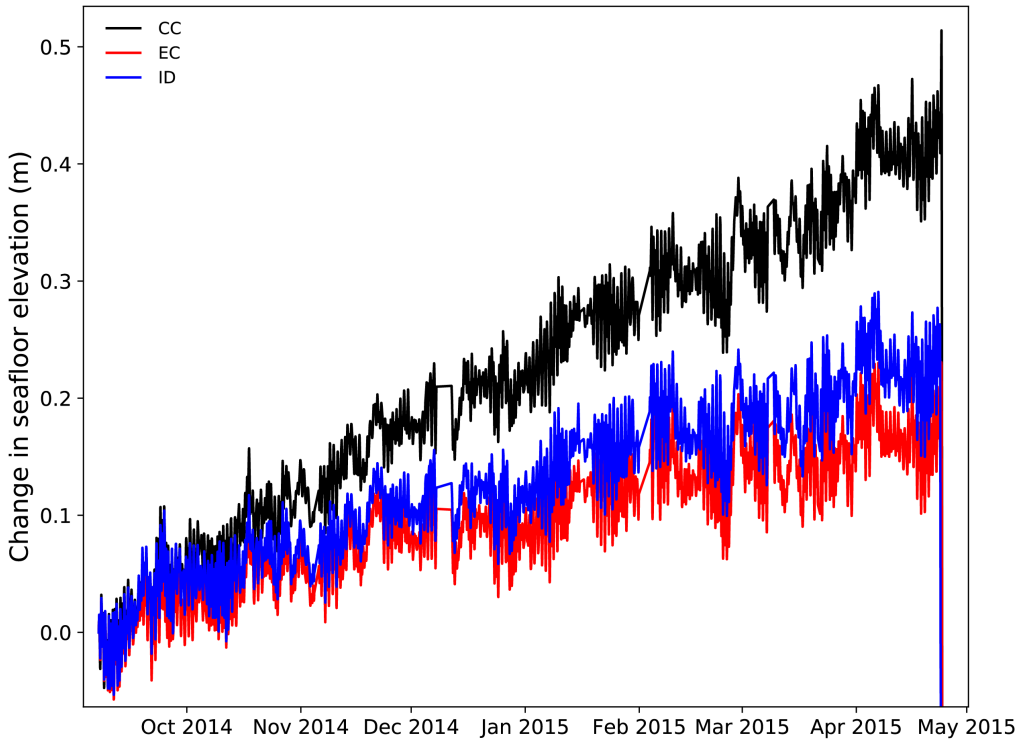

Figure S6: Change in seafloor elevation with time as recorded by the bottom pressure recorders with a 5-hour low-pass filter.

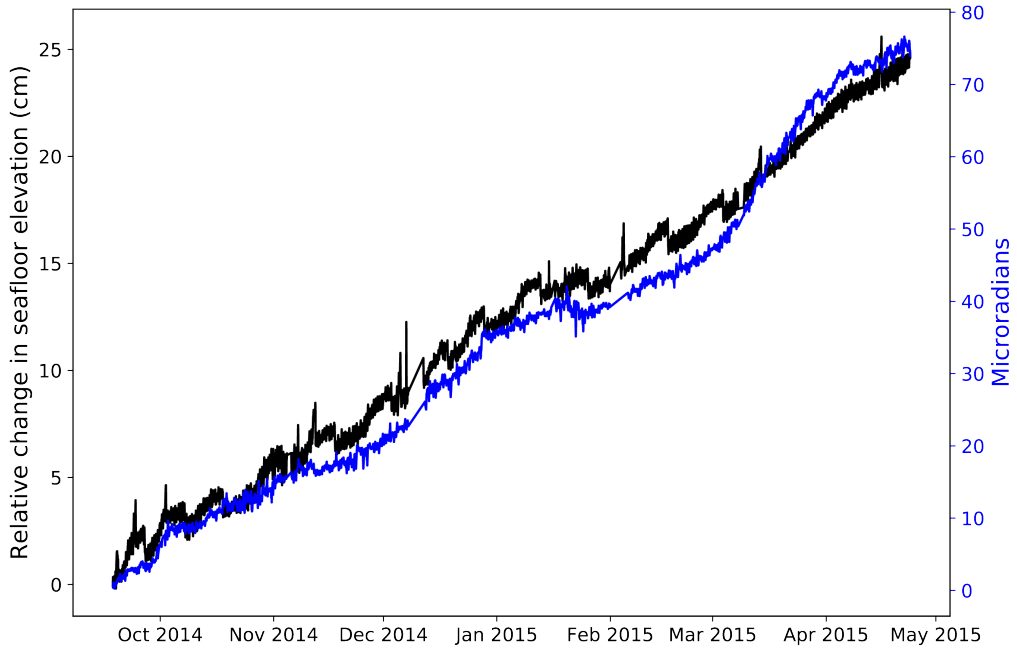

Figure S7: EC tilt magnitude (blue line) and relative change in seafloor elevation between CC and EC (black line) from September 18th 2014 to April 23rd 2015.

Conclusion

The thesis can be summarized as having addressed the following questions:

- What volcanic and tectonic processes controlled the evolution of the 2006 East Pacific Rise eruption?
- How did tidal triggering of microearthquakes at the East Pacific Rise change through an eruption cycle?
- Is earthquake size-frequency distribution stress-dependent?
- How did the magmatic system evolve in the months leading up to the 2015 Axial Seamount eruption?

The main results of the thesis are as follow:

- The 2006 East Pacific Rise eruption lasted two weeks and involved melt being erupted from multiple melt lenses at variable erupted volumes and magma ascent rates, suggesting that the eruption was mainly controlled by the buildup of tectonic stress to a critical level rather than magma overpressure.
- Tidal triggering of earthquakes was strong and relatively constant in the two years before the eruption but disappeared/weakened immediately after the eruption, suggesting that tidal triggering variation may not be useful for fore-

casting mid-ocean ridge eruptions over a 2+ years timescale but might be useful over a longer timescale.

- Above a threshold stress amplitude, earthquake b value is inversely correlated with stress.
- The 2015 Axial Seamount eruption was preceded by variable rates of melt influx into the shallow reservoir as inferred from the variations in seismicity and deformation rates as well as changes in seismic velocity in the caldera edifice.

Bibliography

1. Arnulf, A. *et al.* Anatomy of an active submarine volcano. *Geology* **42,** 655–658 (2014).

2. Arnulf, A. F., Harding, A. J., Kent, G. M. & Wilcock, W. S. D. Structure, Seismicity, and Accretionary Processes at the Hot Spot-Influenced Axial Seamount on the Juan de Fuca Ridge. *Journal of Geophysical Research: Solid Earth* **123,** 4618–4646 (2018).

3. Wilcock, W. S. *et al.* Seismic constraints on caldera dynamics from the 2015 Axial Seamount eruption. *Science* **354,** 1395–1399 (2016).

4. Nooner, S. L. & Chadwick, W. W. Inflation-predictable behavior and co-eruption deformation at Axial Seamount. *Science* **354,** 1399–1403 (2016).

5. Wilcock, W. S. *et al.* The recent volcanic history of Axial Seamount: Geophysical insights into past eruption dynamics with an eye toward enhanced observations of future eruptions. *Oceanography* **31,** 114–123 (2018).

6. Chadwick, W. *et al.* Voluminous eruption from a zoned magma body after an increase in supply rate at Axial Seamount. *Geophysical Research Letters* **43,** 12–063 (2016).

7. Clague, D. *et al.* High-Resolution AUV Mapping and Targeted ROV Observations of Three Historical Lava Flows at Axial Seamount. *Oceanography* **30.** doi:10.5670/oceanog.2017.426. https://doi.org/10.5670/oceanog.2017.426 (2017).

8. Levy, S. *et al.* Mechanics of fault reactivation before, during, and after the 2015 eruption of Axial Seamount. *Geology* **46,** 447–450 (2018).

9. Scholz, C. The frequency-magnitude relation of microfracturing in rock and its relation to earthquakes. *Bulletin of the seismological society of America* **58,** 399–415 (1968).

10. Schorlemmer, D., Wiemer, S. & Wyss, M. Variations in earthquake-size distribution across different stress regimes. *Nature* **437,** 539–542 (2005).

11. Spada, M., Tormann, T., Wiemer, S. & Enescu, B. Generic dependence of the frequency-size distribution of earthquakes on depth and its relation to the strength profile of the crust. *Geophysical Research Letters* **40,** 709–714 (2013).

12. Nishikawa, T. & Ide, S. Earthquake size distribution in subduction zones linked to slab buoyancy. *Nature Geoscience* **7,** 904–908 (2014).

13. Mori, J. & Abercrombie, R. E. Depth dependence of earthquake frequency-magnitude distributions in California: Implications for rupture initiation. *Journal of Geophysical Research: Solid Earth* **102,** 15081–15090 (1997).

14. Goebel, T. H., Kwiatek, G., Becker, T. W., Brodsky, E. E. & Dresen, G. What allows seismic events to grow big?: Insights from b-value and fault roughness analysis in laboratory stick-slip experiments. *Geology* **45,** 815–818 (2017).

15. Tolstoy, M., Vernon, F. L., Orcutt, J. A. & Wyatt, F. K. Breathing of the seafloor: Tidal correlations of seismicity at Axial volcano. *Geology* **30,** 503–506 (2002).

16. Tolstoy, M *et al.* A sea-floor spreading event captured by seismometers. *Science* **314,** 1920–1922 (2006).

17. Soule, S. A., Fornari, D. J., Perfit, M. R. & Rubin, K. H. New insights into mid-ocean ridge volcanic processes from the 2005–2006 eruption of the East Pacific Rise, 9 46 N–9 56 N. *Geology* **35,** 1079–1082 (2007).

18. Xu, M. *et al.* Variations in axial magma lens properties along the East Pacific Rise (9° 30 N–10° 00 N) from swath 3-D seismic imaging and 1-D waveform inversion. *Journal of Geophysical Research: Solid Earth* **119,** 2721–2744 (2014).

19. Marjanović, M. *et al.* A multi-sill magma plumbing system beneath the axis of the East Pacific Rise. *Nature Geoscience* **7,** 825–829 (2014).

20. Carbotte, S. M. *et al.* Fine-scale segmentation of the crustal magma reservoir beneath the East Pacific Rise. *Nature Geoscience* **6,** 866 (2013).

21. Rubin, K. H. *et al.* Volcanic eruptions in the deep sea. *Oceanography* **25,** 142–157 (2012).

22. Dziak, R. P. *et al.* January 2006 seafloor-spreading event at 9 50 N, East Pacific Rise: Ridge dike intrusion and transform fault interactions from regional hydroacoustic data. *Geochemistry, Geophysics, Geosystems* **10** (2009).

23. Tolstoy, M., Waldhauser, F., Bohnenstiehl, D. R., Weekly, R. T. & Kim, W.-Y. Seismic identification of along-axis hydrothermal flow on the East Pacific Rise. *Nature* **451,** 181–184 (2008).

24. Stroup, D. F., Bohnenstiehl, D. R., Tolstoy, M., Waldhauser, F. & Weekly, R. T. Pulse of the seafloor: Tidal triggering of microearthquakes at 9°50′N East Pacific Rise. *Geophysical Research Letters* **34.** doi:10.1029/2007gl030088. https://doi.org/10.1029/2007gl030088 (2007).

25. Bhatnagar, T., Tolstoy, M. & Waldhauser, F. Influence of fortnightly tides on earthquake triggering at the East Pacific Rise at 9°50′N. *Journal of Geophysical Research: Solid Earth* **121,** 1262–1279 (2016).

26. Stroup, D. F. *et al.* Systematic along-axis tidal triggering of microearthquakes observed at 9°50′N East Pacific Rise. *Geophysical Research Letters* **36.** doi:10.1029/2009gl039493. https://doi.org/10.1029/2009gl039493 (2009).

27. Crone, T. J., Tolstoy, M. & Stroup, D. F. Permeability structure of young ocean crust from poroelastically triggered earthquakes. *Geophysical Research Letters* **38.** doi:10.1029/2011gl046820. https://doi.org/10.1029/2011gl046820 (2011).

28. Tanaka, S., Ohtake, M. & Sato, H. Spatio-temporal variation of the tidal triggering effect on earthquake occurrence associated with the 1982 South Tonga earthquake of Mw 7.5. *Geophysical Research Letters* **29.** doi:10.1029/2002gl015386. https://doi.org/10.1029/2002gl015386 (2002).

29. Tanaka, S. Tidal triggering of earthquakes precursory to the recent Sumatra megathrust earthquakes of 26 December 2004 (Mw9.0), 28 March 2005 (Mw8.6), and 12 September 2007 (Mw8.5). *Geophysical Research Letters* **37.** doi:10.1029/2009gl041581. https://doi.org/10.1029/2009gl041581 (2010).

30. Tanaka, S. Tidal triggering of earthquakes prior to the 2011 Tohoku-Oki earthquake (Mw9.1). *Geophysical Research Letters* **39.** doi:10.1029/2012gl051179. https://doi.org/10.1029/2012gl051179 (2012).

31. Wright, T. J. *et al.* Geophysical constraints on the dynamics of spreading centres from rifting episodes on land. *Nature Geoscience* **5,** 242 (2012).

32. Ebinger, C. J. & Sleep, N. Cenozoic magmatism throughout east Africa resulting from impact of a single plume. *Nature* **395,** 788 (1998).

33. Wolfe, C. J., Bjarnason, I. T., VanDecar, J. C. & Solomon, S. C. Seismic structure of the Iceland mantle plume. *Nature* **385,** 245 (1997).

34. Goss, A. R. *et al.* Geochemistry of lavas from the 2005–2006 eruption at the East Pacific Rise, 9 46 N–9 56 N: Implications for ridge crest plumbing and decadal changes in magma chamber compositions. *Geochemistry, Geophysics, Geosystems* **11** (2010).

35. Fundis, A. T., Soule, S. A., Fornari, D. J. & Perfit, M. R. Paving the seafloor: Volcanic emplacement processes during the 2005-2006 eruptions at the fast spreading East Pacific Rise, 9°50′N. *Geochemistry, Geophysics, Geosystems* **11.** doi:10.1029/2010gc003058. https://doi.org/10.1029/2010gc003058 (2010).

36. Tolstoy, M. Mid-ocean ridge eruptions as a climate valve. *Geophysical Research Letters* **42,** 1346–1351 (2015).

37. Dziak, R. *et al.* Rapid dike emplacement leads to eruptions and hydrothermal plume release during seafloor spreading events. *Geology* **35,** 579–582 (2007).

38. Abdallah, A. *et al.* Relevance of Afar seismicity and volcanism to the mechanics of accreting plate boundaries. *Nature* **282,** 17 (1979).

39. Einarsson, P. & Brandsdóttir, B. *Seismological evidence for lateral magma intrusion during the July 1978 deflation of the Krafla volcano in NE-Iceland* tech. rep. (University of Iceland, Reykjavik, IS, 1978).

40. Ayele, A. *et al.* September 2005 mega-dike emplacement in the Manda-Harraro nascent oceanic rift (Afar depression). *Geophysical Research Letters* **36** (2009).

41. Sigmundsson, F. *et al.* Segmented lateral dyke growth in a rifting event at Bárðarbunga volcanic system, Iceland. *Nature* **517,** 191 (2015).

42. Haymon, R. *et al.* Volcanic eruption of the mid-ocean ridge along the East Pacific Rise crest at 9 45–52 N: Direct submersible observations of seafloor phenomena associated with an eruption event in April, 1991. *Earth and Planetary Science Letters* **119,** 85–101 (1993).

43. Rubin, K., Macdougall, J. & Perfit, M. 210Po–210Pb dating of recent volcanic eruptions on the sea floor. *Nature* **368,** 841 (1994).

44. White, S. M., Haymon, R. M. & Carbotte, S. A new view of ridge segmentation and near-axis volcanism at the East Pacific Rise, 8°-12°N, from EM300 multibeam bathymetry. *Geochemistry, Geophysics, Geosystems* **7.** doi:10.1029/2006gc001407. https://doi.org/10.1029/2006gc001407 (2006).

45. Munk, W., Worcester, P. & Wunsch, C. in, 30–114 (1995).

46. Gibbons, S. J. & Ringdal, F. The detection of low magnitude seismic events using array-based waveform correlation. *Geophysical Journal International* **165,** 149–166 (2006).

47. Lomax, A., Michelini, A. & Curtis, A. in *Encyclopedia of Complexity and Systems Science* (ed Meyers, R. A.) 1–33 (Springer New York, 2014). doi:10.1007/978-3-642-27737-5_150-2. http://dx.doi.org/10.1007/978-3-642-27737-5_150-2.

48. Waldhauser, F. A Double-Difference Earthquake Location Algorithm: Method and Application to the Northern Hayward Fault, California. *Bulletin of the Seismological Society of America* **90,** 1353–1368 (2000).

49. Waldhauser, F. & Tolstoy, M. Seismogenic structure and processes associated with magma inflation and hydrothermal circulation beneath the East Pacific Rise at 9°50′N. *Geochemistry, Geophysics, Geosystems* **12.** doi:10.1029/2011gc003568. https://doi.org/10.1029/2011gc003568 (2011).

50. Bohnenstiehl, D. R., Waldhauser, F. & Tolstoy, M. Frequency-magnitude distribution of microearthquakes beneath the 9°50′N region of the East Pacific Rise, October 2003 through April 2004. *Geochemistry, Geophysics, Geosystems* **9.** doi:10.1029/2008gc002128. https://doi.org/10.1029/2008gc002128 (2008).

51. Gottschämmer, E & Surono, I. Locating tremor and shock sources recorded at Bromo Volcano. *Journal of Volcanology and Geothermal Research* **101,** 199–209 (2000).

52. Schlindwein, V., Müller, C. & Jokat, W. Seismoacoustic evidence for volcanic activity on the ultraslow-spreading Gakkel Ridge, Arctic Ocean. *Geophysical Research Letters* **32** (2005).

53. Vergniolle, S, Brandeis, G & Mareschal, J.-C. Strombolian explosions: 2. Eruption dynamics determined from acoustic measurements. *Journal of Geophysical Research: Solid Earth* **101,** 20449–20466 (1996).

54. Perfit, M. R. *et al.* Interaction of sea water and lava during submarine eruptions at mid-ocean ridges. *Nature* **426,** 62 (2003).

55. Gregg, T. K., Fornari, D. J., Perfit, M. R., Haymon, R. M. & Fink, J. H. Rapid emplacement of a mid-ocean ridge lava flow on the East Pacific Rise at 9 46 –51 N. *Earth and Planetary Science Letters* **144** (1996).

56. Buck, W. *On the frequency of dike intrusion episodes at spreading centers* in *AGU Fall Meeting Abstracts* (2006).

57. Chouet, B. A. Long-period volcano seismicity: its source and use in eruption forecasting. *Nature* **380,** 309–316 (1996).

58. Canales, J. P. *et al.* Network of off-axis melt bodies at the East Pacific Rise. *Nature Geoscience* **5,** 279–283 (2012).

59. Bohnenstiehl, D. R. & Carbotte, S. M. Faulting patterns near 19°30′Son the East Pacific Rise: Fault formation and growth at a superfast spreading center. *Geochemistry, Geophysics, Geosystems* **2.** doi:10.1029/2001gc000156. https://doi.org/10.1029/2001gc000156 (2001).

60. Buck, W. R., Einarsson, P. & Brandsdóttir, B. Tectonic stress and magma chamber size as controls on dike propagation: Constraints from the 1975-1984 Krafla rifting episode. *Journal of Geophysical Research: Solid Earth* **111.** doi:10.1029/2005jb003879. https://doi.org/10.1029/2005jb003879 (2006).

61. Fornari, D. *et al.* in *Mid-Ocean Ridges* 187–217 (American Geophysical Union, 2013). doi:10.1029/148gm08. https://doi.org/10.1029/148gm08.

62. Saal, A. E., Hauri, E. H., Langmuir, C. H. & Perfit, M. R. Vapour undersaturation in primitive mid-ocean-ridge basalt and the volatile content of Earth's upper mantle. *Nature* **419,** 451–455 (2002).

63. Shinohara, H. Excess degassing from volcanoes and its role on eruptive and intrusive activity. *Reviews of Geophysics* **46.** doi:10.1029/2007rg000244. https://doi.org/10.1029/2007rg000244 (2008).

64. Soule, S. *et al.* CO2 variability in mid-ocean ridge basalts from syn-emplacement degassing: Constraints on eruption dynamics. *Earth and Planetary Science Letters* **327-328,** 39–49 (2012).

65. Emter, D. in *Tidal phenomena* 293–309 (Springer, 1997).

66. Wilcock, W. S. D. Tidal triggering of microearthquakes on the Juan de Fuca Ridge. *Geophysical Research Letters* **28,** 3999–4002 (2001).

67. Wilcock, W. S. D. Tidal triggering of earthquakes in the Northeast Pacific Ocean. *Geophysical Journal International* **179,** 1055–1070 (2009).

68. Tanaka, S., Ohtake, M. & Sato, H. Evidence for tidal triggering of earthquakes as revealed from statistical analysis of global data. *Journal of Geophysical Research: Solid Earth* **107.** doi:10.1029/2001jb001577. https://doi.org/10.1029/2001jb001577 (2002).

69. Cochran, E. S., Vidale, J. E. & Tanaka, S. Earth tides can trigger shallow thrust fault earthquakes. *Science* **306,** 1164–1166 (2004).

70. McNutt, S. R. & Beavan, R. J. Patterns of earthquakes and the effect of solid earth and ocean load tides at Mount St. Helens prior to the May 18, 1980, eruption. *Journal of Geophysical Research: Solid Earth* **89,** 3075–3086 (1984).

71. Rydelek, P. A., Davis, P. M. & Koyanagi, R. Y. Tidal triggering of earthquake swarms at Kilauea Volcano, Hawaii. *Journal of Geophysical Research: Solid Earth* **93,** 4401–4411 (1988).

72. Tanaka, S., Sato, H., Matsumura, S. & Ohtake, M. Tidal triggering of earthquakes in the subducting Philippine Sea plate beneath the locked zone of the plate interface in the Tokai region, Japan. *Tectonophysics* **417,** 69–80 (2006).

73. Tan, Y. J., Tolstoy, M., Waldhauser, F. & Wilcock, W. S. D. Dynamics of a seafloor-spreading episode at the East Pacific Rise. *Nature* **540,** 261–265 (2016).

74. Agnew, D. C. in *Treatise on Geophysics and Geodesy* (ed Herring, T. A.) 163–195 (Elsevier, New York, 2007).

75. Sohn, R. A., Hildebrand, J. A. & Webb, S. C. A microearthquake survey of the high-temperature vent fields on the volcanically active East Pacific Rise (9°50′N). *Journal of Geophysical Research: Solid Earth* **104,** 25367–25377 (1999).

76. Agnew, D. C. NLOADF: A program for computing ocean-tide loading. *Journal of Geophysical Research: Solid Earth* **102,** 5109–5110 (1997).

77. Savcenko, R. & Bosch, W. EOT11a-empirical ocean tide model from multi-mission satellite altimetry. *DGFI Report No. 89* (2012).

78. Alterman, Z, Jarosch, H & Pekeris, C. Propagation of Rayleigh waves in the earth. *Geophysical Journal International* **4,** 219–241 (1961).

79. Schuster, A. On lunar and solar periodicities of earthquakes. *Proceedings of the Royal Society of London* **61,** 455–465 (1897).

80. Dieterich, J. A constitutive law for rate of earthquake production and its application to earthquake clustering. *Journal of Geophysical Research: Solid Earth* **99,** 2601–2618 (1994).

81. Beeler, N. M. Why earthquakes correlate weakly with the solid Earth tides: Effects of periodic stress on the rate and probability of earthquake occurrence.

Journal of Geophysical Research **108.** doi:10.1029/2001jb001518. https://doi.org/10.1029/2001jb001518 (2003).

82. Dieterich, J. H. Nucleation and triggering of earthquake slip: effect of periodic stresses. *Tectonophysics* **144,** 127–139 (1987).

83. Dziak, R. P. & Fox, C. G. Long-term seismicity and ground deformation at Axial Volcano, Juan de Fuca Ridge. *Geophysical research letters* **26,** 3641–3644 (1999).

84. Gutenberg, B. & Richter, C. F. Frequency of earthquakes in California. *Bulletin of the Seismological Society of America* **34,** 185–188 (1944).

85. Amitrano, D. Brittle-ductile transition and associated seismicity: Experimental and numerical studies and relationship with thebvalue. *Journal of Geophysical Research: Solid Earth* **108.** doi:10.1029/2001jb000680. https://doi.org/10.1029/2001jb000680 (2003).

86. Goebel, T. H. W., Schorlemmer, D., Becker, T. W., Dresen, G. & Sammis, C. G. Acoustic emissions document stress changes over many seismic cycles in stick-slip experiments. *Geophysical Research Letters* **40,** 2049–2054 (2013).

87. Scholz, C. H. On the stress dependence of the earthquake b value. *Geophysical Research Letters* **42,** 1399–1402 (2015).

88. Stumpf, M. P. H. & Porter, M. A. Critical Truths About Power Laws. *Science* **335,** 665–666 (2012).

89. Schorlemmer, D. & Wiemer, S. Microseismicity data forecast rupture area. *Nature* **434,** 1086–1086 (2005).

90. Nanjo, K. Z., Hirata, N., Obara, K. & Kasahara, K. Decade-scale decrease inbvalue prior to theM9-class 2011 Tohoku and 2004 Sumatra quakes. *Geophysical Research Letters* **39.** doi:10.1029/2012gl052997. https://doi.org/10.1029/2012gl052997 (2012).

91. Gulia, L., Tormann, T., Wiemer, S., Herrmann, M. & Seif, S. Short-term probabilistic earthquake risk assessment considering time-dependent b values. *Geophysical Research Letters* **43,** 1100–1108 (2016).

92. Kato, A. *et al.* Preparatory and precursory processes leading up to the 2014 phreatic eruption of Mount Ontake, Japan. *Earth, Planets and Space* **67.** doi:10.1186/s40623-015-0288-x. https://doi.org/10.1186/s40623-015-0288-x (2015).

93. Vidale, J. E., Agnew, D. C., Johnston, M. J. S. & Oppenheimer, D. H. Absence of earthquake correlation with Earth tides: An indication of high preseismic fault stress rate. *Journal of Geophysical Research: Solid Earth* **103,** 24567–24572 (1998).

94. Wang, W. & Shearer, P. M. No clear evidence for localized tidal periodicities in earthquakes in the central Japan region. *Journal of Geophysical Research: Solid Earth* **120,** 6317–6328 (2015).

95. Tan, Y. J., Tolstoy, M., Waldhauser, F. & Bohnenstiehl, D. R. Tidal triggering of microearthquakes over an eruption cycle at 9° 50'N East Pacific Rise. *Geophysical Research Letters* **45,** 1825–1831 (2018).

96. Scholz, C. H., Tan, Y. J. & Albino, F. The Mechanism of Tidal Triggering of Earthquakes at Mid-Ocean Ridges. *arXiv preprint arXiv:1812.00639* (2018).

97. Tréhu, A. M. & Solomon, S. C. Earthquakes in the Orozco Transform Zone: Seismicity, source mechanisms, and tectonics. *Journal of Geophysical Research* **88,** 8203 (1983).

98. Aki, K. Maximum likelihood estimate of b in the formula log N= a-bM and its confidence limits. *Bull. Earthq. Res. Inst., Tokyo Univ.* **43,** 237–239 (1965).

99. Utsu, T. A Statistical Significance Test of the Difference in b-value between Two Earthquake Groups. *Journal of Physics of the Earth* **14,** 37–40 (1966).

100. Shi, Y. & Bolt, B. A. The standard error of the magnitude-frequency b value. *Bulletin of the Seismological Society of America* **72,** 1677–1687 (1982).

101. Utsu, T. Introduction to seismicity. *Mathematical Seismology* **7,** 139–157 (1992).

102. Kagan, Y. Y. Seismic moment-frequency relation for shallow earthquakes: Regional comparison. *Journal of Geophysical Research: Solid Earth* **102,** 2835–2852 (1997).

103. Wiemer, S. & Katsumata, K. Spatial variability of seismicity parameters in aftershock zones. *Journal of Geophysical Research: Solid Earth* **104,** 13135–13151 (1999).

104. Mignan, A. & Woessner, J. Estimating the magnitude of completeness for earthquake catalogs. doi:10.5078/corssa-00180805. http://www.corssa.org/export/sites/corssa/.galleries/articles-pdf/Mignan-Woessner-2012-CORSSA-Magnitude-of-completeness.pdf (2012).

105. Wiemer, S. Minimum Magnitude of Completeness in Earthquake Catalogs: Examples from Alaska, the Western United States, and Japan. *Bulletin of the Seismological Society of America* **90,** 859–869 (2000).

106. Woessner, J. Assessing the Quality of Earthquake Catalogues: Estimating the Magnitude of Completeness and Its Uncertainty. *Bulletin of the Seismological Society of America* **95,** 684–698 (2005).

107. Cao, A. & Gao, S. S. Temporal variation of seismicb-values beneath northeastern Japan island arc. *Geophysical Research Letters* **29.** doi:10.1029/2001gl013775. https://doi.org/10.1029/2001gl013775 (2002).

108. Egbert, G. D. & Erofeeva, S. Y. Efficient inverse modeling of barotropic ocean tides. *Journal of Atmospheric and Oceanic Technology* **19,** 183–204 (2002).

109. Iwata, T. & Young, R. P. Tidal Stress/Strain and the b-values of Acoustic Emissions at the Underground Research Laboratory, Canada. *Pure and Applied Geophysics* **162,** 1291–1308 (2005).

110. Helmstetter, A., Sornette, D. & Grasso, J.-R. Mainshocks are aftershocks of conditional foreshocks: How do foreshock statistical properties emerge from aftershock laws. *Journal of Geophysical Research: Solid Earth* **108.** doi:10.1029/2002jb001991. https://doi.org/10.1029/2002jb001991 (2003).

111. Bohnenstiehl, D., Sprinkle, D., Baillard, C, Moyer, P. & Boettcher, M. *Spatial, Temporal and Size-Frequency Characteristics of Microearthquake Sequences Leading up to the 2015 Eruption of Axial Seamount* in *AGU Fall Meeting Abstracts* (2018).

112. Roy, M. & Marone, C. Earthquake nucleation on model faults with rate- and state-dependent friction: Effects of inertia. *Journal of Geophysical Research: Solid Earth* **101,** 13919–13932 (1996).

113. Hardebeck, J. L., Nazareth, J. J. & Hauksson, E. The static stress change triggering model: Constraints from two southern California aftershock sequences. *Journal of Geophysical Research: Solid Earth* **103,** 24427–24437 (1998).

114. Ide, S., Yabe, S. & Tanaka, Y. Earthquake potential revealed by tidal influence on earthquake size–frequency statistics. *Nature Geoscience* **9,** 834–837 (2016).

115. Clague, D. A. *et al.* Chemical Variations in the 1998, 2011, and 2015 Lava Flows From Axial Seamount, Juan de Fuca Ridge: Cooling During Ascent, Lateral Transport, and Flow. *Geochemistry, Geophysics, Geosystems* **19,** 2915–2933 (2018).

116. Shapiro, N. M. & Campillo, M. Emergence of broadband Rayleigh waves from correlations of the ambient seismic noise. *Geophysical Research Letters* **31** (2004).

117. Brenguier, F. *et al.* Towards forecasting volcanic eruptions using seismic noise. *Nature Geoscience* **1,** 126 (2008).

118. Brenguier, F. *et al.* Mapping pressurized volcanic fluids from induced crustal seismic velocity drops. *Science* **345,** 80–82 (2014).

119. Lecocq, T., Caudron, C. & Brenguier, F. MSNoise, a Python Package for Monitoring Seismic Velocity Changes Using Ambient Seismic Noise. *Seismological Research Letters* **85,** 715–726 (2014).

120. Ratdomopurbo, A. & Poupinet, G. Monitoring a temporal change of seismic velocity in a volcano: Application to the 1992 eruption of Mt. Merapi (Indonesia). *Geophysical Research Letters* **22,** 775–778 (1995).

121. Clarke, D., Zaccarelli, L., Shapiro, N. M. & Brenguier, F. Assessment of resolution and accuracy of the Moving Window Cross Spectral technique for monitoring crustal temporal variations using ambient seismic noise. *Geophysical Journal International* **186,** 867–882 (2011).

122. Wallace, L. M. *et al.* Slow slip near the trench at the Hikurangi subduction zone, New Zealand. *Science* **352,** 701–704 (2016).

123. Meier, U., Shapiro, N. M. & Brenguier, F. Detecting seasonal variations in seismic velocities within Los Angeles basin from correlations of ambient seismic noise. *Geophysical Journal International.* doi:10.1111/j.1365-246x.2010.04550.x. https://doi.org/10.1111/j.1365-246x.2010.04550.x (2010).

124. Hillers, G, Ben-Zion, Y, Campillo, M & Zigone, D. Seasonal variations of seismic velocities in the San Jacinto fault area observed with ambient seismic noise. *Geophysical Journal International* **202,** 920–932 (2015).

125. Zhan, Z., Tsai, V. C. & Clayton, R. W. Spurious velocity changes caused by temporal variations in ambient noise frequency content. *Geophysical Journal International* **194,** 1574–1581 (2013).

126. Donaldson, C., Caudron, C., Green, R. G., Thelen, W. A. & White, R. S. Relative seismic velocity variations correlate with deformation at Kīlauea volcano. *Science Advances* **3,** e1700219 (2017).

127. Einarsson, P. Umbrotin við Kröflu 1975–1989. *Náttúra Mỳvatns. Hið íslenska náttúrufræðifélag, Reykjavík* (1991).

128. Wright, T. J. *et al.* Magma-maintained rift segmentation at continental rupture in the 2005 Afar dyking episode. *Nature* **442,** 291–294 (2006).

129. Tolstoy, M., Wilcock, W., Tan, Y. J. & Waldhauser, F. A Tale of Two Eruptions: How Data from Axial Seamount Led to a Discovery on the East Pacific Rise. *Oceanography* **31,** 124–125 (2018).

130. Wilcock, W. S. D. *et al.* The role of magma injection in localizing black-smoker activity. *Nature Geoscience* **2,** 509–513 (2009).

131. Johnson, J. H., Poland, M. P., Anderson, K. R. & Biggs, J. A cautionary tale of topography and tilt from Kīlauea Caldera. *Geophysical Research Letters.* doi:10.1029/2018gl081757. https://doi.org/10.1029/2018gl081757 (2019).